Department Chemie und Pharmazie

FRIEDRICH-ALEXANDER UNIVERSITÄT ERLANGEN-NÜRNBERG
NATURWISSENSCHAFTLICHE FAKULTÄT

Surface Enrichment Effects, CO_2 Capture, and Acid-Base Reactions in Ionic Liquids Studied by Conventional and Dual Analyser X-ray Photoelectron Spectroscopy

Untersuchung von Oberflächenanreicherungseffekten, CO_2-Abscheidung und Säure-Base-Reaktionen in Ionischen Flüssigkeiten mit herkömmlicher und Dualanalysator-Röntgenphotoelektronenspektroskopie

Der Naturwissenschaftlichen Fakultät der
Friedrich-Alexander-Universität Erlangen-Nürnberg

zur Erlangung des Doktorgrades Dr. rer. nat.

vorgelegt von

Inga Niedermaier

aus Mannheim

Als Dissertation genehmigt
von der Naturwissenschaftlichen Fakultät
der Friedrich-Alexander-Universität Erlangen-Nürnberg

Tag der mündlichen Prüfung: 30.05.2016

Vorsitzender des Promotionsorgans: Prof. Dr. Jörn Wilms

Gutachter: Prof. Dr. Hans-Peter Steinrück
Prof. Dr. Jürgen Schatz

Contents

Contents of Appendix

Published papers:

[P1] N. Taccardi, I. Niedermaier (shared 1st authorship), F. Maier, H.-P. Steinrück, and P. Wasserscheid, *Cyclic Thiouronium Ionic Liquids: Physicochemical Properties and their Electronic Structure Probed by X-Ray Induced Photoelectron Spectroscopy*, Chem-Eur J, 18, 27, 8288-8291, **2012**.

The author's contribution to [P1] are the ARXPS investigations and the corresponding data evaluation.

[P2] I. Niedermaier, N. Taccardi, P. Wasserscheid, F. Maier, and H.-P. Steinrück, *Probing a Gas/Liquid Acid-Base Reaction by X-ray Photoelectron Spectroscopy*, Angew Chem Int Edit, 52, 34, 8904-8907, **2013**.

[P3] I. Niedermaier, M. Bahlmann, C. Papp, C. Kolbeck, W. Wei, S. Krick Calderón, M. Grabau, P. S. Schulz, P. Wasserscheid, H.-P. Steinrück, and F. Maier, *Carbon Dioxide Capture by an Amine Functionalized Ionic Liquid: Fundamental Differences of Surface and Bulk Behavior*, J Am Chem Soc, 136, 1, 436-441, **2014**.

[P4] C. Kolbeck, I. Niedermaier, A. Deyko, K. R. J. Lovelock, N. Taccardi, W. Wei, P. Wasserscheid, F. Maier, and H.-P. Steinrück, *Influence of Substituents and Functional Groups on the Surface Composition of Ionic Liquids*, Chem-Eur J, 20, 14, 3954-3965, **2014**.

The author's contribution to [P4] are the ARXPS investigations and the data evaluation of the ILs [(PhC$_3$)C$_1$Im][Tf$_2$N], [(ClC$_2$)C$_1$C$_1$Im][TfO], [(BrC$_2$)C$_1$Im][Tf$_2$N], [(IC$_2$)C$_1$Im][Tf$_2$N], [(MeSC$_2$)C$_1$Im][Tf$_2$N], [C$_2$C$_1$(MeS)Im][Tf$_2$N], [C$_8$C$_1$Im][ClC$_4$SO$_3$], [(Me$_2$NC$_3$)C$_1$Im][TfO], and [(HOC$_2$)$_2$Me$_2$N][H$_2$NC$_2$SO$_3$] (the latter three in collaboration with C. Kolbeck).

[P5] I. Niedermaier, C. Kolbeck, H.-P. Steinrück and F. Maier, *Dual Analyzer System for Surface Analysis dedicated to angle-resolved photoelectron spectroscopy at liquid surfaces and interfaces*, Rev Sci Inst, 87, 4, 45105, **2016**.

Appendix chapter:

List of Abbreviations

ACN	Acetonitrile
ARUPS	Angle-resolved Ultraviolet Photoelectron Spectroscopy
ARXPS	Angle-resolved X-ray Photoelectron Spectroscopy
ASF	Atomic Sensitivity Factor
BE	Binding Energy
CAE	Constant Analyser Energy
CCD	Charge-coupled Device
CCS	Carbon dioxide Capture and Storage
CHA	Concentric Hemispherical Analyser
cp	Cyclopentadiene
DASSA	Dual Analyser System for Surface Analysis
ESCA	Electron Spectroscopy for Chemical Analysis
Fc	Ferrocene
fwhm	Full Width at Half Maximum
GF	Geometry Factor
ID	Information Depth
IL	Ionic Liquid
iXPS	Imaging X-ray Photoelectron Spectroscopy
L	Linker
LEED	Low Energy Electron Diffraction
LEIS	Low Energy Ion Scattering
MCP	Multichannel Plate or Microchannel Plate
MEA	Monoethanolamine
NAP XPS	Near-ambient Pressure X-ray Photoelectron Spectroscopy
PE	Pass Energy
PSi	Polysiloxane
QMS	Quadrupole Mass Spectrometer
RT	Room Temperature
SI	Supporting Information
SILP	Supported Ionic Liquid Phase
UHV	Ultra-high Vacuum
UPS	Ultraviolet Photoelectron Spectroscopy
XPS	X-ray Photoelectron Spectroscopy

1. Introduction

X-ray photoelectron spectroscopy (XPS) is one of the most versatile methods in surface science. It enables extracting quantitative information about the chemical composition of a sample and about the chemical bonding of an element within the outermost few nanometres close to the sample surface. XPS has to be carried out in ultra-high vacuum (UHV). This requirement restricts XPS investigations to low vapour pressure materials such as solids or untypical liquids, e.g. liquid metals or salt melts at high temperatures. All other classical liquids such as water and organic solvents simply evaporate when introduced into the UHV chamber.

Nevertheless, already in the early years of XPS, Kai Siegbahn, who is generally credited with the invention of XPS, investigated liquids by different approaches such as a precooled liquid beam that darts through a differentially pumped chamber section or a liquid coated wire continuously moving in front of the entrance lens of the spectrometer.[1,2] Especially the liquid beam method was developed further and is nowadays a well-established technique that gave rise to several insights into the surfaces of liquids.[3] But only with the increasing scientific popularity of ionic liquids (ILs) in the 1990s low vapour pressure liquids became available that enabled the investigation of real room temperature liquids as static samples.[4,5]

ILs are a class of liquids that have been the aim of intensive research within the last few decades. Their physical properties such as surface tension or density are comparable to that of other typical room temperature liquids.[6] Surface investigations of ILs can thus shed light on surface properties of liquids in general. Apart from that, ILs are of special interest in many areas such as gas capture, catalysis or nanoparticle formation[7,8], where the IL/vacuum interface and an understanding of interfacial processes is of fundamental importance. Among some other researchers, the group of Florian Maier and Hans-Peter Steinrück at Universität Erlangen-Nürnberg, Germany, started XPS at room temperature IL samples.[4,5,9,10] These studies are only possible due to the extremely low vapour pressure of ILs that makes them stable even under UHV. Exactly ten years ago, first test experiments proved to be successful and in the following years, a huge amount of knowledge was achieved on IL surfaces. In our group, angle-resolved measurements were carried out that enabled the determination of ion orientations in pure ILs, and of the vertical distribution of species in mixtures, solutions or dispersions based on ILs. A large amount of investigations were carried out on non-functionalised ILs, starting with imidazolium ILs containing alkyl chains of varying length combined with anions such as $[Tf_2N]^-$ and halides.[11,12] Simple side chain functionalisation e.g. by halogens and ethers was also part of these early studies[13] and in 2010/11, first tests to follow a reaction within an IL mixture by XPS proved to be successful.[14,15]

In this work, the horizon of these first fundamental insights obtained by angle-resolved XPS (ARXPS) on ILs has been considerably widened and investigations have been taken a huge step forward. This cumulative thesis is based on five publications listed on page 6. In the first part of this thesis, the main achievements are summarised. The papers and the respective supplementary information (SI) are reproduced in the Appendix.

The possibility of functionalising ILs by organic chemistry synthesis methods is the basis of their huge potential.[7,16] Nearly unlimited IL structures can be synthesised by combining simple ionic headgroups with moieties of different complexity. For processes such as homogeneously catalysed reactions using an IL-stabilised catalyst in a SILP system (SILP = Supported Ionic Liquid Phase), interaction with the gas/liquid interface and diffusion within the IL is of decisive importance[17] for e.g. catalyst turn over frequency and selectivity, but also for understanding the reaction kinetics. Functionalisation influences surface composition of IL moieties and consequently also their performance in processes that rely on interaction with the surface of the IL. Studies on a few basic compounds containing simple functional groups have already been carried out in the early years of IL research with XPS.[13] In Chapter 4 of this thesis, this topic is extended to a huge database of differently functionalised IL structures that allow inferring a set of ubiquitously valid rules for ion orientation at IL surfaces (see [P4]). Also, unpublished data on ferrocenyl-functionalised ILs are shown.

Functionalisation introduces reactivity into ILs and hence the possibility to carry out reactions under XPS monitoring. First trials were carried out *in situ* in 2011 on a reaction between two functionalised ILs. It was proven that XPS is not only suitable to track the reaction progress, but also to display concurrent changes in surface composition.[14,15] This topic is pursued in Chapter 5 including the results of [P2] and [P3]. After showing unpublished data that highlights the challenge of XPS reaction monitoring, two gas-liquid reactions taking place at the gas-IL interface are detailed there. CO_2 absorption of an amine-functionalised IL was investigated *in situ* by near ambient pressure XPS in [P3], enabling fundamental conceptual findings on the underlying reaction mechanism as well as important conclusions for CO_2 removal in general. [P2] investigates the reaction of an IL with a gaseous acid, which sheds light on reaction rate and product diffusion.

Chapter 6 and [P5] deal with one remaining challenge of ARXPS on ILs: angle-resolved measurements typically involve rotating the sample along its polar axis. However, this is impossible for low-viscous macroscopic liquid samples that trickle down from the tilted sample holder. Therefore, a new chamber concept was planned and realised within our group that will be the source of a wealth of future knowledge in IL surface science: the DASSA (Dual Analyser System for Surface Analysis) contains two electron analysers fixedly mounted at 0° and 80° emission angles towards a horizontal sample and thus allows simultaneous angle-resolved

measurements without the need of sample rotation. DASSA further extends the surface sensitive investigation possibilities from ARXPS to angle-resolved UPS (ARUPS), low energy ion scattering (LEIS) and Imaging XPS (iXPS) as it contains multiple excitation and detection options. Also, being equipped with a monochromatic X-ray source the resolution is much improved compared to our earlier results. DASSA is unique worldwide and has the potential to revolutionise surface sensitive investigations of liquids in the same way as the first idea of placing an IL into an XPS chamber did ten years earlier.

Chapter 7 expands on the topic of XPS chemical shifts that allow for differentiation of the constituent atoms of an IL by their chemical environment. The influence of binding position on electron density for ILs functionalised with a thioether group is discussed in [P1], and unpublished DASSA results with improved resolution deal with more subtle electronic differences, e.g. in different cationic nitrogen species.

2. Fundamentals and Techniques

2.1. X-ray photoelectron spectroscopy

X-ray photoelectron spectroscopy (XPS) is an extensively used technique that is based on the photoelectric effect first observed by Heinrich Hertz and Wilhelm Hallwachs roughly 130 years ago.[18,19] The 1960s are commonly denoted the birth decade of XPS because vacuum equipment was sufficiently developed to create ultra-high vacuum (UHV) conditions. UHV is required due to the highly restricted inelastic mean free path of electrons in gaseous media, the requirement of an atomically clean surface with a slow rate of re-coverage by species from the remaining gas and for technical reasons. Also, the commencing availability of computers for analyser control and detector readout and further technical improvements played a role. Kai Siegbahn pioneered modern XPS by developing the technique hugely forward close to its nowadays potential.[20]

In photoelectron spectroscopy, irradiation of a sample with photons (X-rays in the case of XPS) of a fixed energy results in photoelectron emission from the sample, with the kinetic energy of the electron $E_{\mathrm{kin,s}}$ relative to the vacuum level of the sample given by

$$E_{kin,s} = h\nu - BE - \phi_s \tag{1}$$

where $h\nu$ is the photon energy, BE is the electron binding energy relative to the Fermi energy and ϕ_s is the work function of the sample (see Figure 1). In XPS experiments of solids and liquids, the sample has to be in electrical contact with the electron analyser so that the Fermi levels of sample and analyser equalise. The detected kinetic energy $E_{\mathrm{kin,a}}$ relative to the analyser then becomes:

$$E_{kin,a} = h\nu - BE - \phi_a \tag{2}$$

with ϕ_a the work function of the analyser. ϕ_a is a constant value that is commonly determined by calibrating the instrument with a reference peak of well known BE.

Discrete loss processes take place within the sample as a result of photoemission. These final state effects are observable as characteristic features in the photoelectron spectrum. Most importantly, these are Auger lines and shake-up satellites. Furthermore, initial state effects such as spin-orbit splitting determine the fine structure of the spectra. For a detailed description of these features, References 21-23 are recommended. Most electrons leaving the sample have undergone quasi-continuous loss processes on their way to the sample surface and thus, these electrons only contribute to the broad spectral background. This small mean free path

of the excited photoelectrons in the nanometre or even sub-nanometre regime (depending on their kinetic energy and on the density of the material) makes XPS one of the most powerful tools in Surface Science (see also next section).

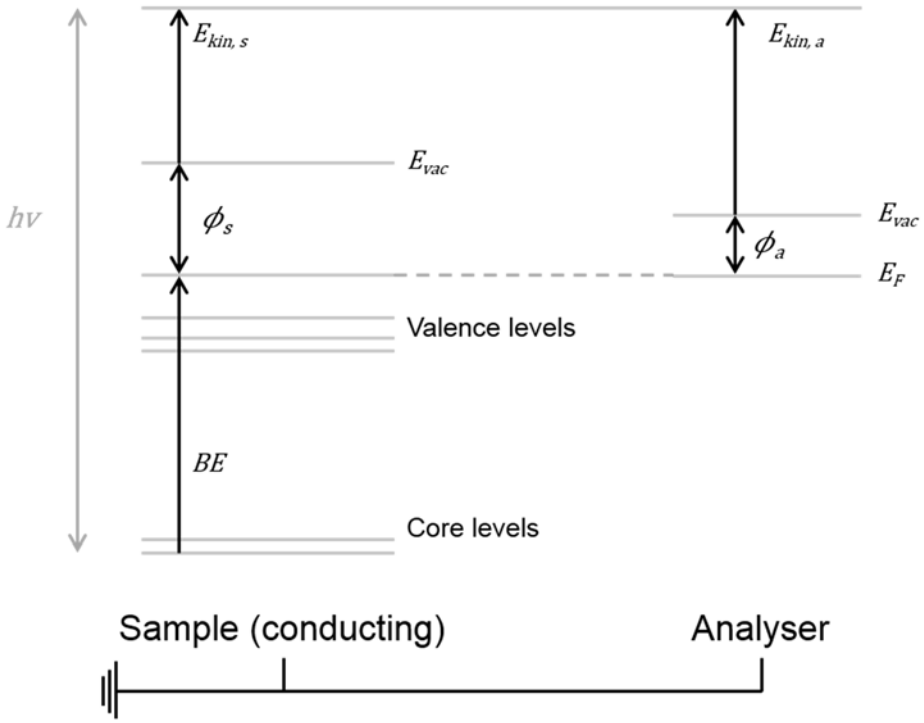

Figure 1: Energy levels involved in the photoelectron emission process in XPS (hv = photon energy, BE = photoelectron binding energy relative to the Fermi level E_F, E_{vac} = vacuum level, $E_{kin,s}$ = kinetic energy relative to the sample, $E_{kin,a}$ = detected kinetic energy relative to the analyser, ϕ_s = work function sample, ϕ_a work function analyser).

The huge popularity of the method XPS is due to the fact that both chemical and quantitative information can be obtained from the spectra. The exact photoelectron BE depends on the chemical environment of the emitting atom (element) and can vary up to several eV in different binding situations. Furthermore, quantification of the elements present within one sample is possible after correcting the measured peaks by atomic sensitivity factors (ASFs). They mainly account for the fact that electrons of different core levels have different cross sections, i.e. different probabilities to be excited to above the vacuum level upon photoexcitation.

The basic components needed to carry out XPS are a UHV chamber, an X-ray source and an electron analyser. But commonly, XPS chambers contain further equipment enabling multiple options for sample treatment and analysis. The three XPS setups used for the work in this thesis are described in detail in Chapter 3.

2.2. Angle-resolved XPS

XPS is inherently a surface sensitive technique due to the low inelastic mean free path (λ) of electrons in matter. λ is defined as the length over which the photoelectron signal decreases from I_0 to (I_0 / e). λ depends on E_{kin} of the electron, a relationship which roughly follows the well known 'universal curve'.[24] Using the NIST Electron Inelastic-Mean-Free-Path Database[25], for photoelectrons with E_{kin} in the range of interest for Al Kα excitation ($h\nu$ = 1486.6 eV, E_{kin} = 800-1300 eV), λ is determined to be 2.3-3.0 nm in organic matter. Signal attenuation increases with increasing escape depth of the photoelectrons, and the XPS information depth (ID) is defined as the depth from which ~95 % of the recorded signal originates. The value of 95 % is derived by a signal attenuation to (I_0 / e^3), so that ID is given by $3 * \lambda$. For ILs, ID is thus 7-9 nm.

As ID is quoted as a depth perpendicular to the surface, this value only holds true for photoelectrons collected at normal emission (ϑ = 0°, with ϑ the emission angle relative to the surface normal). The geometrical relationship for emission under angles ϑ ≠ 0° is given by

$$ID = 3 * \lambda * cos\vartheta \qquad (3)^{26}$$

so that ID decreases with increasing emission angle.

This dependence is employed for angle-resolved XPS (ARXPS), where spectra recorded under normal emission are compared to spectra taken at high emission angles (ϑ = 80° for the spectra shown in this thesis). The ID thus decreases to 1.0-1.5 nm, enabling effects of surface enrichment or depletion of species to be determined from changes in signal intensity when comparing 0° to 80° data. One should note at this point that at large emission angles, elastic scattering effects might play a role[26], but they are not considered in this thesis.

2.3. ARXPS on ILs

As noted above, XPS has to be carried out under UHV, which automatically restricts its use to solids, unusual liquids such as salt melts at very high temperatures and gases at extremely low partial pressures. Common liquids are excluded due to their high vapour pressure, resulting in direct evaporation, the moment a liquid sample is pumped down for introduction into the UHV chamber. Although Kai Siegbahn already in the early days of XPS sought ways to extend XPS also to liquid samples and came up with ingenious ideas such as the liquid microjet technique[1,3], XPS investigations on static liquid samples of bulk amounts were not possible until in the 1990s, Ionic Liquids (ILs) came into scientific focus. In the following years,

ILs became a class of extensively studied materials due to their special properties such as electrical conductivity or high thermal stability. Apart from that, they feature a very low vapour pressure (10^{-9} mbar at room temperature[27]), making them stable under UHV and thus investigable by XPS. Ten years ago, several investigators carried out first successful trials of IL studies with XPS[5,9,10,28], among them also our group led by H.-P. Steinrück at the Universität Erlangen-Nürnberg, Germany.[4,29]

Table 1: Top: general IL structure, comprising a cation with a cationic headgroup (light grey, C^+) and an anion with the anionic headgroup (dark grey, A^-). Either or both ions can contain one or several side chains (R). The left and middle column show typical cationic and anionic headgroups, the right column shows a few possible side chains.

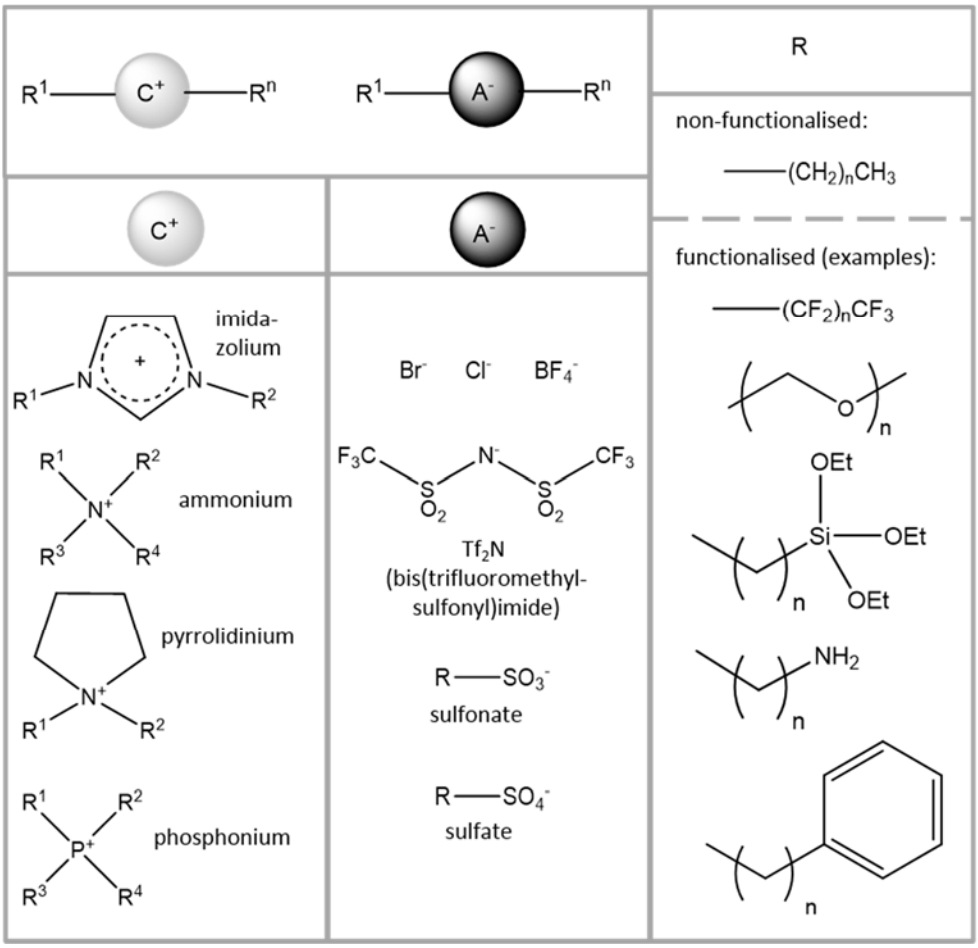

ILs basically are salt melts, i.e. are composed of anions and cations only. They are liquid below 100 °C and in many cases even at and below room temperature (RT), due to their spatially extended and often unsymmetrical ion structure. They are sufficiently similar to standard liquids to make XPS results on IL surface structures universally important. Apart from that, IL surface studies are especially important due to the applicability of ILs in areas such as catalysis, electrochemistry or phase extraction[16], where the interactions with surrounding media play a fundamental role in the underlying processes.

The general IL structure is given at the top of Table 1. As noted, ILs consist of cations and anions only and each of these structures can be subdivided into a charge carrying headgroup and one or several side chains. Monoatomic ions without side chains also exist. Typical cationic headgroups comprise (left column) imidazolium, ammonium, pyrrolidinium and phosphonium. Anions can be (middle) halogenides such as bromide or chloride, or extended structures such as the $[BF_4]^-$ complex or the very common $[Tf_2N]^-$ anion. Anions with different side chains also exist, such as sulfonates and sulphates shown at the bottom. Side chains on both anions and cations (R, right column) can be simple alkyl chains of different lengths (top). Apart from that, functionalised side chains can contain different organic moieties such as halogenated, branched or unsaturated alkyls or many other functional groups such as ethers, ethoxysilanes, amines or phenyl, to just name a few. XPS investigations on such functionalised ILs in general and in reaction applications is the main subject of this thesis. Before embarking on these results, a brief review of results obtained on the IL/vacuum interface of basic, non-functionalised ILs by ARXPS is given.

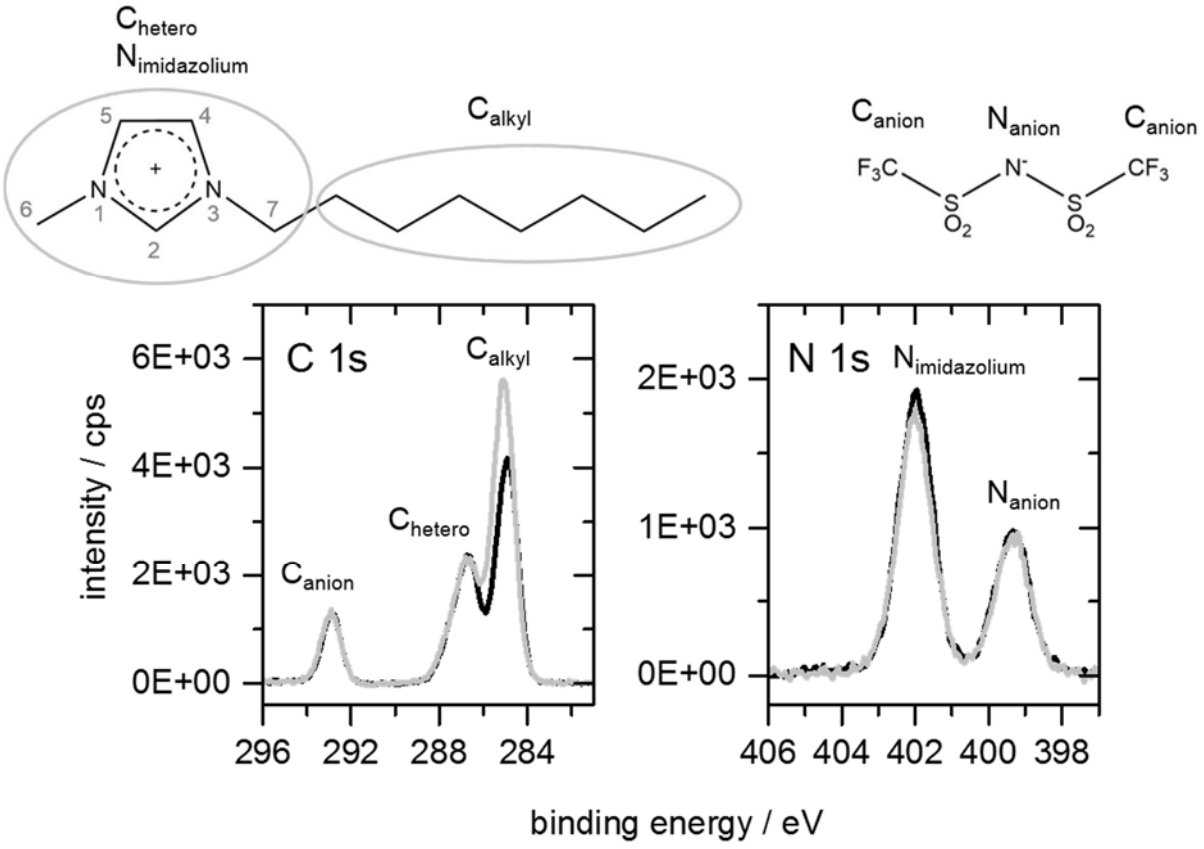

Figure 2: C 1s and N 1s spectra of $[C_8C_1Im][Tf_2N]$ at 0° (black) and 80° (grey) emission, indicating strong surface enrichment of the alkyl group of the cation. The spectra were recorded with the DASSA setup (see Chapter 3).

In Figure 2, the C 1s and N 1s spectra of 3-octly-1-methyl imidazolium ($[C_8C_1Im][Tf_2N]$), a primary IL commonly used as a reference substance by our group, are depicted. Its structure is given at the top together with numeration of the atoms of imidazolium for later reference.

The black spectra were recorded at 0° emission, and the grey spectra at 80° emission. The latter are scaled by a geometry factor (GF) of 1.9 to account for overall intensity loss at grazing emission conditions (details on GF can be found in [P5]). The three peaks visible in the C 1s region are attributed to both anionic C atoms, the five C atoms bound to N in the imidazolium moiety of the cation (C_{hetero}) and the seven C atoms bound to C and H only in the alkyl moiety of the cation, in order of decreasing BE. The N 1s region shows two signals in a 2 : 1 ratio, with the more intense one attributable to both imidazolium N atoms, and the less intense one to the single anionic N atom. In the 80° spectra, C_{alkyl} clearly increases in intensity, while C_{anion} and N_{anion} remain virtually constant and C_{hetero} and $N_{imidazolium}$ decrease slightly. For C_{hetero}, this decrease is not very pronounced as it is compensated by the increase of the overlapping C_{alkyl} signal. For the IL/vacuum interface, one can thus conclude that the cation is orientated such that the nonpolar alkyl chain is strongly enriched in the topmost layers, whereas the imidazolium rings lie beneath this alkyl layer.[12]

This predominant orientation of nonpolar side chains is a general finding for ILs, as long as the chain is of sufficient length ($n \geq 4$), irrespective whether it is part of the cation or anion.[11] For a series of $[C_8C_1Im]^+$ ILs with different anions, it was also found that cation alkyl enrichment is strongest for ILs with small, well coordinating anions, and decreases with increasing anion volume.[12] These effects likely result from the interplay of several factors. Attractive electrostatic interactions between the charge carrying moieties facilitate arrangement into polar and non-polar domains. Orientation of the non-polar domain towards the gas phase is thereby favourable as it lowers the surface free energy of the system. For alkyl chains of identical length, the degree of surface orientation is determined by the distance between cation headgroup and anion: orientation is enhanced due to space restrictions when headgroups are in close proximity for ILs with small, well coordinating anions, and is less pronounced when the anion is larger with lower coordination behaviour. In addition, dispersive interactions between alkyl chains that depend on chain length and intermolecular distances influence the degree of orientation.

3. Experimental Details

For the investigations summarised in this work, three different XPS setups were used. The XPS chambers are termed "ESCA", "GAP" and "DASSA" according to terminology used in our workgroup. Each chamber is described below in detail and after that, particulars on data treatment and sample preparation is given. Some of the chambers contain components that were not used for any of the summarised results, e.g. an organic evaporator to prepare IL monolayers. Such components are not included in the below descriptions.

3.1. ESCA

The ESCA (Electron Spectroscopy for Chemical Analysis, a synonym to XPS) chamber is the most simple of all three setups and is based on an ESCALAB 200 spectrometer by VG (Vacuum Generators Ltd.) present within our group for more than twenty years. It was continuously adapted and extended, and during the here described research it had the overall layout shown in Figure 3, comprising a load lock chamber for sample introduction into UHV, a preparation chamber and an analysis chamber. The preparation chamber contains a LEED unit (Low Energy Electron Diffraction), a sputter gun for surface cleaning and a leak valve for gas dosage. Samples are moved on a long range XYZϑ manipulator from preparation to analysis chamber, where XP spectrum acquisition takes place. The excitation source is an X-ray gun (Specs XR50) with a double cooling circuit that considerably minimises sample heat up by infrared radiation from the source head. This non monochromatic source contains a dual anode capable of emitting either Al Kα radiation (1486.6 eV) at a maximum power of 400 W or Mg Kα radiation (1253.6 eV) at up to 300 W. The analyser used is a "Scienta R3000" concentric hemispherical analyser with 135 mm mean radius. It is a 2D analyser with a detection unit consisting of a multichannel plate (MCP), a phosphorous screen and a CCD camera that records the light flashes on the screen produced by electrons with 600 energy channels. The X-ray source replaced the original source of the ESCALAB 200 in 2011 and the analyser was mounted as a replacement of the original one in 2009. The analysis chamber further contains a flood gun for charge neutralisation and a quadrupole mass spectrometer (QMS) of type BALZERS QMA 120 with a mass range of 1-200 amu operated since the 1990s. The chamber base pressure is in the 10^{-10} mbar range which increases into the 10^{-9} mbar region during operation.

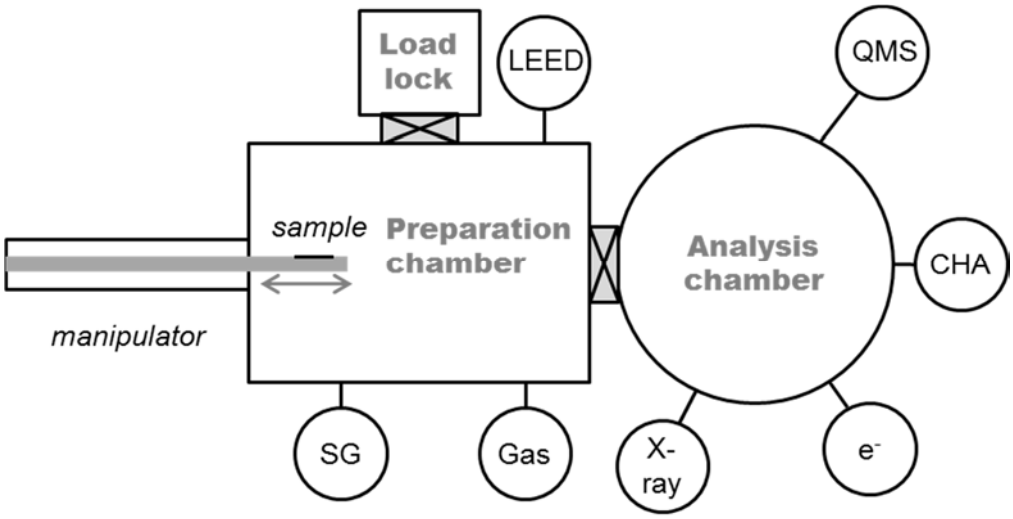

Figure 3: Scheme of the ESCA chamber used. SG = sputter gun, Gas = leak valve for gas dosage, X-ray = dual X-ray source (Al Kα, Mg Kα), e^- = electron gun, CHA = concentric hemispherical analyser, QMS = quadrupole mass spectrometer, LEED = low energy electron diffraction unit.

The original sample holder layout was changed in 2011 to a homemade system that unites the advantages of larger size with a concept of four transferrable electrodes that enable temperature measurements directly at the sample and have thus considerably increased reliability of temperature dependent investigations. This four electrode concept further opens up the possibility of electrochemical sample manipulation during XPS investigations. The ESCA sample holder is described in Reference 30 and its design with both named advantages was transferred to the chamber DASSA obtained in 2014 that is described in great detail in [P5].

The measurement software used is SES version 1.2.5 by VG Scienta that enables recording spectra in swept or snapshot mode. Sweeps are summed up for the final record file. In the snapshot mode, the window covers 12 % of the PE. The obtained spectra are saved in .pxt files that can be imported into CasaXPS (see below) with transfer of most metadata.

The ESCA chamber was used for the spectra shown in [P1], [P2] and [P4]. Basic analyser settings for the ESCA system were a curved slit aperture (0.8 mm x 20 mm) and transmission lens mode in sweep mode. For wide scans, settings were: 200 eV pass energy (PE), step size 1 eV, 3 "frames" (images) at a speed of 70 images/s, resulting in a dwell time of 0.043 s, 1 sweep. Settings for region scans were: 100 eV PE, step size 0.05 eV, 10 "frames" (images) at a speed of 70 images/s, resulting in a dwell time of 0.143 s, 10 sweeps.

X-ray gun settings used were: Al Kα radiation at 250 W power (U_{anode} = 12.5 kV, I_{emiss} = 20 mA) for spectra in [P1] and [P4], Mg Kα radiation at 250 W power (U_{anode} = 12.5 kV, I_{emiss} = 20 mA) for the data in [P2].

3.2. GAP

This chamber is a near ambient pressure (NAP) XPS setup built in 2004 that is capable of recording XP spectra at an analysis chamber pressure of up to 1 mbar. The name GAP indicates that it bridges the "pressure gap", the prevailing difference between surface studies of model compounds at non-realistic pressure ranges and real life application under ambient conditions. XP spectra can be recorded during *in situ* treatment of the sample with gases at much higher partial pressures than would be possible in standard UHV spectrometers. This is realised by a gas tight Al window between chamber and X-ray gun and by four differently pumped stages along the electron path from sample to detector comprising two sections in front of the lens system of the analyser with only minute orifices along the lens axis and two within the analyser. These features sufficiently seal the equipment that requires UHV (X-ray gun) or HV better than 10^{-6} mbar (analyser) from the high chamber pressure. The schematic chamber setup is shown in Figure 4.

The GAP chamber was used for the investigations of CO_2 absorption described in [P3]. It comprises an Omicron EA 125 U7 concentric hemispherical analyser of 125 mm mean radius with a 7 channel detector. It is modified with a tubule that enables differential pumping of the lens system and channeltrons with elongated connections to the counter unit that create space for attaching another turbomolecular pump close to the detector. Also, the lens voltages have been adjusted to increase the working distance to account for the space requirement of the differentially pumped stages in front of the lens system. The largest available entrance and exit apertures are used (entrance: rectangular 6 mm x 12 mm, exit rectangular 5 mm x 11 mm per channeltron) as it is actually the orifice of the differentially pumped sections that restricts the acceptance angle. The X-ray source is an XR 50 from Specs described for the ESCA chamber with a modified Al window that enables the above mentioned sealing. The base pressure is in the 10^{-9} mbar region. Two gas dosage inlets are available for either beam dosing or background dosing, of which only the latter was used for the presented data. The software that controls spectra recording is EIS 2.2.2 by Omicron. The resulting file is of .xps type, that was exported into the vamas format (.vms) used by Casa XPS (see below). The EIS export function transfers only the most vital metadata. A detailed description of the system can be found in Reference 31.

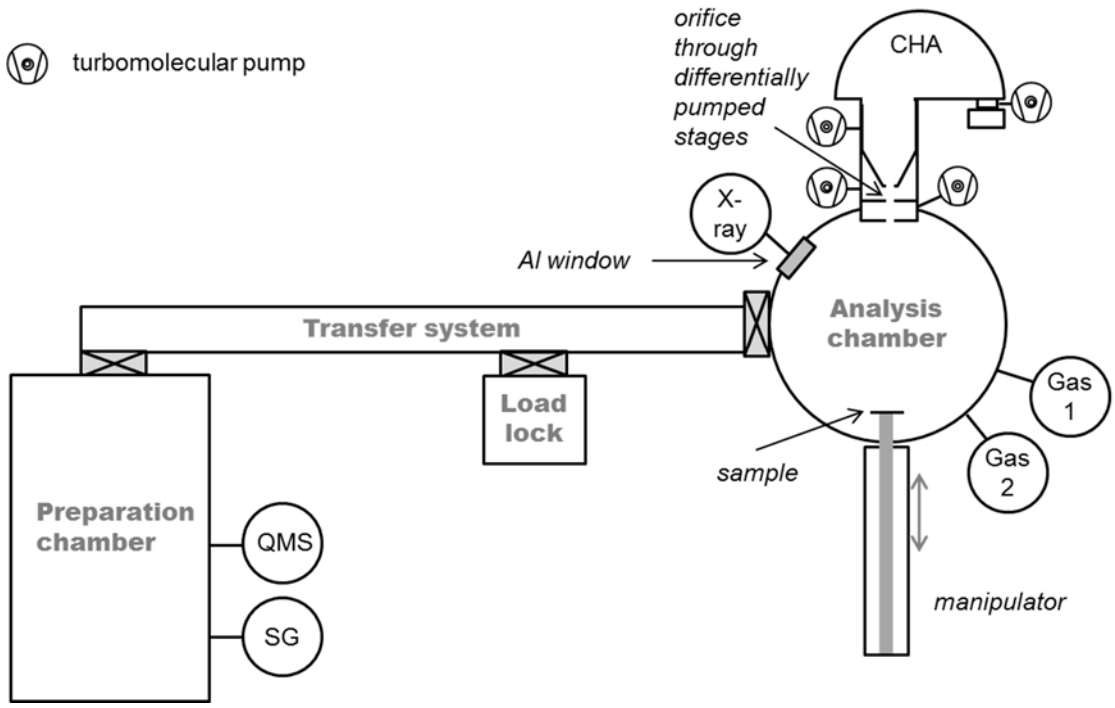

Figure 4: Schematic sketch of the GAP chamber setup that is capable of operating at near ambient pressure (NAP). SG = sputter gun, QMS = quadrupole mass spectrometer, X-ray = dual X-ray source (Al Kα, Mg Kα), Gas 1 = leak valve for beam dosing, Gas 2 = leak valve for background dosing, CHA = concentric hemispherical analyser. Turbomolecular pumps are only shown for the four differentially pumped analyser and chamber sections that enable operation at pressures of up to 1 mbar.

Spectra were recorded at 50 eV PE for region scans and at 200 eV PE for survey scans at high magnification in the constant analyser energy mode (CAE) with 0.2 s dwell time and 0.05 eV step size. Sweep mode is the only available option. For region scans of the N 1s region 20 sweeps were used, for all other region scans 10 sweeps were recorded. Survey spectra settings were 1.0 eV step size, 0.2 s dwell time and 1 sweep. Sweeps are averaged by the EIS software for the result file.

Al Kα radiation at 50 W power (U_{anode} = 13.0 kV) was used for excitation.

3.3. DASSA

An extensive description of the DASSA (Dual Analyser System for Surface Analysis) chamber is part of [P5], so only the most vital details are given here. This system was built in 2013 and is unique worldwide. DASSA is dedicated to ARXPS studies of liquids of low viscosity and/or high layer thickness that have to be kept horizontal, as they would drip down from the sample holder when rotated. Angle-resolved studies are enabled by two analysers mounted at normal and grazing emission angle relative to a horizontal sample that record spectra simultaneously.

It further enables the application of other surface science methods, namely ultraviolet photoelectron spectroscopy (UPS), low energy ion scattering (LEIS) and Imaging XPS (iXPS). Its overall design is given in Figure 5. It comprises a load lock, a preparation chamber and an analysis chamber with overall three gas dosing valves for reaction studies. A sample holder concept with four transferrable contacts similar to the one described for the ESCA was also implemented here.

As the chamber was only recently built by the company Omicron Nanotechnology (then part of Oxford Instruments plc., now part of Scienta Omicron), it is still mostly in its original layout, although some important additions have been done by now. To name just the core components, there are two identical Omicron Argus concentric hemispherical 1D analysers with a 124 mm mean radius and x/y deflectors that enable iXPS in addition to standard XPS. The detector is a coupled microchannel plate (MCP)/stripe anode device with 128 energy channels. The monochromatic X-ray source is Omicron XM 1000 capable of spot or line irradiation with one crystal of 100 mm size (dispersive direction) on a 500 mm Rowland circle diameter. The optimum spot diameter is 0.75 mm for horizontal incidence on a well-focussed sample and is estimated to be 1-1.5 mm for the given chamber setup with the X-ray source at grazing incidence on the horizontal sample.

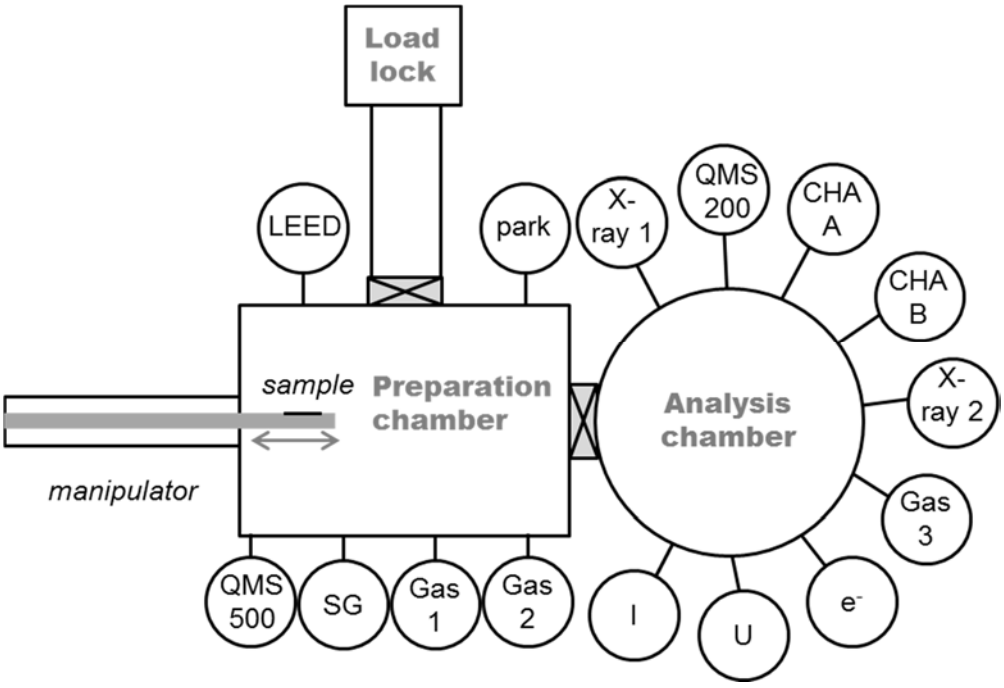

Figure 5: Schematic sketch of the DASSA chamber layout with two concentric hemispherical analysers (CHA A at 0° emission and CHA B at 80° emission) that enable simultaneous angle-resolved measurements on horizontal liquid samples. I = ion source, U = UV source, X-ray 1 = monochromatic Al Kα source, X-ray 2 = dual Al Kα/Mg Kα source, QMS = quadrupole mass spectrometer with mass range 1-200 amu (analysis chamber) or 1-500 amu (preparation chamber), e^- = flood gun, Gas 1-3 = leak valves for gas dosage, SG = sputter gun, LEED = low energy electron diffraction unit, park = multiple sample parking positions.

Both analysers are controlled simultaneously by one user interface, a specifically configured dual version of the measurement software Matrix T 3.2. Standardly, the constant analyser energy mode (CAE) was used with a curved slit aperture (1 mm x 10 mm) and high magnification in sweep mode. Survey spectra were recorded with 200 eV PE, a step size of 1 eV and a dwell time of 0.5 s. Region scans were recorded at 35 eV PE, a step size of 0.05 eV and a dwell time of 1.5 s. The high dwell times were used as the option of several sweeps per spectrum was not available in the specifically configured dual software version. The resulting file format is .mtrx that can only be displayed with the Omicron software Vernissage that is also available in a specifically configured dual version. Export is done from Vernissage to the Casa XPS file type .vms.

The base pressure of the chamber is in the 10^{-11} mbar region and during measurements, the pressure increased into the 10^{-10} mbar region. A quadrupole mass spectrometer (Hiden HAL 3F 511) connected to the preparation chamber allows for residual gas analysis even of high mass compounds (max. 510 amu).

3.4. Data analysis and display

All data was analysed with the software Casa XPS. Version 2.3.16Dev6 was used for all spectra recorded with ESCA and GAP and version 2.3.16 PR 1.5 was used for all DASSA spectra. Both versions are identical in evaluating XPS data. The PR 1.5 version contains an additional functionality needed for iXPS data handling at DASSA. Data fitting in Casa for ESCA data was carried out using the fitting models described in Reference 11. For GAP data, no fitting models were available and the ESCA models were used due to the reasonable assumption that both systems should result in similar spectra.

The fit model had to be modified in the C 1s region for DASSA due to the improved resolution when using monochromatic X-rays. Both fit models are compared in Figure 6 for the standard imidazolium IL $[C_8C_1Im][Tf_2N]$. The fitted C 1s region of $[C_8C_1Im]Cl$ is also shown. For both models, a two point linear background is subtracted for all regions except C 1s of $[C_8C_1Im][Tf_2N]$ where a three point linear background is used to account for the higher slope underneath the C_{anion} component at highest BE. For the peaks, Pseudo Voigt functions are used with 70 % Gaussian and 30 % Lorentzian contribution.

The ions contain only equivalent fluorine (F), oxygen (O) and sulphur (S) atoms so that only one peak is observed in the F 1s, O 1s and S 2p region. F 1s and O 1s are thus fitted with a single peak without constraints. For S 2p, the peak is split into a doublet due to spin-orbit

splitting and fitting constraints are used as resulting from the nominal peak value ratios: an identical full width at half maximum (fwhm) for both components and a 1 : 2 area ratio ($S\ 2p_{1/2}$: $S\ 2p_{3/2}$). The average peak distance was determined from a range of different measurements of the S 2p region and used as a constraint: for ESCA, the value is 1.18 eV and for DASSA, it was found to be 1.21 eV which is attributed to the better resolution. For other doublets, the procedure is identical in that the nominal peak area ratios and identical fwhm values are used as fitting constraints. For clearly separated doublet components, no peak distance constraint was used. For overlapping doublet peaks of elements that are present in other XPS suitable compounds, different reference measurements were carried out to obtain a valid peak splitting value. In all other cases the doublet separation reported in the NIST database[32] was used.

Looking at regions containing more than one component, the N 1s region is fitted with two separate peaks without constraints as they are clearly separated. For the C 1s region, the C_{anion} peak at highest BE that is well separated from the main signal is also fitted without constraints. The main peak contains several contributions that can be distinguished differently depending on energy resolution. For ESCA/GAP spectra obtained with non-monochromated X-ray sources, there is one C_{hetero} component at higher BE and a C_{alkyl} component at lower BE. Fitting constraints are only made for the fwhm ratio that is set to 1.1 : 1.0 (C_{hetero} : C_{alkyl}). For DASSA, spectra recorded with a monochromated Al Kα source, the C_2 component that has the highest shift due to two neighbouring N atoms can be distinguished as a high BE shoulder in the raw data and is fitted as a separate component. The residual four C atoms attached to one N each are then termed $C_{hetero'}$ (note the prime symbol at the end of the subscript). Consequently $C_{hetero'}$ + C_2 of the DASSA model equal C_{hetero} of the ESCA/GAP model. Constraints made are: fwhm ratio 1.0 : 1.1 : 1.0 (C_2 : $C_{hetero'}$: C_{alkyl}) and distance between C_2 and C_{hetero} = 0.9 eV. For both cases, these constraints have been obtained by first fitting a large number of imidazolium based IL spectra with the nominal area constraint only, i.e. C_{hetero} : C_{alkyl} area ratio was set to 5 : (n-1) for ESCA spectra of $[C_nC_1Im]^+$ ILs and to C_2 : $C_{hetero'}$: C_{alkyl} = 1 : 4 : (n-1) for DASSA spectra. Resulting average fwhm ratios and peak distances that were found to be very similar for all these pre-fits were then used for the final fit models with the constraints given above.

The alkyl-hetero distance cannot be constrained as is clear when comparing the C 1s regions of $[C_8C_1Im][Tf_2N]$ and $[C_8C_1Im][Cl]$ in Figure 6. This distance varies considerably for the same cation combined with different anions due to interionic effects.[12] For non-imidazolium based ILs and also for imidazolium ILs with very long alkyl chains (e.g. $[C_{18}C_1Im]^+$ based ILs), these fit models have to be adapted using assumptions such as the presence of C_{hetero} and C_{alkyl}

components and sometimes pre-fits fixing the area ratio to the nominal values to obtain reasonable fitting parameters.

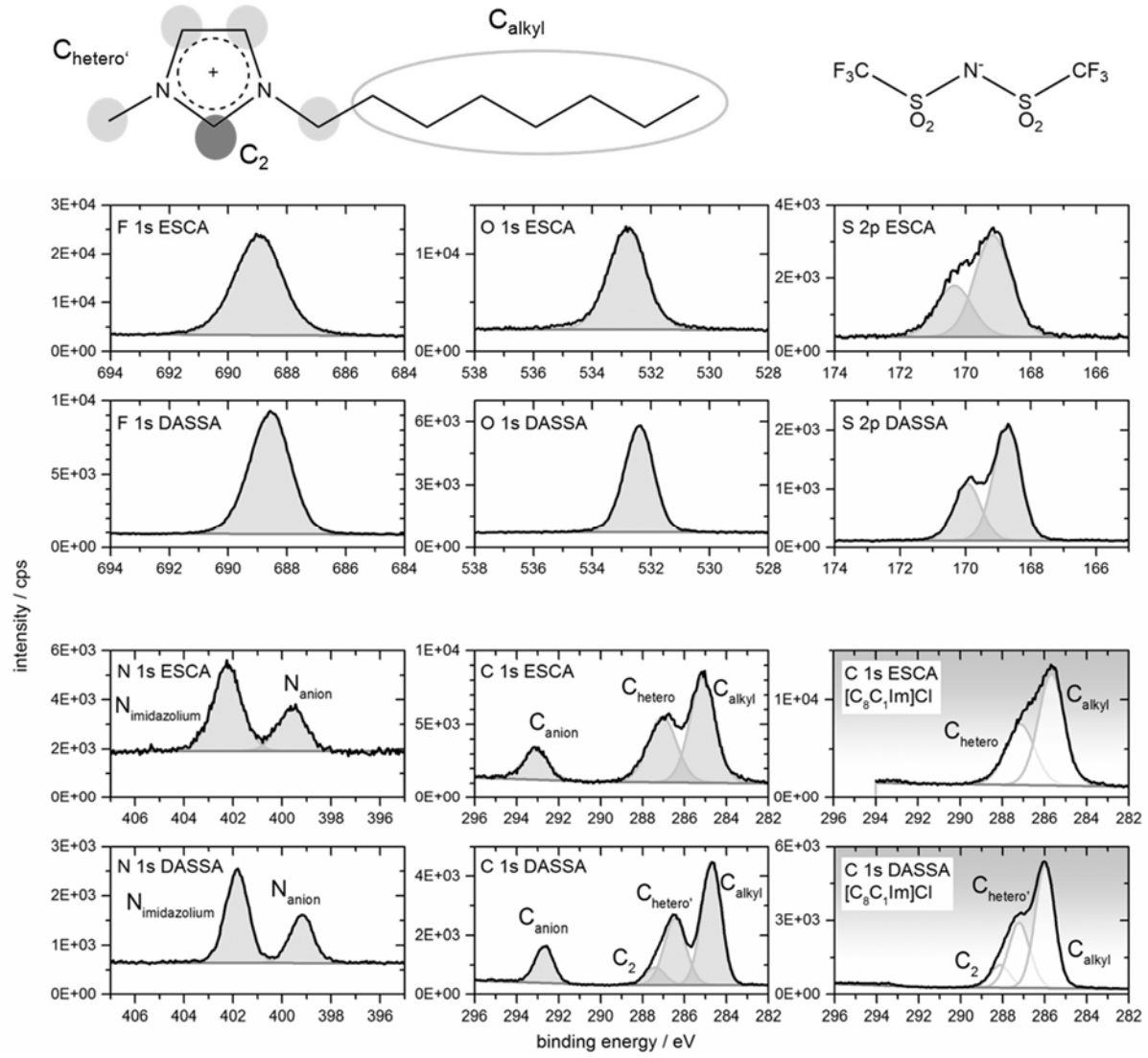

Figure 6: Fitting model for the exemplary IL $[C_8C_1Im][Tf_2N]$. Models are identical for ESCA and DASSA spectra for all regions except C 1s, where an additional peak (C_2) can be resolved for DASSA. The grey background C 1s spectra show the region for a different IL ($[C_8C_1Im]Cl$) that contains no C_{anion} peak and exhibits a C_{hetero} ($C_{hetero'}$ for DASSA) to C_{alkyl} peak distance clearly different from the $[C_8C_1Im][Tf_2N]$ C 1s spectrum.

Usually, 80° spectra are fitted using the same constraints than for 0° spectra. However, in the case of 80° spectra where components are either not well visible or not well separated, additional constraints are used to link the 80° fits to those of the respective 0° measurements. For example, it is sometimes not sufficient to simply fix an fwhm ratio as the resulting fit exhibits extremely broad peaks with fwhms = 3-9 eV. In such cases the maximum fwhms are constrained to the fwhms of the respective components in the 0° spectrum. Also, to prevent fits with peak positions shifted beyond reasonable limits, a peak distance or even a fixed peak position constraint may be necessary. Peak distances are usually found to be identical in

0° and 80° apart from the C_{hetero} and C_{alkyl} distance that varies with emission angle for ILs with long alkyl chains. This effect is likely a result of a changing charge environment at the outermost surface dominated by nonpolar alkyl chains.

If fit parameters diverge from those detailed above or signal intensities are not deduced by fit, but by numerical integration, this is commented on in the corresponding data in this thesis.

All spectra used in the figures of this thesis were produced with Origin versions 8.0, 9.0 and Home Use 2015, depending on the time of spectra production. Spectra were imported into Origin as .txt files produced by Casa XPS that contained the recorded data points as well as the background and fit curves. Where background subtracted spectra are shown, the imported Casa XPS background was subtracted from the measured spectra in Origin. No other data manipulation was carried out in Origin.

3.5. Spectra quantification

To extract quantitative information from fitted or integrated curve areas, the values have to be corrected with atomic sensitivity factors (ASFs). They mainly account for differrent cross sections of photoelectrons originating from different core levels, but are also dependent on factors such as the angle of X-ray incidence or the transmission function of the analyser. The concept of ASFs and also a large ASF value database is presented by Wagner et al. in Reference 33. This database is used as it is by many researchers, but realising that ASF values can differ considerably between different experimental setups[34], for the ESCA and DASSA chambers a calibration has been carried out that includes determination of a limited number of ASFs by reference measurements, and relating these to the Wagner values to obtain a function that enables correction of all other values given in the Wagner database.

The procedure for ESCA is described in Reference 35, and the (identical) procedure for DASSA is given in detail in [P5]. High quality ILs without contaminations are ideally suited for these ASF reference measurements as they possess a well-defined stoichiometry of a range of elements whose signals cover a wide range of kinetic energies. The experimental atom ratio of a sample is obtained by relating the sum of all ASF corrected peak areas to the sum of all atoms present in the IL in nominal stoichiometry.

3.6. Sample preparation

A few (2-4) pipette drops of all investigated liquids were spread with a pipette tip onto a solid support attached to the actual sample holder. The sample holder was then tilted and liquid collecting on the lower rim was removed by the pipette. For ESCA and GAP, this support was a polycrystalline gold foil of 0.1 mm thickness. The DASSA system that is dedicated to investigation of bulk amounts of liquids is operated with sample holders equipped with a liquid reservoir of 0.5 mm depth made of molybdenum or tantalum. Liquids were either spread onto the bottom of this reservoir as described above, or the reservoir was filled partly or completely, depending on overall requirements.

To prepare well-defined samples of ILs which are solid at RT, the sample holders were either heated by placing them onto a hot plate and the sample was then added to the solid support and allowed to melt and to re-crystallise. When molten, it was distributed evenly by a pipette tip or spatula. A second approach was dissolving the solid in an appropriate solvent and adding this solution to the support, followed by evaporation of the solvent in air and/or in UHV. A third option used for solids was fixing powdery samples to the support by XPS grade sticky tape patches.

Prepared samples were introduced within minutes into the load locks of the respective chambers and pumped down. The only exception are samples prepared by the solvent method. For the ESCA gold foil support and in some cases also for the DASSA reservoir sample holders, repeated adding of solution was necessary to obtain a solid film of sufficient thickness. For DASSA, the completely filled reservoir was left to evaporation in air rather than pumping it down immediately in order to prevent sample spill by sudden vaporisation in vacuum.

4. Surface composition of functionalised ILs

The option of tuning the properties of an IL by functionalisation is one of the reasons for persistent scientific interest and the basis for their applicability in many diverse fields. ILs were once termed designer solvents because their structural variability is nearly unlimited and can in principle be tailored according to the desired application.[7,16] Side chains of varying complexity can be attached to either anion or cation (or both) by established organic chemistry synthesis routes. Ionic structures can be achieved containing heteroatoms and functional groups, in principle in any thinkable combination, as long as the result is a stable liquid at the desired application conditions and has the required properties.

For many of the potential applications, interaction with the surrounding phases across the IL interfaces is of fundamental importance – catalysis of gas phase reactions, separation processes, selective gas capture or nanoparticle synthesis by sputter processes are cases in point. Thus, it is of interest to ascertain how functionalisation of an IL changes its surface composition. This is the topic of [P4] that summarises general rules for surface composition in functionalised ILs:

[P4] C. Kolbeck, I. Niedermaier, A. Deyko, K. R. J. Lovelock, N. Taccardi, W. Wei, P. Wasserscheid, F. Maier, and H.-P. Steinrück, *Influence of Substituents and Functional Groups on the Surface Composition of Ionic Liquids*, Chem-Eur J, 20, 14, 3954-3965, **2014**.

The main results of [P4] are discussed in Subchapter 4.1. In Subchapter 4.2 unpublished results on ferrocenyl ILs are summarised and the full details are given in Chapter A.1 of the Appendix. Further results related to surface composition are given in Section 7.2.

4.1. Effect of functionalisation on surface composition of ILs[P4]

The determination of general guidelines that describe surface composition of non-functionalised ILs was part of the early ARXPS results of our group. Generally, one can state that alkyl chains orientate towards the surface and form a non-polar overlayer above the charged headgroups if of sufficient lengths ($-C_nH_{2n+1}$ with $n \geq 4$)[11]. For different anions and the alkyl chains part of the cation, orientation is more pronounced for ILs containing smaller, more coordinating anions.[12] The huge number of ILs studied in [P4] allow to extend these findings to ILs containing functional groups. The studied ILs can be grouped into two units: imidazolium ILs methylated at the C2 position of the imidazolium ring (for atom numeration see Figure 2) that are compared to their non-methylated analogues, and ILs with side chains of varying

length on cation and/or anion with different functional groups. Of the latter unit, the majority are imidazolium ILs with the 3-position of the ring system functionalised. This short review will focus on these, but will also repeat overall findings for ILs containing the functional group as part of the anion or a cation different from imidazolium. The C2-methylated ILs will not be addressed here.

Figure 7 shows the differentially functionalised imidazolium cations (structures 4.2-4.8) reported on in [P4] together with the non-functionalised cation $[C_8C_1Im]^+$ (4.1). They are sorted into four groups by their degree of surface order as described in [P4]. The main finding of [P4] can be summarised as this: for ILs containing functionalised side chains, the degree of side chain order at the surface is mainly dependent on the degree of interaction between functional groups and ionic headgroups. Similar to non-functionalised dialkylimidazolium cations, the nonafluorohexylimidazolium cation (4.2) and the triethoxysilylpropylimidazolium cation (4.3) exhibit clear surface orientation with the functionalised side chain pointing towards vacuum. For the fluorinated compound, this result can be generalised to haloalkane side chains of different degree of halogenation for the haloalkane group part of either the cation or the anion, and the halogen being either fluorine or chlorine. Analogous results might be expected for iodated or bromated compounds or for not imidazolium-based halogenated cations, but experimental confirmation for this is still lacking. For F and Cl, the pronounced orientation effect is attributed to the rigid nature of the carbon-halogen bond with low polarizability. Halogenated units therefore behave similarly to alkyl moieties and the same factors as those stated for alkyl chains at the end of Section 2.3 are responsible for the pronounced surface enrichment: headgroups and halolkane moieties separate into polar and non-polar domains and at the surface, the haloalkane moiety is most favourably orientated towards the vacuum. In this uppermost layer the haloalkane chains only undergo very weak dispersive interactions with each other.

For imidazolium cations functionalised with the ethoxysilyl unit (4.3), the reason for the orientation is not so obvious. After all, the presence of oxygen suggest a certain degree of polarity and the possibility of ion-dipole or dipole-dipole interaction and hence, some interaction with the ionic groups is expected. Still, the finding is in line with an observed high surface activity of alkoxysilane compounds. Polysiloxane impurities of extremely low concentration below the detection limit of NMR are an annoying issue in IL samples intended for surface science investigations. Since the start of IL ARXPS studies, our group in collaboration with some of our suppliers[36] has worked on ways to avoid these impurities. Their most obvious source which is grease used to seal glassware joints has been abandoned by these groups years ago, but as the issue still occurs, albeit much more rarely, other likely sources include

slight contaminations of instruments, glassware, gas and vacuum lines as well as commercial reactants. The topic of siloxane contaminations is resumed in Chapter 8.

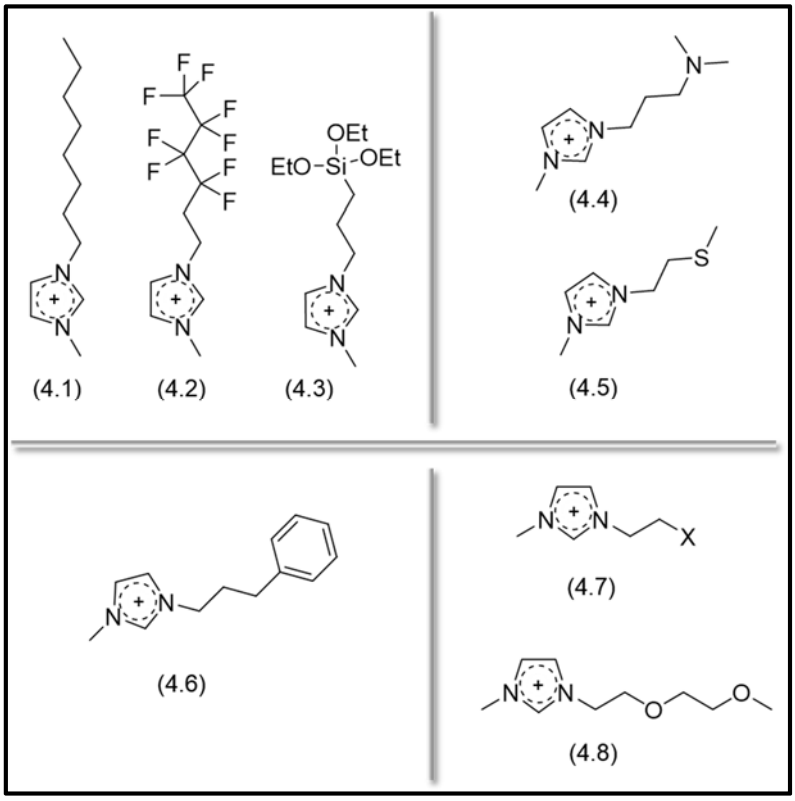

Figure 7: Imidazolium based cations containing different functional moieties attached to the 3-position of the ring. The depicted orientation of these functional units indicates their degree of surface ordering, from high (4.1-4.3) via intermediate (4.4, 4.5) and low (4.6) to structures exhibiting no orientation (4.7, 4.8).

Looking at amine-, thioether- and phenyl-functionalised cations, the degree of surface orientation of the functionalised side chain progresses from intermediate for the former two (4.4, 4.5) to low for the latter (4.6). For these, interactions between the functional group and the polar headgroup play an increasing role in attenuating surface enrichment. For amine and thioether, these interactions are mainly of the ion-dipole and dipole-dipole type that arise from the presence of the heteroatoms, nitrogen and sulphur. Similar to non-functionalised dialkylimidazolium cations, structure 4.6 also only contains carbon and hydrogen in the side chain. The fact that surface orientation of the phenyl ring is extremely low shows the dominance of π-π stacking interactions between the aromatic phenyl and imidazolium rings. One would expect this interaction to be larger between rings of the same kind, i.e. high phenyl-phenyl interaction that would still allow a considerable degree of orientation. The fact that this is not observed is likely caused by the predominance of the charge-carrying imidazolium ring in inducing interaction.

Both the haloethylimidazolium (4.7. with X = Br, Cl, I) and the ethylene glycol-functionalised cation (4.8) show no pronounced surface orientation. For the haloethyl cation, the lack of

surface orientation seems to contradict the findings reported above on halogenated structures such as 4.2. The reason for this discrepancy is likely related to the shorter chain length of compounds 4.7. Former studies on non-functionalised ILs with alkyl chains of different length also showed that surface enrichment is not observed by ARXPS if the side chains are too short.[11] For the poly(ethylene glycol) cation, the high electronegativity of oxygen when compared to nitrogen or sulphur results in increased interaction (hydrogen bonding) between this polar moiety and the headgroups that effectively suppresses any orientation effect.

Other important findings of [P4] are listed below:

1) The charged headgroups of anion and cation usually form a layer at a similar distance from the surface.
2) For an IL that contains one ion functionalised with a group that enriches at the surface such as a haloalkane unit, the enrichment of this group is enhanced if the second ion contains a long alkyl chain, e.g. the enrichment of the chloroalkyl moiety in $[C_8C_1Im][ClC_4SO_3]$ is enhanced when compared to that of $[C_2C_1Im][ClC_4SO_3]$.
3) For the same functional group attached to different cationic headgroups (e.g. imidazolium and ammonium), the degree of surface orientation depends on the headgroup type.
4) The very common $[Tf_2N]^-$ anion always shows a preferred orientation with both CF_3 groups pointing towards the vacuum and both SO_2 groups pointing towards the bulk.

4.2. Ferrocenyl-functionalised ILs

Several ILs containing a ferrocenyl-functionalised side chain at the 3-position of the imidazolium ring were also investigated with the ESCA setup. The linker unit that covalently bonds the ferrocenyl moiety to the imidazolium ring is either an amide, ether or alkyl. These ferrocenyl ILs were not included in [P4] because most of the samples contained a surface-active impurity, which complicated the determination of surface orientation effects. This impurity issue is revisited in Chapter 8.

Ferrocene is commonly used as a standard in electrochemical applications with a ferrocene/ferrocenium redox potential of 0.40 V against NHE.[37] These ferrocenyl ILs could thus potentially be used in a combined electrochemical/XPS experiment using the specific sample holder layout of either the ESCA or the DASSA described in 3.1 and 3.3. However, due to impurities being present in the samples such electrochemical experiments were not pursued further for these ILs.

A dominant surface-active impurity layer can render the determination of IL surface orientation impossible due to high damping of all but the impurity signals, especially for the surface sensitive 80° emission measurements. For these ILs, Argon sputtering was investigated to remove the impurity. Sputtering of liquid IL surfaces has been used before by our and other groups for removal of surface impurities on non-functionalised ILs (see Reference 38 and references therein). For these, but even more so for functionalised ILs that are more prone to beam damage, it is crucial to find a set of suitable sputter parameters that removes the impurity without damaging the IL severely. This is reported on in more detail in Chapter A.1 in the Appendix.

Sputtering was successfully carried out for most of the ferrocenyl ILs, although some still contained traces of an organic contamination. Sputtering generally introduces a degree of uncertainty into XPS results when only one single compound is investigated, as structural damage may not be eye-catching in the spectra, but still lead to subtle spectral changes influencing interpretation. However, in the present case, nine different ferrocenyl ILs were investigated by ARXPS to determine surface composition, some sputtered and some not. A general trend can be observed for all but one of the compounds investigated, which is a sign of reliability of the results.

According to the results of [P4] on IL surface composition discussed above, for the nonpolar ferrocenyl unit one could expect predominant orientation towards the IL surface in the case of low interaction with the headgroups. If either the amide or ether linkers or the π system of the cyclopentadiene (cp) rings that form the major part of the ferrocenyl unit interacted considerably with the ionic headgroups, a homogeneous arrangement at the outermost surface would be expected. The ARXPS data that is discussed in detail in the Appendix Chapter A.1.2 indicate the latter alternative of a more homogeneous surface composition. In contrast to the findings of [P4], however, the data also indicates that the ferrocenyl unit is orientated such that it lies below the charged headgroup of the anion, and possibly also below the headgroup of the cation. The reason for this behaviour which was not observed so far in other ILs is not clear, but could be due to the bulky size of the ferrocenyl group. For full confidence into these results, however, investigations of contamination-free ILs without pre-treatment have to be carried out. Furthermore, for an isolated determination of the preferred ferrocenyl orientation without superimposing effects that may result from the linker type or the linker length, alkyl-linked ferrocenyl ILs with an alkyl chain length with $n > 4$ would be essential.

5. Reactions at the IL-vacuum interface

In 2012, our group was the first to report the use of XPS for monitoring a reaction between two liquids in bulk amounts.[14,35] Because of the vacuum constraints, XPS is not a standard tool to study reactions in liquids, but it has some advantages over the classical techniques such as UV/Vis or NMR: it allows monitoring of all elements that are present within the reacting compounds – the only exceptions are H and He. The changes in electronic structure these elements undergo during course of the reaction are conveyed from changes in the chemical shift of the core levels of all elements. The reaction is studied *in situ*, so it is not necessary to remove part of the reaction mixture at certain time intervals or quench the reaction for investigation. Furthermore, density changes are directly reflected in intensities of the core level signals, and by using ARXPS, changes in the surface profile that go hand in hand with reaction progress can also be observed. The evolution of gaseous species is reflected in changes of the chamber pressure, and with a QMS attached to the chamber it is possible to qualitatively and quantitatively analyse the gas phase.

Due to the UHV requirement of XPS the method is, however, restricted to reactants with a low vapour pressure. That would in principle restrict its application to very few compounds indeed, as most liquids evaporate in UHV and would be pumped off the sample support before ever reaching analysis position. Functionalised ILs present a solution to this problem: by tethering reactive functional groups to polar headgroups and combining them with suitable counterions, new tailor made ILs are achieved that are able to carry out the desired reaction in UHV.

Further restrictions concern the time scale of the reaction. Even the best electron analyser needs a dwell time in the order of tenths of a second to acquire spectra with a signal to noise ratio sufficient to analyse the resulting signals. This leads to a measurement time of a at least one second per core level, so that for studying a reaction with several core levels of interest with XPS, reaction conditions need to be chosen such that intermediate steps also have a lifetime of at least several seconds or even minutes. In many cases, this can be controlled relatively easily by employing the relationship between reaction rate constant k and temperature T given in the Arrhenius equation when cooling down the reactive mixture:

$$k = A \times e^{\left(\frac{-E_a}{RT}\right)} \tag{4}$$

A second requirement is harder to meet: it must be possible to trigger the start of the reaction at a defined point in time within the chamber. The challenge lies in the fact that introducing a reaction mixture into the UHV chamber requires one to several hours. During this transfer time, with our XPS setups available, no temperature manipulation and especially no cooling of the

sample is possible. For reactions such as the pioneering study reported in 2012[14,35], where reaction rate is low, triggering is easily done by heating up the reaction mixture once it is within the XPS chamber to a temperature that ensures a time interval of a few hours from start to completion of the reaction. Unpublished results in Section 5.1 will, however, show that it can be quite tricky to handle a reactive mixture in a way that it is possible to follow the complete reaction by XPS, that is, WITHIN the chamber. In the results described in 5.1, an attempt was made to carry out a liquid-liquid reaction similar to the pioneering study in 2012 by mixing two reactive ILs outside the XPS chamber, and triggering the reaction after introduction into the chamber by heating up the mixture.

Of course, there is a different approach to this problem: reaction start can be triggered much more precisely if both reaction partners can be brought together at a defined point in time when already within the XPS chamber. This approach does exclude the addition of bulk amounts of any compound. But it is possible to dose gaseous reagents at low partial pressures onto an IL already within the UHV chamber. Solids and liquids can be provided in the same way via the gas phase after evaporation. Reagents added in this way will interact with the uppermost surface of the IL, so that the resulting reaction will take place within the IL region that is accessed by XPS.

Using this approach, the reaction of the gaseous acid TfOH with the basic anion of the IL $[C_2C_1Im]Cl$ is studied *in situ* in Section 5.2. As reaction onset is precisely controlled, the resulting anion metathesis can be followed by XPS from the start. In Section 5.3, an IL that reacts with gaseous CO_2 to form carbamation products is investigated. This investigation was carried out with the near-ambient pressure XPS setup GAP that allowed application of a CO_2 background pressure as high as 0.9 mbar during the XPS studies. Again, the reaction could be followed over all time intervals of interest as the CO_2 flow could be started and stopped as desired.

The respective papers and the SI can again be found in the Appendices:

[P2] I. Niedermaier, N. Taccardi, P. Wasserscheid, F. Maier, and H.-P. Steinrück, *Probing a Gas/Liquid Acid-Base Reaction by X-ray Photoelectron Spectroscopy*, Angew Chem Int Edit 52, 34, 8904-8907, **2013**.

[P3] I. Niedermaier, M. Bahlmann, C. Papp, C. Kolbeck, W. Wei, S. Krick Calderón, M. Grabau, P. S. Schulz, P. Wasserscheid, H.-P. Steinrück, and F. Maier, *Carbon Dioxide Capture by an Amine Functionalized Ionic Liquid: Fundamental Differences of Surface and Bulk Behavior*, J Am Chem Soc 136, 1, 436-441, **2014**.

5.1. Halogen exchange

As a follow-up on the pioneering *in situ* reaction study by XPS in 2012[14,35], it was attempted to study halogen exchange reactions of the type shown in Scheme 1. The cation of one IL that is terminally functionalised with either Br or I reacts with a halide anion of a second IL, resulting in halogen exchange via an S_N1 reaction. As in UHV the reaction proceeds under solvent free experimental conditions, solvent effects determining equilibrium can be excluded and the equilibrium of this reaction depends mainly on the leaving group ability of the participating halogens. The leaving group ability decreases in the order I > Br > Cl.[39] Thus, for this reaction, the equilibrium constant is K >> 1 and the equilibrium lies far to the right if the halogen covalently bonded to the cation of the first IL has a higher leaving group ability than the halogen forming the anion of the second IL. Possible combinations are therefore X = Br and Y = Cl, X = I and Y = Cl as well as X = I and Y = Br.

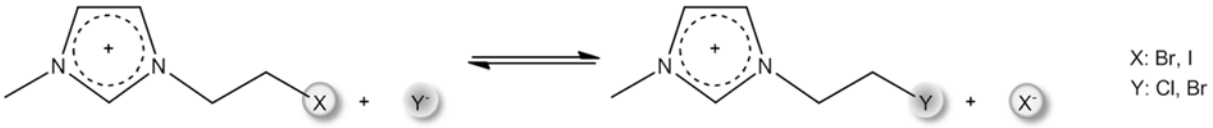

Scheme 1: Halogen exchange reaction in an IL mixture where X and Y are halogens.

The rate determining step in such S_N1 reactions is typically the breaking of the C-X bond forming the free halide X^- and a carbocation, while the following nucleophilic attack by the second halide Y^- is much faster. As the breaking of the C-X bond is endothermic, increasing the reaction temperature will also lead to an increase in K, thus shifting the equilibrium even further to the right hand side of the Scheme 1 equation.[39] Monitoring such a halogen exchange by XPS is expected to be straightforward as covalently bonded and anionic halogens show a clearly differentiable chemical shift. Also, the counterions of both ILs that are mere spectators can be chosen such that they do not superimpose the signals of the reacting species, and temperature control of reaction rate and equilibrium position should be possible.

Two attempts to carry out the reaction with X = I and Y = Br are shown below to highlight problems with monitoring such a reaction by XPS. The data shown is exemplary for other reactions with different halogen combinations that were also tested as well as for other reactions with similar reaction rates. In Figure 8, the normal emission I $3d_{5/2}$ and Br $3d_{3/2,\ 5/2}$ (in short, Br 3d) core level spectra of two experiments of the reaction of $[(IC_2)C_1Im][Tf_2N]$ and $[C_2C_1Im]Br$ to form $[(BrC_2)C_1Im][Tf_2N]$ and $[C_2C_1Im]I$ are given. The spectra of experiment 1 and experiment 2 are shown at the top and at the bottom, respectively. The scheme at the top of the figure shows the desired reaction and also the spectator ions $[Tf_2N]^-$ and $[C_2C_1Im]^+$ that form the counterions of both reactants.

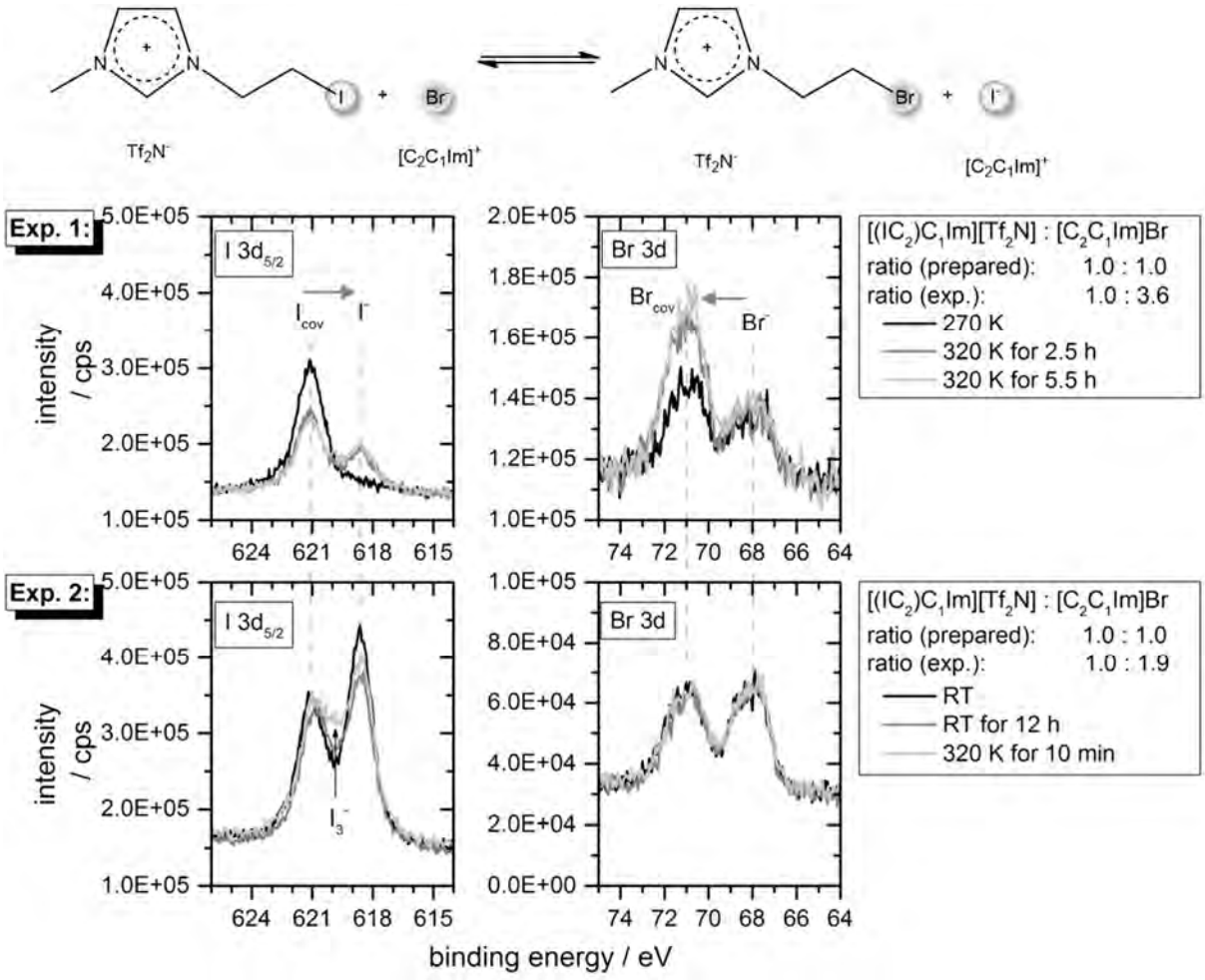

Figure 8: Two attempts to monitor the halogen exchange reaction of $[(IC_2)C_1Im][Tf_2N]$ and $[C_2C_1Im]Br$ to form $[(BrC_2)C_1Im][Tf_2N]$ and $[C_2C_1Im]I$. Top spectra: I $3d_{5/2}$ and Br 3d core level of experiment 1, bottom spectra: I $3d_{5/2}$ and Br 3d core level of experiment 2. All spectra are taken in normal emission with the ESCA setup.

The first issue arises with the ratio of both components. For both experiments, the ILs were mixed in a 1 : 1 molar ratio determined by mass according to nominal molecular mass. As can be seen in the legends for both experiments, the experimental ratio determined by the ASF corrected ratio of the I $3d_{5/2}$ and the Br 3d signal ("ratio (exp.)") differs widely from this: it is 1.0 : 3.6 (I : Br) for experiment 1 and 1.0 : 1.9 (I : Br) for experiment 2. The reasons for this discrepancy can be related to the high hygroscopy of halogenated ILs. Crystal water is part of the IL weighed out in air, but evaporates in UHV, leading to large differences between IL mass in air and IL mass in UHV. Also, to ensure proper mixing of both components, acetonitrile (ACN) was used as a solvent that evaporates once the sample is brought into UHV, leaving the pure IL mixture behind. For the tiny amounts in the 1 mg region used to prepare the IL mixtures for XPS, solubility of the IL in the solvent chosen is not easily determined by eye. A seemingly homogeneous solution can still contain undissolved species, so that during transfer of the solution onto the sample holder, the less well dissolved component is left behind in the sample vial, and the stoichiometry of the mixture on the sample holder changes drastically

when compared to that in the vial. This behaviour is likely the main reason for the discrepancy observed here with the halogenated IL $[(IC_2)C_1Im][Tf_2N]$ being less well soluble in ACN. In experiment 2, about a 10 times higher amount of solvent was used for mixture preparation, which obviously improved the situation, but did not completely solve the problem. Determination of an appropriate solvent or solvent mixture would have been required, but was not possible with the very low amounts available of these specifically synthesised ILs. In addition, the observed surface depletion of the halide anions described below also introduces an error into stoichiometric determination. This effect is also hard to quantify.

For both experiments, the black spectra give the initial situation, i.e. the first spectrum recorded once the mixture was introduced into the UHV chamber. For experiment 1, the freshly prepared mixture was cooled in the sample vial and also the manipulator was pre-cooled so that the mixture reached a temperature of 270 K as soon as it was transferred to the sample holder position on the manipulator. As noted above, no cooling is possible during sample introduction, so that the experiment 1 sample also returned to RT for 1 h in between preparation and 1st measurement. For experiment 2, the mixture was at RT for the complete time period of sample preparation until recording of the first spectrum.

In the spectra, the peak position of the covalently bonded species (I_{cov} or Br_{cov}) is marked, and also the anionic halide position (I^- and Br^-). The arrows in the spectra of experiment 1 indicate the direction of intensity shift expected during reaction. Initially, a Br^- peak and a I_{cov} peak should be present that both decrease in intensity during reaction, while new peaks emerge and increase at the Br_{cov} and the I^- position. The initial (black) spectra show that for both experiments, the reaction has already started, and it is already far advanced for experiment 2, as both the Br 3d spectrum and the I $3d_{5/2}$ spectrum of experiment 2 clearly reveal two peaks at the respective covalent and ionic positions. Cooling both sample vial and manipulator obviously helped slowing down the reaction in experiment 1, as the intensity shift in the I $3d_{5/2}$ spectrum is much further advanced in experiment 2 where no cooling attempts were made. Obviously, for reactions with such low activation energy barriers, full reaction monitoring by XPS is impossible without a complete cooling chain in order to slow down the reaction rate sufficiently.

Two more issues are visible in the spectra. For experiment 2, after heating the mixture to 320 K, a third peak arises in the I $3d_{5/2}$ region in between the covalent and the ionic signal at approximately 620 eV. This likely results from triiodide (I_3^-), which under ambient conditions typically forms from molecular iodine (I_2) and iodide.[40] Thus, increasing the temperature in experiment 2 does not induce further halogen exchange as desired, but leads to a side-reaction.

For experiment 1, heating to 320 K indeed is followed by further halogen exchange, as can be seen in the decrease of the I_{cov} peak, the emergence of the I^- peak and the increase in the Br_{cov} peak. However, in addition to halogen exchange, a second process must take place. For halogen exchange alone, one would expect to see a Br^- decrease that matches the increase of Br_{cov}. Similarly, the changes in the I_{cov} and the I^- signals should have the same magnitude, but the decrease in the I_{cov} signal is slightly higher than the increase of the I^- signal. This mirrors a well-known feature observed for IL mixtures with very differently sized anions such as monoatomic halides combined with $[Tf_2N]^-$:[4,41] the small anions are surface-depleted to such an extent that it is notable even in the 0° spectra, i.e. under conditions where XPS averages over about ten IL layers.

For the initial reaction mixture containing Br^- and $[Tf_2N]^-$ anions, the same effect is likely also observed and Br^- is surface-depleted to the benefit of $[Tf_2N]^-$. During conversion of Br^- to covalently bonded Br, reacted surface Br^- is replenished from the bulk, leading to a constant Br^- peak intensity. The I^- anion possibly shows a similar behaviour: upon formation of ionic I^- from covalently bonded I, the ion remains at the surface until a certain concentration limit is reached, and thereafter any excess is depleted from the surface into the bulk. However, the effect in the I $3d_{5/2}$ signals is less pronounced than for Br 3d. Therefore, a definite statement is not possible. As the signal intensities of the ionic Br^- and I^- peaks differ in experiment 1 and 2, it is possible that the surface content of halide ions depends on some of the factors that differ in between both experiments. Possible factors include the stoichiometric ratio of both components that may also influence the density of the IL mixture, or the temperature history of the sample.

Although this replenishing of the Br^- anion in the surface near region and the likely depletion of I^- ions upon formation in excess is in itself a spectacular finding, it complicates extraction of isolated information on the halogen exchange reaction. Quite generally, the fact that reaction monitoring by *in situ* XPS generates an all-embracing picture of processes that take place during the reaction can be an advantage, as in Section 5.2 and [P2] where determination of reaction progress as well as variations in density and in electronic structure give a comprehensive picture of the course of events. It can, however, also be unfavourable if a process of interest cannot be extracted due to superimposing effects such as preferential segregation processes.

5.2. An acid-base reaction studied by XPS[P2]

To circumvent the time delay between bringing reaction partners into contact by *ex situ* mixing and the first XPS measurement, a more favourable approach is introduction of one component into the vacuum chamber and subsequently adding the second one *in situ* within the UHV system. For a liquid-liquid reaction with one reagent being a UHV stable IL and the other a high vapour pressure liquid, this is most easily accomplished by vaporising the latter and dosing it onto the IL surface. With this approach, the starting point of the reaction is clearly defined and recording of spectra can be timed accordingly.

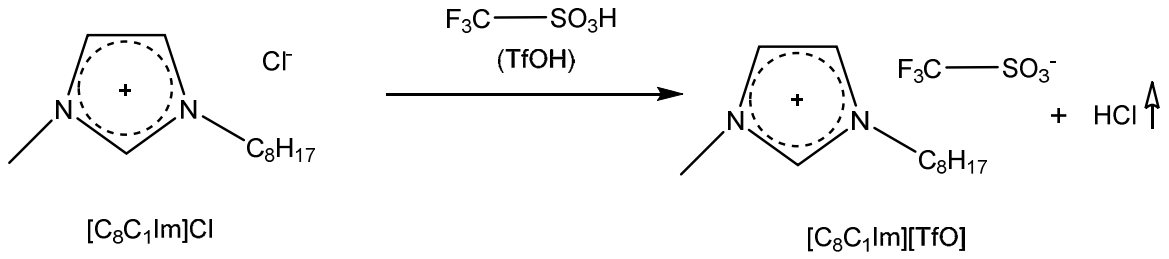

Scheme 2: The acid base reaction between the chloride anion of $[C_8C_1Im]Cl$ and vaporised triflic acid described in [P2].

This approach was used for the reaction detailed in [P2], namely a Brønstedt acid-base reaction between the weakly basic anion of $[C_8C_1Im]Cl$ and the strong trifluoromethanesulfonic (triflic) acid TfOH (F_3CSO_3H), as shown in Scheme 2. This reaction is used in IL synthesis for anion exchange[42] and is thus of general interest. However, apart from that, *in situ* XPS gives a comprehensive picture of the multiple processes that take place even during this relatively simple reaction. Figure 9 reproduces the central figure of [P2] and gives the changes of all core level spectra over dosage time of TfOH from top to bottom. Clearly, during the course of the reaction from 0 to 170 min dosage time, the Cl 2p doublet attributed to the anion of the reactant IL decreases, showing that this ion is neutralised by protonation and the formed volatile HCl is pumped off the system. The acid TfOH, on the other hand, donates its proton and forms the $[TfO]^-$ anion. Being thus stabilised in UHV it replaces Cl^- as the IL anion, as can be deduced from the emergence and increase of core level peaks associated with all $[TfO]^-$ species, namely F 1s, O 1s, S 2p and C_{anion}.

The XPS analysis does not only reflect the proton transfer, but also the fact that a monoatomic and therefore small anion (Cl^-) is replaced by a much more bulky one ($[TfO]^-$). This results in an overall density decrease (if one defines density as number of IL pairs per volume unit). As XPS analyses a fixed IL volume, this density decrease is directly reflected in an overall decrease in cation signal intensity during reaction, although the cation itself does not take part in the actual reaction (see N 1s and main feature in C 1s). Furthermore, the coordination of the

small Cl^- anion to the cation is different to that of $[TfO]^-$, as has been described in Reference 43. This results in a decrease in electron density induction onto the cation during course of the reaction, which is visible in a shift of the signals associated with the positively charged moiety of the cation, namely the N 1s and the C_{hetero} signal both originating from the imidazolium ring.

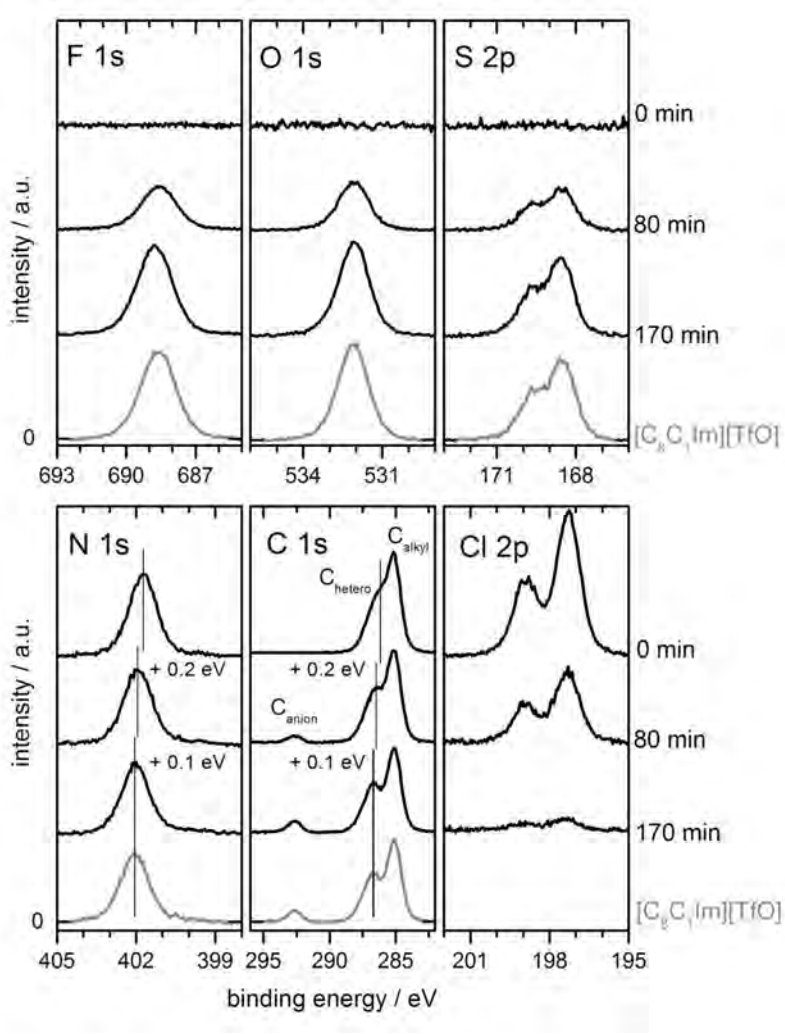

Figure 9: Changes in all core level spectra during the reaction of the IL $[C_8C_1Im]Cl$ with vaporised triflic acid TfOH (p_{TfOH} = 1x10^{-6} mbar) at RT. The grey spectra reproduce a reference measurement of $[C_8C_1Im][TfO]$ for comparison with the spectra of the reaction product. The spectra were recorded with the ESCA setup at normal emission.

The reaction proceeds close to completion in 170 min at a gas pressure of p_{TfOH} = 1x10^{-6} mbar at RT, as can be deduced from the fact that the Cl 2p signal originating from the anion of the reactant IL nearly vanishes over time to a residual signal of ~9 % the intensity at 0 min acid dosage. The product formed is indeed $[C_8C_1Im][TfO]$, as shown by a comparison with the reference spectra in grey. In [P2] it could further be shown that this reaction is restricted to the topmost IL layers accessed by XPS only: when heating the sample after completion of the reaction, the signals associated with the $[TfO]^-$ anion start to decrease while the Cl 2p signal associated with the Cl^- anion of the reactant IL again increases (for spectra see [P2]). This

cannot be due to a back reaction of the products HCl and $[C_8C_1Im][TfO]$ to again form the reactant IL $[C_8C_1Im]Cl$, as the gaseous HCl is immediately removed from the sample site by the continuous pumping of the UHV system. Therefore the observed changes result from enhanced diffusion at elevated temperatures, allowing unreacted $[C_8C_1Im]Cl$ from the bulk to ascend to the surface, where it is again detected by XPS.

5.3. Chemical absorption of CO_2 by an amine-functionalised IL[P3]

Since carbon dioxide (CO_2) has been identified as one of the potential factors for global warming, development of its atmospheric levels has been closely investigated and increasing use of fossil fuels since the industrial revolution has been identified as the main factor responsible for its enhanced release. The resulting rise in mean global temperature is feared to bring about extreme meteorological events and rising ocean levels with detrimental effects for worldwide food harvest, drinking water resources and available living space.[44]

At the moment of writing this chapter (30/11/15), the 2015 Paris Climate Conference (COP21) opens its doors. While former climate summits failed to produce a mutual consent on actions to limit the worldwide average temperature increase to 2 °C and conclusive plans on how to achieve this goal, the 2015 conference is hoped to be a milestone in worldwide agreement on climate control plans with a binding outcome for all participating countries.[44,45]

Strategies to diminish CO_2 emissions include more energy efficient processes or an active reduction of atmospheric CO_2 levels by e.g. afforestation.[46] In addition, developed countries for years have investigated the possibility of reducing CO_2 emissions at the major sites of production, i.e. at industrial facilities or power plants.[46] There are three possible CO_2 capture and storage (CCS) techniques, namely post-combustion CO_2 removal, pre-combustion CO_2 removal and the oxy-fuel process.[46,47] Of these, the first mentioned is especially suitable for retrofitting existing plants and also is the most developed process.[47]

The post-combustion process aims to remove CO_2 from flue gases of fossil fuel combustion prior to emission of these into the atmosphere. The most developed of the separation technologies are CO_2 adsorption on solids such as carbonaceous materials or zeolites or absorption in liquids. Thereby physical or chemical absorption is possible.[48]

In general, two vital steps are part of the process: CO_2 uptake at the flue gas site and later CO_2 release in pure form for further storage or utilisation with at best complete absorbent recovery.[47,49] The optimal absorbent would undergo these two steps with minimum energy requirements.[49] This would include uptake of the maximum possible CO_2 amount at the

elevated temperature of the flue gas without need of cooling, and complete CO_2 release with the necessary temperature enhancement and/or pressure reduction as low as possible.

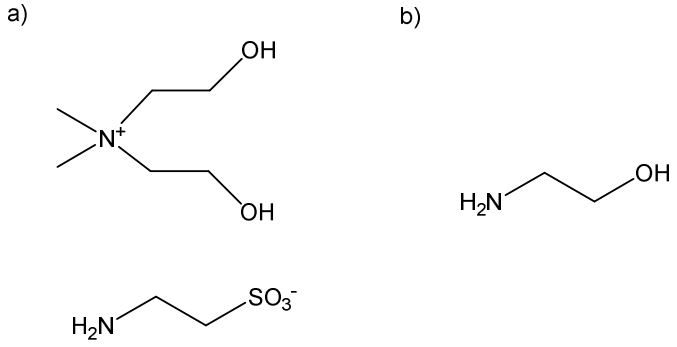

Figure 10: a) IL di(hydroxyethyl)dimethylammonium taurinate investigated for its CO_2 absorption ability in [P3]. b) MEA (monoethanolamine) that in spite of some severe drawbacks is already in use for CO_2 absorption processes.

Amines such as monoethanolamine (MEA, see Figure 10b) have been shown to be successful CO_2 absorbents, but when operating in post-combustion flue gas cleaning processes, their high energy demands for CO_2 release is a remaining unsolved issue.[48,50,51] In addition, they feature low stability under elevated temperatures which makes them prone to evaporation, degradation and corrosion in the flue gas stream.[50,52] Several researchers have proposed amine-functionalised ILs as potential MEA replacements due to their well-known advantages such as high thermal stability and low vapour pressure.[50-52] The paper [P3] given in the Appendix set out to investigate the processes that take place at the IL-gas interface for such an amine-functionalised IL during CO_2 absorption and the species formed during this reaction. The results on the interface processes obtained by NAP XPS are compared to bulk uptake measurements and bulk sensitive IR investigations of the IL.

The investigated IL di(hydroxyethyl)dimethylammonium taurinate $[(HOC_2)_2Me_2N][H_2NC_2SO_3]$ given in Figure 10a mimics MEA. Its anion is functionalised with a primary amine and the cation is hydroxylated. The IL undergoes a reaction with CO_2 identical to the reaction of simple amines such as MEA that proceeds in three steps, as shown in Scheme 3. The amine and CO_2 first form the intermediate carbamic acid (R-NHCOOH, step 1) which subsequently may be deprotonated to form carbamate ($R\text{-}NHCOO^-$, step 2). The proton is transferred to another amine molecule to form ammonium ($R\text{-}NH_3^+$, step 3).[49] The overall reaction is given as step 4. Depending on reaction conditions the deprotonation of carbamic acid is either favoured or not, so that either carbamic acid or carbamate is the predominant reaction product (see [P3] for a detailed discussion of these conditions). Stabilisation of carbamic acid would be advantageous in terms of CO_2 uptake capability, as one mole of amine can bind one mole of CO_2 in the carbamic acid form (1 : 1 uptake). For the full reaction to carbamate, to bind one mole of CO_2 two moles of amine are required, as the amine also acts as proton acceptor (1 : 2 uptake).[49]

$$R\text{-}NH_2 + CO_2 \longrightarrow R\text{-}NHCOOH \quad (1)$$

$$R\text{-}NHCOOH \longrightarrow R\text{-}NHCOO^- + H^+ \quad (2)$$

$$R\text{-}NH_2 + H^+ \longrightarrow R\text{-}NH_3^+ \quad (3)$$

$$2\ R\text{-}NH_2 + CO_2 \longrightarrow R\text{-}NHCOO^- + R\text{-}NH_3^+ \quad (4)$$

Scheme 3: Reaction of primary amines and CO_2 to form the intermediate carbamic acid (R-NHCOOH) in step (1), which may then transfer a proton to a second amine molecule to form carbamate ($R\text{-}NHCOO^-$) and an ammonium in steps 2 and 3. The overall reaction is shown as step 4.[49]

For XPS analysis, it is important to note that the N 1s signals that originate from amine, carbamate and carbamic acid are very close in BE. All these N atoms are uncharged and have very similar chemical environments. Hence the resulting peaks are superimposed and cannot be differentiated. However, the positively charged N atom of ammonium gives rise to a peak clearly shifted to higher BE, so that it is possible to indirectly differentiate between carbamate (with accompanying ammonium formation) and carbamic acid (without ammonium formation).

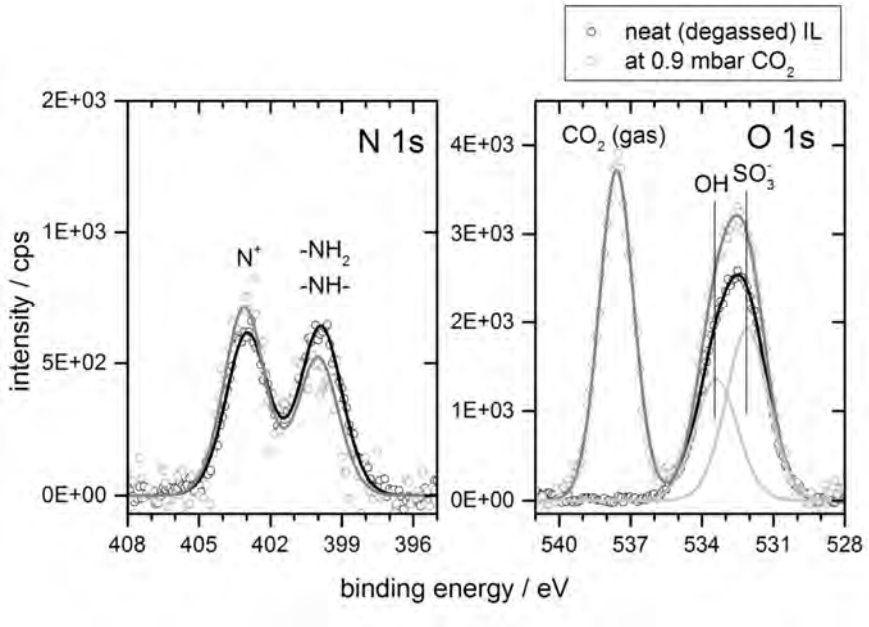

Figure 11: XP spectra of the IL $[(HOC_2)_2Me_2N][H_2NC_2SO_3]$ before (black) and during (grey) application of CO_2 at a partial pressure of 0.9 mbar. The grey spectra are intensity corrected as signals are subject to damping by the gas phase, as described in [P3] (Experimental Section). Fit peaks for O 1s are shown in light grey. All spectra were recorded with the GAP setup.

Figure 11 gives in black the N 1s and O 1s spectra of the neat IL prior to CO_2 application preheated to remove any products that result from reaction with atmospheric CO_2. It shows two signals of 1 : 1 intensity resulting from the ammonium atom of the cation (not taking part in the reaction with CO_2) at 403.0 eV and from the primary amine group of the anion at 399.9 eV. The O 1s region shows a broad signal with contributions from both OH groups of the

cation and the three equivalent O atoms of the anionic sulfonate group. All these species do not take part in the reaction.

During application of 0.9 mbar CO_2 (grey spectra), the cation ammonium peak gains intensity, indicating the formation of an ammonium zwitterion from the anion (H_3N^+-$(CH_2)_2$-SO_3^-) that is a clear sign of simultaneous carbamate formation. The amine signal decreases by the same amount. The N 1s signals of the formed carbamate and carbamic acid superimpose the amine peak and thus cannot be quantified directly. Carbamate formation, however, can be quantified indirectly by the ammonium zwitterion to 15 %, i.e. 0.15 mole of the IL anion react to form ammonium and further 0.15 mole react to form carbamate. The overall degree of carbamation can be determined from the increase of the O 1s signal that translates into an uptake of 0.58 mole CO_2 per mole IL. The amount of carbamic acid formed is thus approximately 0.58 – 0.15 = 0.43 mole. Within the near surface region (7-9 nm) carbamic acid is therefore the dominant carbamation product at a pressure of 0.9 mbar CO_2.

In [P3] this overall formation of 15 % carbamate and 43 % carbamic acid in he surface near region of the IL is compared to bulk uptake determined by absorption isotherms and to the species formed in the bulk determined by IR spectroscopy. It could be shown that the amount of CO_2 absorbed at the surface region is considerably higher than the overall bulk uptake. At the partial CO_2 pressure of 0.9 mbar used for the XPS *in situ* experiments, surface uptake was nearly six times higher than bulk uptake at a partial CO_2 pressure of 0.7 bar (700 mbar), which was the lowest pressure investigated for the isotherms. Furthermore, at pressures up to 2.5 bar the product species in the bulk was found to be solely carbamate, while at the surface it is mainly carbamic acid.

Thus, for CO_2 absorption with amine-functionalised ILs it is advantageous to generate a surface to bulk ratio as high as possible by minimising IL droplet size for two reasons: the predominant surface species (carbamic acid) can intrinsically bind twice the amount of CO_2 when compared to carbamate, due to the 1 : 1 uptake ratio of carbamic acid when compared to the 1 : 2 uptake ratio of carbamate. Also, CO_2 surface uptake is in general much higher than bulk uptake, which is likely a consequence of diffusion limitation of carbamation products into the bulk. The predominance of carbamic acid is likely a consequence of maintaining as low as possible surface charges, so that the singly charged carbamic acid anion is preferred over the dianionic carbamate.

6. The DASSA spectrometer[P5]

This chapter focusses mainly on the unique spectrometer DASSA (Dual Analyser System for Surface Analysis, see 3.3) that was obtained by our group at the beginning of 2014 and is described extensively in [P5]:

[P5] I. Niedermaier, C. Kolbeck, H.-P. Steinrück, and F. Maier, *Dual Analyzer System for Surface Analysis dedicated to angle-resolved photoelectron spectroscopy at liquid surfaces and interfaces*, Rev Sci Inst, 87, 4, 45105, **2016**.

Apart from a description of the major feature, the dual analysers, also unpublished results obtained with DASSA so far will be given here and in Chapter 7.

6.1. Dual analyser spectroscopy

The previous chapters gave a broad overview on the wealth of information on liquid surfaces that can be obtained by XPS. Especially for the results given in Chapter 4, ARXPS was employed to obtain information about orientation and enrichment effects. To use ARXPS, i.e. to vary the angle between the sample surface normal and the analyser, it is necessary to tilt the sample by means of a rotatable manipulator to angles of ~70-85° relative to its normal emission orientation. The problem with rotating liquid samples is obvious: they may drip off the support. This problem can be circumvented by using relatively thin films (up to ~100 µm) of ILs. Due to the high viscosity of most ILs such films remain rather stable and allow rotation by 360° without loss from the support – indeed this is the method used for sample preparation for the ARXPS results given in Chapter 4 (see Section 3.6 for description of film preparation).

The problem, however, remains for low viscous samples or film thicknesses higher than 100 µm. The latter becomes necessary if e.g. an electrochemical cell setup is to be used on the sample holder (see sample holder descriptions under 3.1and 3.3) or if investigations with varying liquid surface-to-support distances are carried out, which can contribute to answer open questions on charge transport within ILs. A pilot study on this is described in detail in [P5].

The core feature of the unique DASSA spectrometer are two identical electron analysers mounted at fixed electron emission angles of $\vartheta = 0°$ for normal emission and $\vartheta = 80°$ for grazing emission for a horizontal sample. The schematic overview of the DASSA analysis chamber in Figure 12 shows the orientation of both analysers towards the central sample. Analyser A records spectra at $\vartheta = 0°$ and analyser B at $\vartheta = 80°$. A and B are mounted such that their energy

dispersive directions are orientated along polar sample rotation. This orientation ensures the minimum acceptance angle for normal and grazing emission data and thus a well defined emission angle for ARXPS.

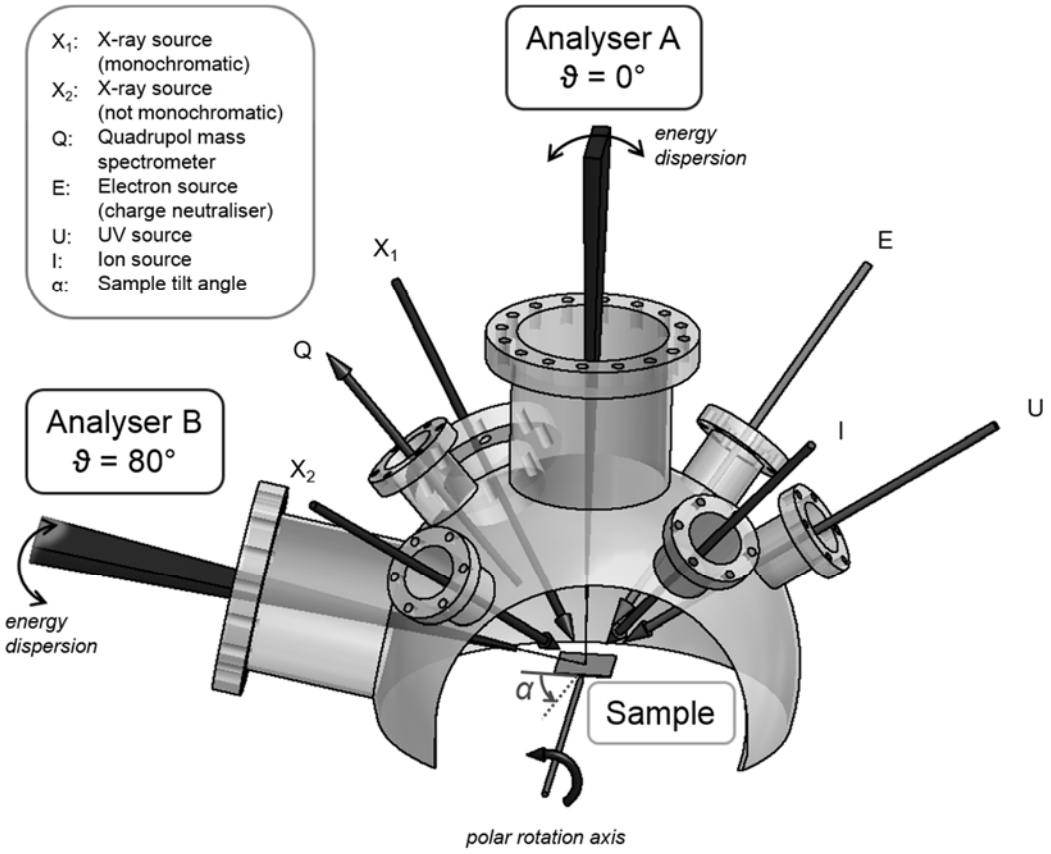

Figure 12: Layout of the DASSA analysis chamber with the two electron analysers at 0° (analyser A) and 80° geometry (analyser B), and with the four excitation sources X_1, X_2, U and I (see abbreviation list above) and further components.

The arrangement of all other components in the analysis chamber is also shown in Figure 12. Most importantly, it contains a monochromatic X-ray source (X_1, Al Kα, E = 1486.6 eV) capable of spot or line irradiation (spot size ~1 mm). The monochromator ensures much improved spectral resolution when compared to the ESCA or GAP XPS setups. Chapter 7 gives some examples on how minor variations in electronic structure can be visualised by this superior resolution. There is also a dual X-ray source (X_2, Al Kα, E = 1486.6 eV or Mg Kα, E = 1253.6 eV) with both X-ray sources mounted at magic angle geometry (54.7°)[73,74] towards each of the analysers. DASSA also contains a UV source (U) and an ion source (I), enabling further surface sensitive investigations such as angle-resolved ultra violet photoelectron spectroscopy (ARUPS) or low energy ion scattering (LEIS).

6.2. Synchronous spectra recording

Apart from the main advantage of DASSA, namely that samples do not have to be tilted for ARXPS, there is a further huge bonus: spectra at normal and grazing emission are recorded simultaneously. This is enabled by a special 'dual' version of the measurement software MATRIX T3.2 that addresses the lens system of both analysers at the same time with identical parameters and displays the received intensity information of both detectors as separate spectra side by side. The software window of the dual MATRIX version is shown in Figure 13. This synchronous recording ensures that all differences observed between spectra of the two angles result from the angle-resolved nature of the experiment alone, and are not a consequence of time dependent changes of the sample.

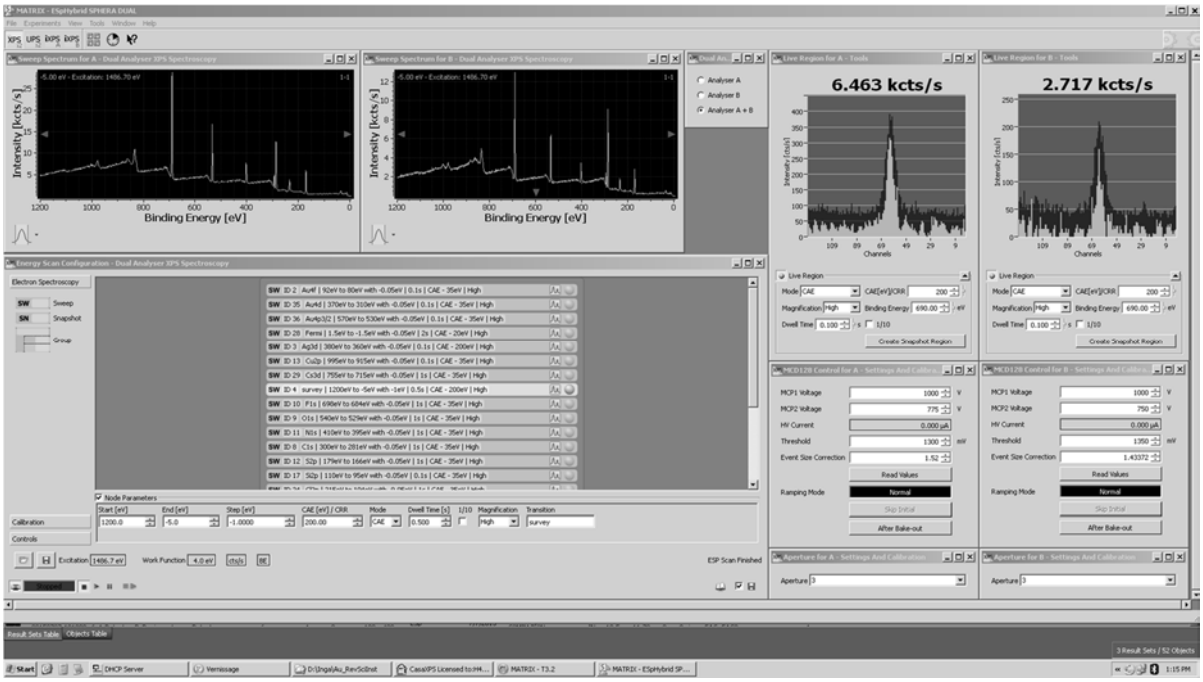

Figure 13: Software window of the especially configured dual MATRIX T3.2 version. Spectra of analyser A and B are displayed side by side (top region to the left; left: A, right: B). There are also two simultaneously activatable live view windows (right) that enable quick previewing of snapshot regions for both analysers. Measurement parameters only have to be entered once and are used identically to actuate the lenses of both analysers.

The following examples show the importance of this condition, especially for investigations of functionalised ILs. While non-functionalised ILs are relatively stable to X-ray irradiation[29] and do not show pronounced spectral changes even after 15 h of X-ray exposure ($P_{x\text{-}ray}$ = 250 W, Al Kα), more reactive functional groups are also more susceptible to changes triggered by irradiation. Under typical XPS conditions, some functionalised ILs only exhibit unchanged spectra for exposure times below 1 h. The following graph (Figure 14) shows spectral changes that occur in functionalised ILs as a consequence of X-ray irradiation (compare black spectra recorded initially and grey spectra recorded after several hours of exposure to X-ray). The

ferrocenyl-functionalised IL [(FcCOC$_3$)C$_1$Im][Tf$_2$N] that is described in more detail in Chapter A.1 (Appendix) shows clear signs of degradation after 5 h of X-ray exposure ($P_{X\text{-}ray}$ = 250 W, Al Kα), notable in a second F 1s peak that emerges shifted to lower binding energy of half the intensity than the original F 1s peak. The initial Fe 2p doublet of the Fe^{II} species decreases in intensity, while a second, broader doublet attributed to Fe^{III} becomes visible.

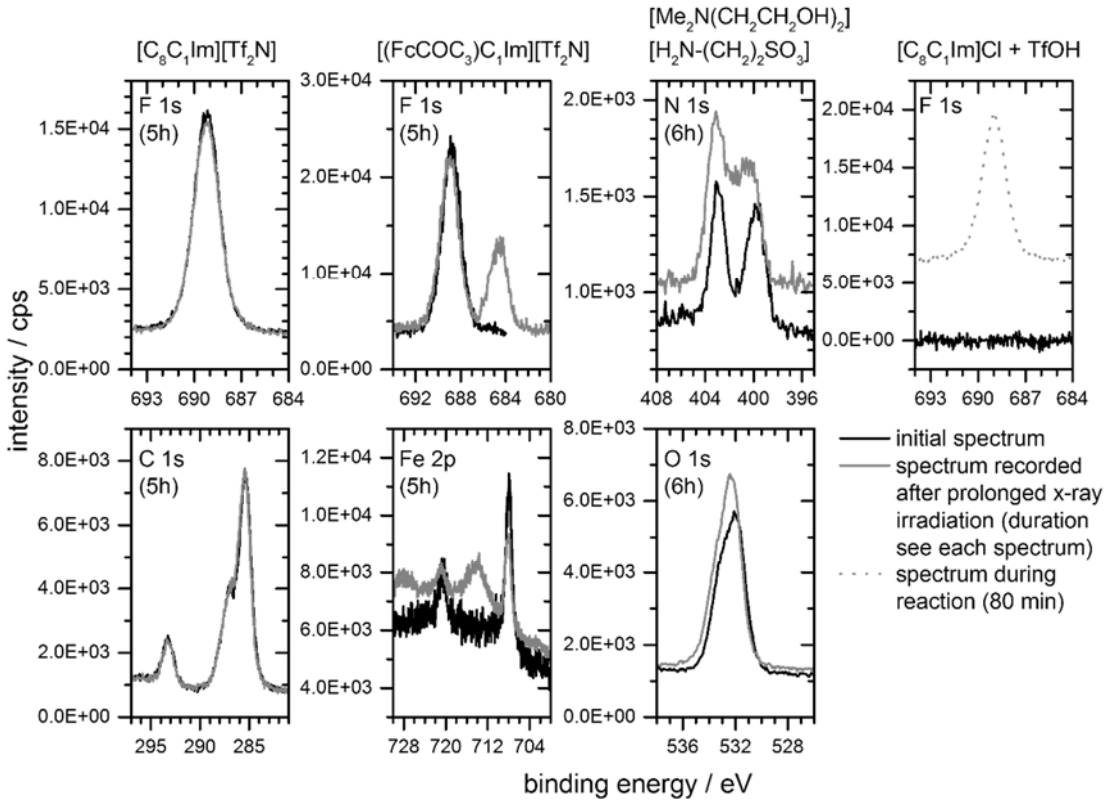

Figure 14: Spectral changes under X-ray exposure (compare black and grey spectra). While non-functionalised ILs such as [C$_8$C$_1$Im][Tf$_2$N] (left top and bottom) show no pronounced changes, functionalised ILs often show X-ray induced degradation, such as the ferrocenyl functionalised IL [(FcCOC$_3$)C$_1$Im][Tf$_2$N] (second from left) or the amine functionalised IL [(HOC$_2$)$_2$Me$_2$N][H$_2$NC$_2$SO$_3$] (second from right). When monitoring reactions (right, [C$_8$C$_1$Im]Cl + TfOH), changes in successive spectra are also large. Spectra were recorded with the ESCA setup apart from those of [(HOC$_2$)$_2$Me$_2$N][H$_2$NC$_2$SO$_3$] which were recorded with the GAP setup.

The IL used for the CO_2 absorption experiments described in 5.3 is especially susceptible to X-ray induced damage. Already after ~30 min, signs of degradation become visible in the spectra (not shown), and after 6 h of exposure, in the N 1s region, a clear 3rd peak emerges in between the two original peaks, while the peak at lower BE decreases. Also in the O 1s region, the peak associated with the anionic SO_3^- group increases in intensity. There are also prominent changes in the other spectra (not shown). In some cases, the IL even bubbles when exposed to X-rays, which is a clear sign of generation of highly volatile species. To circumvent this problem of X-ray damage for the CO_2 absorption experiments, a reduced X-ray power of

50 W has been used for the above experiments, which was demonstrated to be applicable to the IL for up to 15 h without any pronounced spectral changes.

Furthermore, apart from X-ray induced degradation of ILs, also for processes such as *in situ* reaction monitoring, recording of angle-resolved spectra in the usual consecutive way may be impossible if the reaction is too fast. For example, for the above described acid-base reaction (see also Figure 14 right), recording of a complete set of region spectra took 80 min, which is exactly the time lapse in between two steps recorded. Recording of 80° emission spectra in between the 0° spectra series is impossible timewise, and even if it was possible for reactions proceeding on a slower time scale, then 80° spectra would always be recorded in between the 0° emission data. This does not allow 0° to 80° comparison that is required for determination of orientation effects.

Thus, the huge advantage of recording spectra simultaneously is a reduction of measurement time by a factor of 2, which especially for susceptible samples decreases the amount of X-ray damage considerably, and the certainty that normal and grazing emission data always originate from the same point in time. In addition, the DASSA spectrometer yields a higher signal per incoming X-ray than the ESCA and GAP spectrometers, due to improved electron detection efficiency, which even further reduces spectra recording time.

7. Electronic structure

It was shown by our group that XPS can be used as an electron density probe to reveal the electronic structure of the ions that make up the IL. In particular, the correlation between XPS BEs and ^{1}H and ^{13}C NMR peak shifts was demonstrated.[43] Looking at Figure 6 in Section 3.4 on fitting procedures and comparing the C 1s spectra of $[C_8C_1Im][Tf_2N]$ and $[C_8C_1Im]Cl$, there clearly is a different chemical shift for the C_{hetero} component of these two ILs, revealing a difference in electron density in the identical $[C_8C_1Im]^+$ cation when combined with anions of different coordination behaviour. For functionalised ILs, XPS may be used to probe differences in electronic structure for all IL components as a function of factors such as headgroup type, functional group, number of functional groups, distance between headgroup and functional group (spacer length), functional group position and temperature.

As summarised in Section 7.1, it was demonstrated that functionalising an imidazolium headgroup with a thioether at different ring positions leads to significantly different electron density, especially on the S atom. Details are given in:

[P1] N. Taccardi, I. Niedermaier, F. Maier, H.-P. Steinrück, and P. Wasserscheid, *Cyclic Thiouronium Ionic Liquids: Physicochemical Properties and their Electronic Structure Probed by X-Ray Induced Photoelectron Spectroscopy*, Chem-Eur J 18, 27, 8288-8291, **2012**.

While the chemical shift in this case is quite large, making it detectable with the given resolution of the ESCA instrument, the improved resolution of DASSA enabled investigation of much more subtle effects, as shown in Sections 7.2-7.3 for different nitrogen based cationic headgroups and for temperature effects (not published yet).

7.1. Electronic structure of two thio-functionalised ILs[P1]

Figure 15 shows both thio-functionalised ILs whose electronic structure is compared in [P1]. In 3-(methylethylsulfide)-1-methylimidazolium bis(trifluoromethylsulfonyl)imide (7.1) the S atom is part of a thioether group in the side chain bound to the 3-position of imidazolium while in the structural isomer 3-ethyl-2-(methylthio)-1-methylimidazolium bis(trifluoro-methylsulfonyl)imide (7.2) the S atom is directly bonded to the 2 position of imidazolium, forming a thiouronium functional group. In XPS, both ILs give rise to two clearly separable S 2p doublets (Figure 15 right) with the anionic S $2p_{3/2}$ signal at an identical position for both ILs at 168.9 eV. This shift to high BE results from the neighbouring O atoms in the sulfonyl groups of $[Tf_2N]^-$ (see Table 1 for $[Tf_2N]^-$ structure).

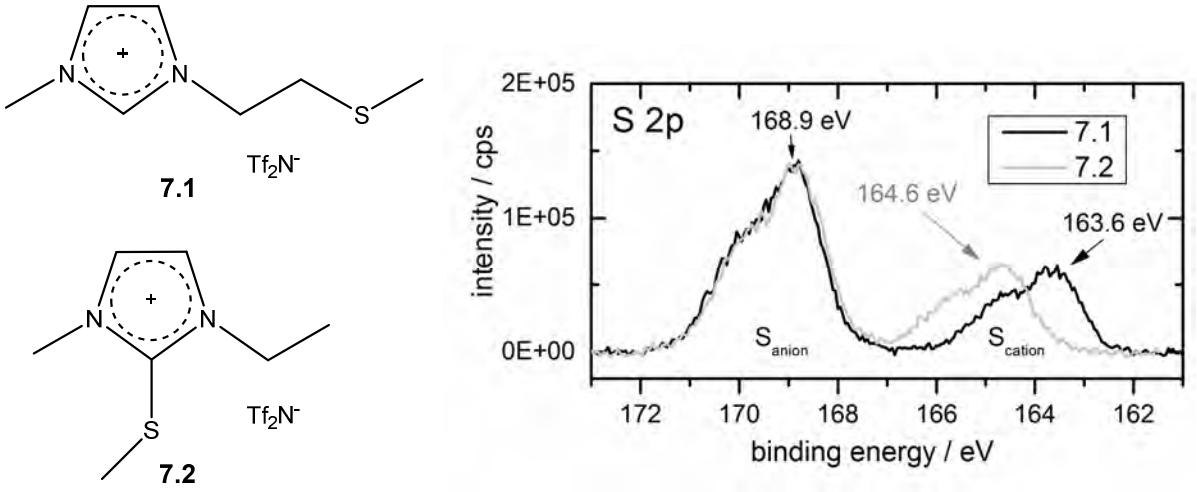

Figure 15 left: 3-(methylethylsulfide)-1-methylimidazolium bis(trifluoromethylsulfonyl)imide (**7.1**) and 3-ethyl-2-(methylthio)-1-methylimidazolium bis(trifluoromethylsulfonyl)imide (**7.2**); right: 0° emission spectra of the S 2p region of 7.1 (black) and 7.2 (grey). BE positions of the S $2p_{3/2}$ components are indicated for all species. Spectra were recorded with the ESCA setup.

More importantly, the S 2p signals of the cation of 7.2 exhibit a large shift of 1.0 eV towards higher BE relative to that of 7.1. Although S has identical next neighbours in both cations (C on both sides), the pronounced difference in BE clearly indicates that charge density at the location of S differs considerably, with lower electron density for compound 7.2. Apparently, there is an increased degree of charge transfer between imidazolium ring and thio group in the case of C2 attachment. The concomitant higher electron density on the imidazolium ring of 7.2 is confirmed by shifts in the $N_{imidazolium}$ and C_{hetero} signals to lower BE when compared to 7.1 or to a reference IL $[C_2C_1Im][Tf_2N]$. In addition, there is a pronounced shift of the C2 signal to higher BE in 7.2 when compared to $[C_2C_1Im][Tf_2N]$. This is due to the covalent bond to S with considerably higher electronegativity than H (see [P1] for C 1s and N 1s spectra).

7.2. Electronic structure of different cationic N species

Taking advantage of the improved energy resolution of DASSA, the N 1s BE of four different cationic N species in different ILs was compared to the N 1s BE of the standard imidazolium IL 1-ethyl-3-methylimidazolium bis(trifluoromethylsulfonyl)imide ($[C_2C_1Im][Tf_2N]$). The applied PE for these spectra is 20 eV, in contrast to the standard value for DASSA spectra of 35 eV, to further enhance resolution. The cations are pyrrolidinium (Pyrr), ammonium (A),

pyridinium (Py), and a cation based on the ethylated superbase diazabicycloundecen (DBU), a bicyclic molecule with two tertiary amine groups.

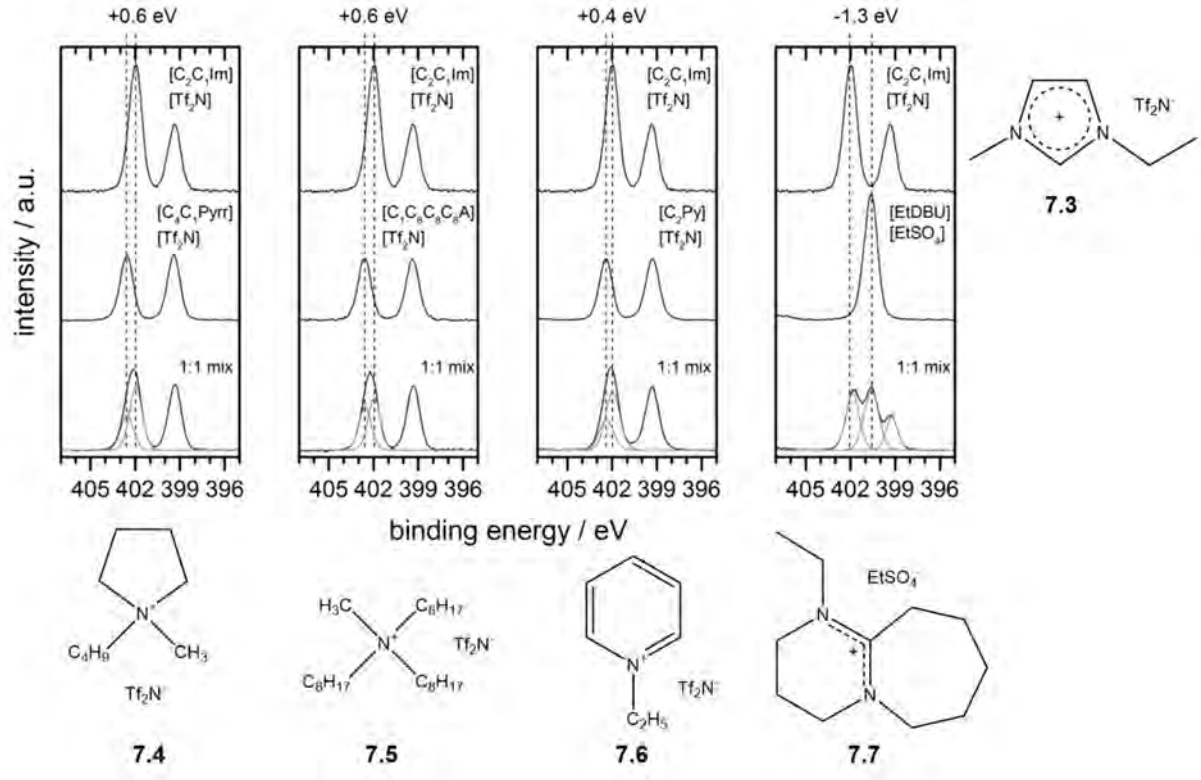

Figure 16: Normal emission N 1s spectra of the reference IL $[C_2C_1Im][Tf_2N]$ (**7.3**, four identical spectra at top, structure see far right), the ILs $[C_4C_1Pyrr][Tf_2N]$ (**7.4**), $[C_1C_8C_8C_8A][Tf_2N]$ (**7.5**), $[C_2Py][Tf_2N]$ (**7.6**) and $[EtDBU][EtSO_4]$ (**7.7**) (middle from left to right; structures are given below spectra) and a 1 : 1 (molar) mixture of each of these ILs with $[C_2C_1Im][Tf_2N]$ (bottom). Normalisation values are given in the main text. The values at the top give the difference of the N_{cation} peak to that of $[C_2C_1Im][Tf_2N]$. Spectra were recorded with the DASSA setup.

Figure 16 gives the structure of the reference compound $[C_2C_1Im][Tf_2N]$ (7.3, for the $[Tf_2N]^-$ structure see Table 1) as well as those of the investigated $[Tf_2N]^-$ based ILs with the cations *N*-butyl-*N*-methyl pyrrolidinium ($[C_4C_1Pyrr]^+$, 7.4), methyltrioctylammonium ($[C_1C_8C_8C_8A]^+$, 7.5, commonly also denoted $[OMA]^+$ in literature), *N*-ethylpyridinium ($[C_2Py]^+$, 7.6) and of the IL 1-aza-8-(ethylazolium)bicycloundecen ethylsulphate ($[EtDBU][EtSO_4]$ 7.7). While 7.4-7.6 are relatively common ILs, DBU is an untypical IL precursor. Ying et al. were the first to prepare a DBU-based IL by protonation with acetic acid, forming [DBUH][Ac].[53] There are a few subsequent publications that report on the use of this $[DBUH]^+$-based IL in catalysis.[54-57] Apart from that, Wu et al. reported on ILs based on alkylated DBU, among them also $[EtDBU][PhSO_3]$ ($[PhSO_3]^-$ = phenylsulfonate) with an identical cation as that in 7.7.[58] The IL 7.7 was received in 2012 from Lehrstuhl für Chemische Reaktionstechnik, Universität Erlangen-Nürnberg from the group of Dr. Peter S. Schulz, where it was synthesised by Matthias Bahlmann. It was intended for further CO_2 absorption experiments, but due to time restrictions, further studies

apart from a general characterisation were out of the scope of this thesis and had to be postponed.

The top spectrum of each of the four columns in Figure 16 gives the N 1s region of the reference $[C_2C_1Im][Tf_2N]$, the middle row shows the N 1s region of the four investigated neat compounds and the bottom row gives spectra of a molar 1 : 1 mixture of the respective IL with the reference IL $[C_2C_1Im][Tf_2N]$. To account for different densities and therefore different signal intensities, all spectra were normalised to the $[C_2C_1Im][Tf_2N]$ F 1s intensity (spectra not shown) which effectively equalises the intensity of all anion signals, in particular also the N_{anion} signal in the above spectra at 399.4 eV. Slight BE corrections in the order of 0.05-0.20 eV were also necessary for some spectra due to slight charging effects. The BE was also referenced to the F 1s (and thus, in effect, the N_{anion}) signal. For the $[EtDBU][EtSO_4]$ (7.7), spectra with its different anion compared to the other $[Tf_2N]^-$ ILs, intensity normalisation of all spectra was carried out assuming the N_{cation} signal in the pure compound has an identical intensity to the $N_{imidazolium}$ signal in 7.3, and that the $N_{imidazolium}$ signal in the 1 : 1 mixture is half the intensity of that in pure $[C_2C_1Im][Tf_2N]$. The BE scale of the mixture was referred to the $N_{imidazolium}$ signal of $[C_2C_1Im][Tf_2N]$, and the obtained BE of the N_{cation} signal of $[EtDBU][EtSO_4]$ in the mixture was then used as reference for the pure compound.

Looking at the cationic N 1s signals which is the high BE signal for the $[Tf_2N]^-$ based ILs, there is a clear difference in BE for all four ILs when compared to the $[C_2C_1Im][Tf_2N]$ $N_{imidazolium}$ signal at 402.0 eV. For 7.4 and 7.5 the signals are both shifted by 0.6 eV to higher BE. The shift is slightly lower for 7.6 and amounts to 0.4 eV. Only for 7.7 the N_{cation} signal is shifted to lower BE by a value of 1.3 eV.

As chemical shift in XPS is influenced by local electron density, the spectra show that electron density is considerably lower on the pyrrolidinium and the ammonium N atom (7.4 and 7.5) when compared to the imidazolium N atoms (7.3). In consequence, this demonstrates that the positive charge is located to a higher degree on the N atoms in the case of pyrrolidinium and ammonium. This finding is in agreement with expectations, as both the pyrrolidinium and the ammonium N atom are bonded solely to aliphatic or alicyclic alkyl groups, whereas for imidazolium, both N atoms are part of an aromatic system. For this, the positive charge is less strongly located, but dispersed over the extended π system, leading to a lower positive charge density / higher electron density on the N atoms. The pyrrolidinium group could also be viewed as a cyclic ammonium, which makes the fact that the cationic N 1s signal of both groups exhibits an identical shift understandable. In the pyridinium compound (7.6), however, the N atom is also part of an aromatic system with lesser charge localisation, as is the case for imidazolium. Still, electron density must be lower on pyridinium when compared to imidazolium as is witnessed by the shift to high BE. This is due to the positive charge being dispersed over

two N atoms in the case of imidazolium, while it resides on one N atom only in the case of pyridinium.

There is only one N 1s signal for compound 7.7, as the charge is evenly distributed by resonance across the $[N=C-N]^+$ moiety. Positive charge density is very low / electron density is comparatively high on this moiety, as the signal exhibits a pronounced shift to lower BE when compared to the $N_{imidazolium}$ signal. As there is no extended π system on this bicyclic structure, a situation intermediate between that of ammonium/pyrrolidinium and imidazolium could be expected, due to the presence of two N atoms, but no aromaticity. As for this IL only, the anion is not $[Tf_2N]^-$, likely an electron inducing effect of the $[EtSO_4]^-$ anion is at least partly responsible for the observed shift to low BE. The above-mentioned early publication of our group[12] investigates BE as a function of charge density, that is varied by combining different anions to an identical cation. Cationic N 1s BEs of ILs with small, well coordinating anions such as halides differ by up to -0.6 eV from that of $[Tf_2N]^-$ based ILs. Unfortunately, $[EtSO_4]^-$ was not part of this investigation, but for $[C_2C_1Im][EtSO_4]$ in Ref. 29, we find a cation N 1s BE of 401.5 eV (relative to O 1s and S 2p of compound 7.7). This is by 0.5 eV lower than the $[C_2C_1Im][Tf_2N]$ N 1s BE of 402.0 eV, showing that $[EtSO_4]^-$ has an electron inducing effect in the order of the halides. The residual shift to low BE observed for $[EtDBU][EtSO_4]$ must thus result from the structure of the cation. As there is no extended π system, the positive charge must mainly be located on the C atom of the $[N=C-N]^+$ moiety. This assumption is confirmed by the pronounced shift of the respective C 1s signal to higher BE by 0.6 eV more than for the C2 atom in imidazolium ILs, as shown in Figure 17.

For pyrrolidinium (7.4), the observed BE is in agreement with that reported by Shigeyasu et al.[59] and by Men et al.[60] for the identical IL (N_{cation} = 402.6 eV relative to N_{anion} = 399.4 eV in Figure 16, N_{cation} = 402.5 eV relative to N_{anion} = 399.3 eV in Reference 59, N_{cation} = 402.7 eV relative to N_{anion} = 399.5 eV in Reference 60). The same is true for the ammonium IL (7.5) when compared to XPS BEs reported on similar alkylammonium ILs by the Licence group[61] (N_{cation} = 402.6 eV relative to N_{anion} = 399.4 eV in Figure 16, N_{cation} = 402.5 eV relative to N_{anion} = 399.3 eV in Reference 61). The pyridinium IL 7.6 was also investigated by the Licence group[62] who reported slightly diverging peak positions (N_{cation} = 402.4 eV relative to N_{anion} = 399.4 eV in Figure 16, N_{cation} = 402.6 eV relative to N_{anion} = 399.5 eV in Reference 62). No XPS data is reported on the IL $[EtDBU][EtSO_4]$ or the $[DBUH]^+$ analogues.

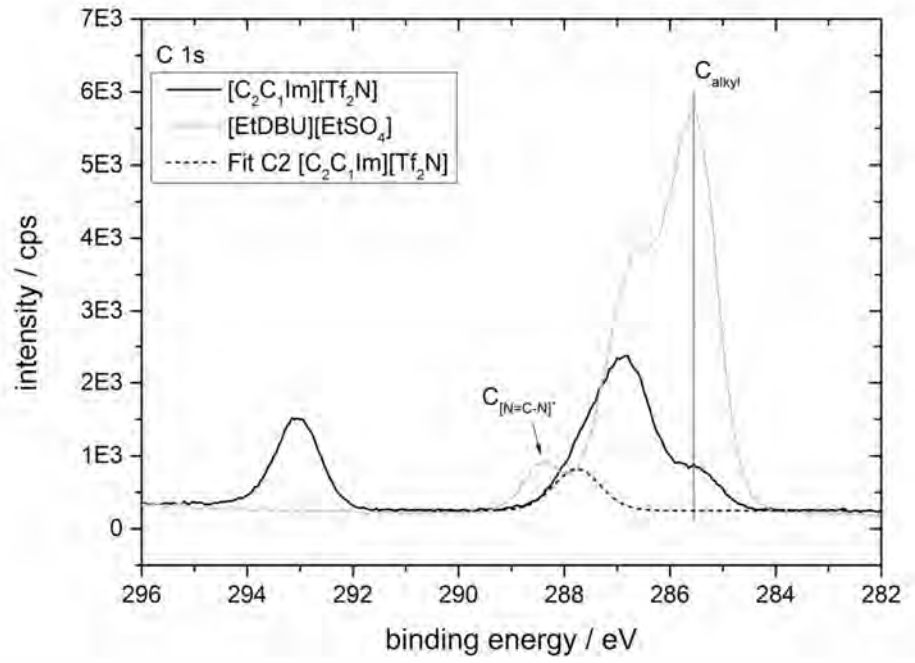

Figure 17: C 1s region of $[C_2C_1Im][Tf_2N]$ (black) and $[EtDBU][EtSO_4]$ (grey) and the $[C_2C_1Im][Tf_2N]$ C2 fit peak (black dashed). The related $[N=C-N]^+$ peak of $[EtDBU][EtSO_4]$ that is also bonded to two N atoms is considerably shifted to higher BE when compared to the $[C_2C_1Im][Tf_2N]$ C2 signal. Spectra were recorded with the DASSA setup.

Taking all spectra into account (F 1s, O 1s, C 1s and S 2p not shown), the calculated atom numbers agree well with the nominal values. Having thus ascertained the absence of impurities, a molar 1 : 1 mixture of each of the four ILs with $[C_2C_1Im][Tf_2N]$ was prepared using ACN as a solvent to ensure proper mixing. ACN is completely removed from the mixture by evaporation in UHV prior to XPS measurements. For the N 1s spectra of the mixtures in Figure 16, the N_{cation} to N_{anion} distance obtained from the pure compounds were used as constraints for the fits shown in grey as well as an identical fwhm for the N_{cation} peak of the investigated IL and the $N_{imidazolium}$ peak of $[C_2C_1Im][Tf_2N]$. For all mixtures but $[C_1C_8C_8C_8A]/[C_2C_1Im][Tf_2N]$, the calculated atom numbers and nominal atom numbers coincide very well, indicating the applicability of the fit model and homogeneous mixing of both components. In particular, the nominal N_{cation} : N_{anion} ratio of 3 : 2 for equimolar mixtures of 7.3 with 7.4 and 7.6 are found in the 0° emission spectra. For $[C_1C_8C_8C_8A]/[C_2C_1Im][Tf_2N]$ there is a predominance of the ammonium N_{cation} signal over $N_{imidazolium}$. The nominal ratio would be 1 : 2 ($N_{cation,\ ammonium}$: $N_{imidazolium}$), but the observed ratio is 1.0 : 1.2 only. There is further a predominance of 5-10 % of all cationic C 1s signals over the nominal values, and concomitantly by 5-10 % lower than nominal atom numbers for all anion signals (spectra not shown). This shows that most likely, there is a predominance of the ammonium cation $[C_1C_8C_8C_8A]^+$ over the imidazolium cation $[C_2C_1Im]^+$ in the surface near region of the IL to such an extent that this is already noticeable in the 0° spectra. The fact that the same trend is more pronounced in the 80° data corroborates this assumption. As the results were obtained by a single measurement

and were not repeated with a second sample to confirm reproducibility, it is, however, also possible that an error during preparation of the mixture led to an IL ratio different from 1 : 1. As both ILs have a common anion and their cationic C 1s signals are not separable, such an error would only be observable in the N 1s region.

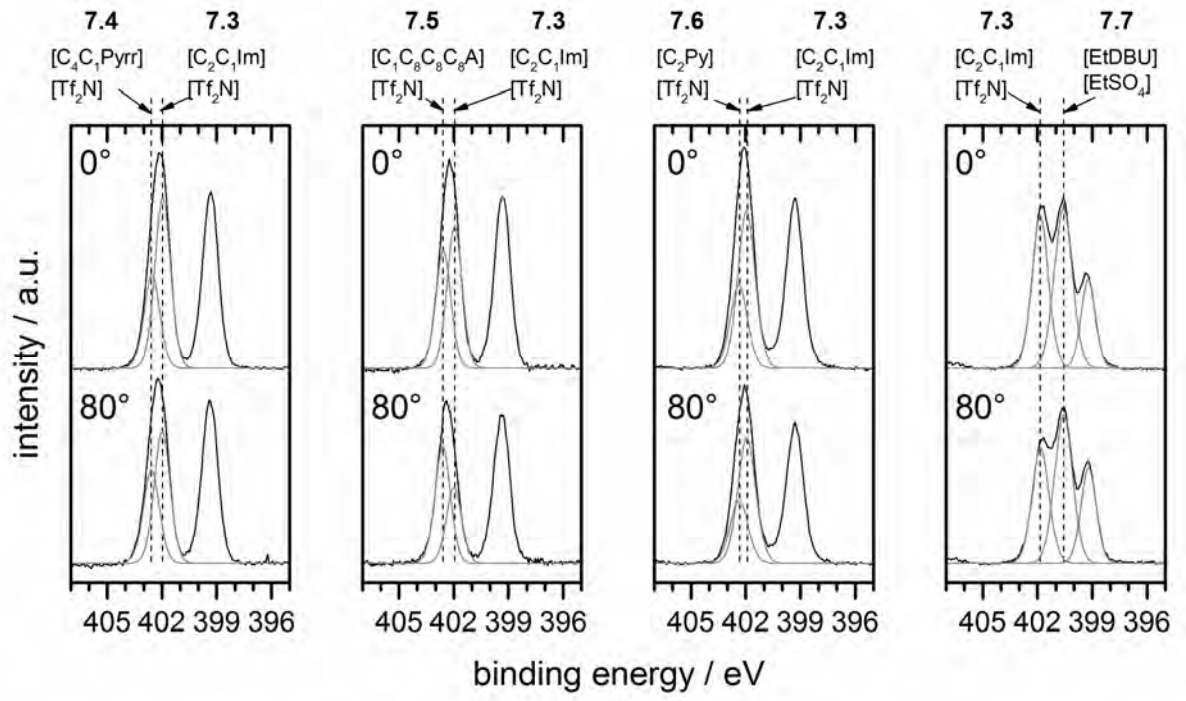

Figure 18: Comparison of the N 1s 0° and 80° emission spectra of the mixtures introduced in Figure 16. Spectra were recorded with the DASSA setup.

In Figure 18 the N 1s 0° emission spectra of the four different mixtures are reproduced. In addition, the more surface sensitive 80° data and the fit peaks are shown. The cationic N 1s species are assigned at the top. For the 80° fits identical constraints as those described for the 0° data were used, and all spectra were scaled by the GF as described in Section 2.3 and [P5]. For the $[C_1C_8C_8C_8A]/[C_2C_1Im][Tf_2N]$ mixture (second from left), there is a strong increase of the ammonium component in 80° when compared to 0°, resulting in a 1.0 : 0.7 ratio ($N_{cation,\ ammonium}$: $N_{imidazolium}$). The C_{alkyl} component that nearly exclusively arises from the ammonium cation also shows enhancement in the 80° spectra by 25 % (not shown). Thus, there must be a clear enrichment of the $[C_1C_8C_8C_8A]^+$ cation at the expense of the $[C_2C_1Im]^+$ cation at the surface. A similar, though not as pronounced behaviour is found for the pyrrolidinium compound 7.4. While the atomic ratios in the 0° data agree with nominal stoichiometry, there is a 5 % increase in $N_{cation,\ pyrrolidinium}$ intensity in 80° when compared to 0° emission and a 20 % decrease of the $N_{imidazolium}$ signal. This gives a 1.1 : 1.4 ratio ($N_{cation,\ pyrrolidinium}$: $N_{imidazolium}$), while the nominal ratio would be 1 : 2. There is also an intermediate (7 %) intensity increase in 80° relative to 0° of the C_{alkyl} signal mainly associated with the pyrrolidinium cation, so overall, at the surface of the

mixture, the $[C_4C_1Pyrr]^+$ cation is enriched while $[C_2C_1Im]^+$ is depleted. For the mixture of $[C_2C_1Im][Tf_2N]$ with the pyridinium compound 7.6, the 80° data show no pronounced surface enrichment effects apart from the typical $[Tf_2N]^-$ orientation discussed in Section 4.1 and [P4], so that both cations are present in the nominal 1 : 1 ratio at the surface. A slight surface segregation effect was found for the $[C_2C_1Im][Tf_2N]$/[EtDBU][$EtSO_4$] mixture: both cationic N 1s signals that have a nominal 1 : 1 ratio decrease in intensity in the 80° spectrum, but the $N_{imidazolium}$ does so to a higher extent, resulting in a 1.0 : 0.7 ratio ($N_{cation,\ EtDBU}$: $N_{imidazolium}$). So again, the imidazolium cation must be depleted from the surface to the benefit of [EtDBU].

The enrichment of the pyrrolidinium (7.4) and ammonium (7.5) cation over the imidazolium based $[C_2C_1Im]^+$ is contrary to what one could expect from the chemical shift data, as both cationic N atoms in compounds 7.4 and 7.5 have a higher degree of charge density than those in $[C_2C_1Im]^+$. From the results of [P4] and Section 4.1, one would assume that IL moieties with a higher charge density should be located at a larger distance from the surface than those having a lower charge density or are uncharged. To unequivocally determine surface enrichment of different headgroups, however, similar or identical alkylation of these would be necessary to exclude an effect of different alkyl chain lengths. In the present case, surface enrichment scales with the C_{alkyl} content of the cation and is thus most pronounced for the ammonium with three octyl groups attached. Because in all surface sensitive studies that I am aware of, C_{alkyl} enrichment is observed for long aliphatic chains, it is a feasible assumption that cation surface enrichment observed here, and in particular the very pronounced enrichment of the ammonium cation, are indeed induced by the surface-enriched alkyl chains “pulling” the associated headgroup towards the surface.

For the [EtDBU][$EtSO_4$] mixed with $[C_2C_1Im][Tf_2N]$, the reason for the observed enrichment of $[EtDBU]^+$ is likely not related to the high electron density induction by the $[EtSO_4]^-$ anion and the resulting lower charge density on the cation, as one could spontaneously assume. As in an IL mixture anions and cations are expected to mix equally, resulting in a mixture structure that is just as well described as containing [EtDBU][Tf_2N] and $[C_2C_1Im][EtSO_4]$, the electron induction of $[EtSO_4]^-$ is not expected to exclusively affect the $[EtDBU]^+$ cation. The surface enrichment could probably be related to the predominance of nonpolar cyclic alkyls in $[EtDBU]^+$. For unambiguous determination of cationic surface enrichment, however, it would be advantageous to use identical anions for both components to exclude any anion-induced effect.

7.3. BE shift as a function of temperature for [$C_{18}C_1$Im][TfO]

Several studies have by now been carried out at DASSA, where IL peak positions were monitored as a function of sample temperature. One of these investigations is described in detail in [P5]. In addition, the data of a related analysis is presented below. These investigations are motivated by the prevailing lack of knowledge on how charge compensation in XPS and hence charge transport in ILs operates.

Charge transport in ILs can be considered along the lines of classical electrolytes that are composed of a non-conducting solvent and a charge-carrying solute that is typically a salt. Ionic conduction in electrolytes with low solute concentration is mainly dependent on diffusion of the charge carriers that on average do not interact with each other. The charge transport process in ILs is similar to that in electrolyte solutions in that the charge carriers are ions. However, the pronounced difference is the absence of neutral solvent molecules that screen interionic interactions. For ILs, the ionic conduction mechanism is thus thought to be influenced by further factors such as ion size or cation-anion interactions.[63-65]

In XPS, electrons are emitted from the sample surface by photoemission, leading to a formal oxidation of the surface. These electrons have to be replenished to counteract build-up of a positive surface charge that affects the kinetic energy of the photoelectrons and hence leads to an apparent signal shift to higher BEs. For non-conducting samples, electrons of low energy have to be supplied by a flood gun directly to the sample surface, but ILs are sufficiently conductive to allow electron replenishment from the grounded sample support. Conduction through ILs is basically an ionic process, as noted above. However, during XPS of ILs, a shift of all signals to higher BEs is commonly observed with increasing X-ray exposure time, showing that conduction through the liquid is likely insufficient for complete charge compensation (see Reference 66 for a more elaborate discussion). The investigations of BE changes as a function of temperature for different ILs can shed light on to what extent increased ion mobility can enhance conductivity to counteract surface charging. The spectra were recorded with DASSA due to its superior energy resolution.

In the study described here, XP spectra of the IL [$C_{18}C_1$Im][TfO] ([TfO] = trifluoromethyl-sulfonate or triflate, [F_3C-SO_3]$^-$) were recorded at different temperatures. Prior to the investigations, the IL was degassed *in vacuo* by heating it to 423 K over a period of 4 h. Simultaneously recorded QMS spectra and a strong increase in chamber pressure confirmed the loss of water from the IL during this heat-up phase. Subsequently, starting from 423 K the IL was allowed to cool down and spectra were recorded at 30 K intervals down to 303 K. After this, the IL was again heated up to 423 K while spectra were recorded, followed by a cooling phase identical to the first one.

Notably, the IL [$C_{18}C_1$Im][TfO] contained a polysiloxane impurity. Though only minor, the presence of this impurity may have influenced the results given below to some extent. The topic of polysiloxane contamination is discussed in Chapters 4 and A.1 (Appendix) of this thesis, and will be revisited in Chapter 8.

[$C_{18}C_1$Im][TfO] is a liquid crystalline IL with the transition from smectic A phase to solid at ~328 K, with a ~20 K hysteresis in the heating phase. In pre-trials of the below described experiment, it was shown that for sample layer thicknesses in the order of 100-400 µm, sample charging was considerable for the solid IL at 303 K, giving rise to strong shifts to high BE of all peaks, and in some cases also partial charging noticeable in double peak structures. It is the experience of our group that charging of solid samples can be diminished to a large extent by preparing very thin sample layers on the support. Therefore, for the below described experiments, a thin sample film of 12 µm thickness was prepared by the solution method described in 3.6 using ACN.

To judge the changes in BE relative to sample temperature, averaged values of BE differences to the BE position at a reference point for all species were calculated from the fitted spectra. The BE positions at 423 K at the start of the measurements were chosen as reference values due to the fact that a) water was removed, b) highest intrinsic conductivity was expected due to high ion mobility, and c) potential radiation damage was minimal. In Figure 19, the BE shifts are depicted *vs.* X-ray duration (i.e. measurement time) and also relative to sample temperature, to also visualise effects that may arise from increased X-ray or UHV exposure. The reference point where the BE shifts of all signals equal zero is depicted by a star symbol. Note that for all three measurements at 303 K (highlighted in grey), where the bulk IL is solid, the mean BE values are considerably higher compared to the respective values at the next data point at 333 K, and the very last 303 K value is on average highest. This shows that in spite of the use of the very thin film, charging of the solid sample still occurs, leading to a shift of all signals to high BEs.

Disregarding the 303 K data points with high charging of the solid sample, there seems to be an overall decreasing trend for average BE with X-ray duration, marked by the dashed grey line in Figure 19. This is unusual and in contrast to the above mentioned overall BE increase of all signals commonly observed for ILs with increasing X-ray exposure time. Apart from that, the data points in the complete heating and cooling cycle (in between the 2nd and 3rd 303 K points) at least suggest a weak relationship to temperature: as temperature increases, BE slightly decreases. This could be a manifestation of the expected effect described above: with increasing temperature, ion mobility and thus conductivity increases, leading to enhanced charge transport and thus better compensation of photoelectron loss, and in effect to a lower BE. However, the BE increase with decreasing temperature is weak, and is not seen in the

first cooling phase. To improve reliability of data, several more heat/cool cycles would have to be carried out.

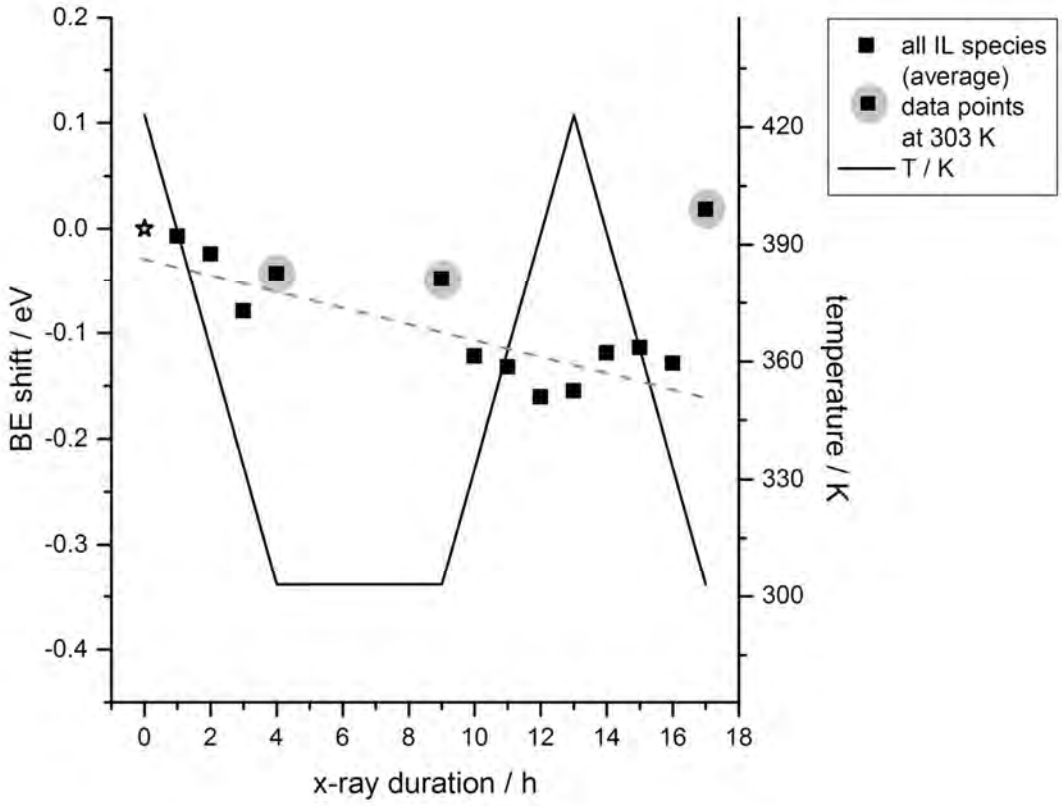

Figure 19: Average change of BE with temperature in a cooling/heating/cooling cycle of [C18C1Im][TfO]. The BE position of the first 423 K measurement is chosen as reference point (BE shift = 0 eV, marked with a star symbol). At 303 K (data points highlighted in grey), the IL is solid, leading to a determined shift to higher BE.

To obtain further information on BE shift of each species with temperature and/or measurement time, in Figure 20 the previous figure is expanded to show the BE shifts of each contribution separately. To elucidate an emerging trend, all anion signals are shown in black and all cation signals are shown in grey. The data points at 303 K, where the trend is disturbed by sample charging, are marked by rectangles. There is a clear temperature dependence of BE position for the signals of both ions: for anion species, the BEs increase with decreasing temperature, and vice versa, for cations, the BEs decrease with decreasing temperature. In a simplified initial state picture, anions become more negatively charged (increase in electron density) with increasing temperature, which reduces the observed BE, whereas at the same time cations become more positively charged (decrease in electron density). This effect could be related to the IL density: as temperature increases, density for most compounds decreases, which is equivalent to an increase of interionic distances. As described in Reference 43, interionic charge transfer is related to coordination of the ions that constitute the IL, or in other words, on how and at which distance the ions arrange. Thus transfer of electron density from

anion to cation is lowered when the ions are further apart, resulting in the observed higher anionic and lower cationic electron density with increasing temperature.

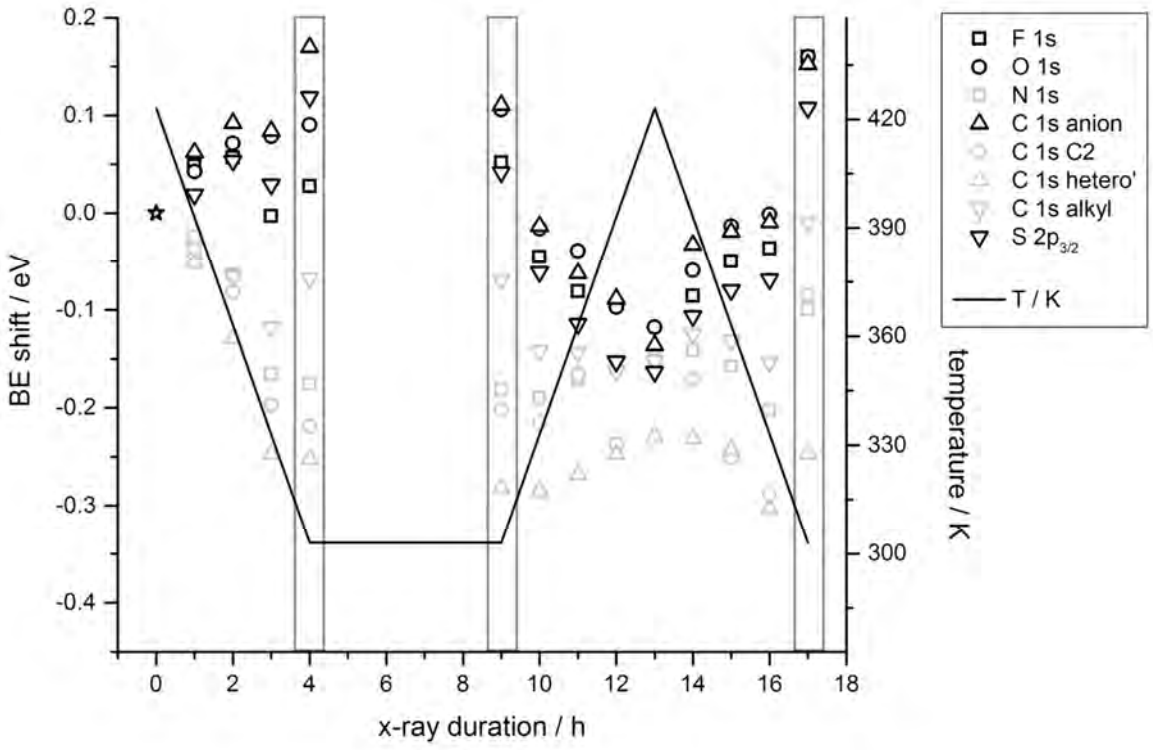

Figure 20: Change of BE with temperature in a cooling/heating/cooling cycle of [$C_{18}C_1$Im][TfO] for each species. Black data points refer to anion species and grey data points refer to cation species. The BE position of the first 423 K measurement is again chosen as reference point (BE shift = 0 eV, marked with a star symbol). The 303 K data points where the IL is solid are marked with grey rectangles.

As a final note in this section, a similar behaviour was observed when investigating the IL [(BrC_2)C_1Im][Tf_2N] at temperatures between 223 and 373 K with the ESCA setup. In Figure 21, BE positions at 373 K were chosen as the point of reference that is again marked with a star symbol. There are the same temperature dependencies of the BE shifts for cation and anion signals than for [$C_{18}C_1$Im][TfO]. However, the trends in this case are superimposed by the overall peak shift to higher BE with increasing X-ray exposure time (black solid squares). This is a typically observed behaviour for many ILs that results from charge build-up at the IL surface. Hence, the decrease of BE with increasing temperature for all anion signals is nearly reversed (black open symbols), while the trend of increasing BE with increasing temperature of all cation signals is enhanced (grey symbols).

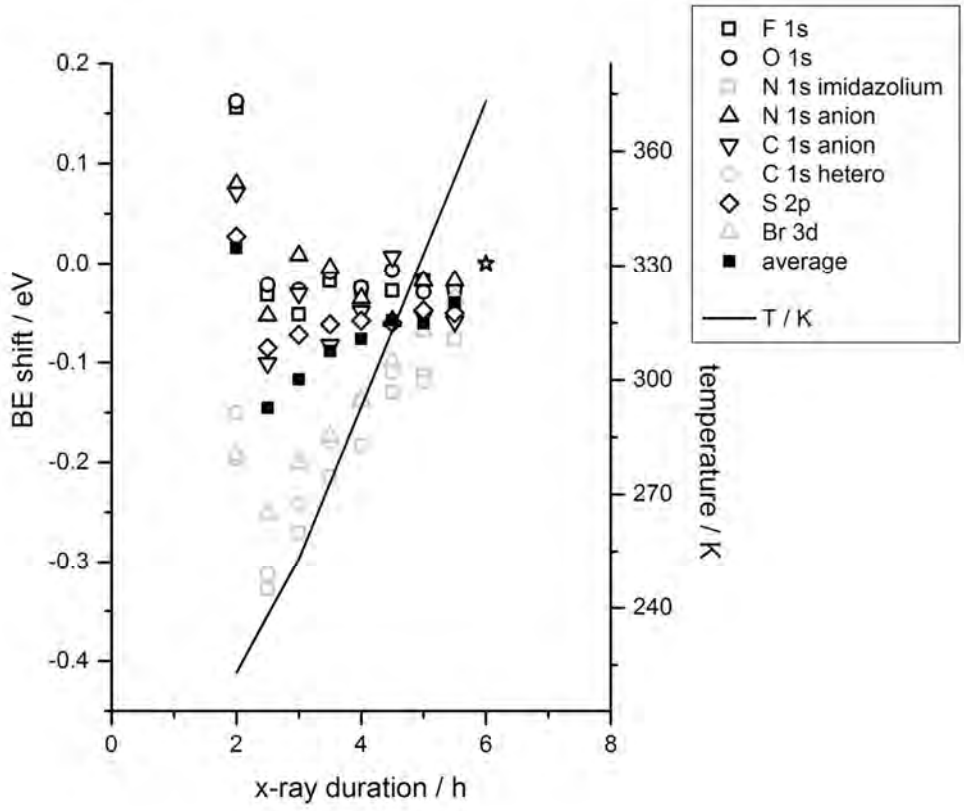

Figure 21: Changes in BE with increasing temperature for all species in the IL [(BrC_2)C_1Im][Tf_2N] for anion (black, open symbols) and cation (grey) peaks relative to the peak position at 373 K (BE shift = 0 eV, marked with a star symbol). The black solid squares show the average peak shift for all species.

8. Outlook

This thesis summarises my contributions to IL surface science by ARXPS. As this field has been developed into multiple directions, the previous chapters already covered a wide spectrum of investigations. Naturally, future research will be even more diverse, and highly developed instrumentation and sophisticated procedures will allow for a wealth of prospective research fields.

Functionalisation of ILs is, as mentioned, nearly unlimited in its potential. Many of the new materials that will be developed for different applications will rely on surface processes, and thus will require thorough surface characterisation for a fundamental understanding and the improvement of their performance. The fact that XPS can be used as a probe sensitive to charge distribution makes it complementary to NMR when it comes to determination of reactivity of differently functionalised moieties. For reaction monitoring, the concept of functionalised ILs can be employed in many diverse fields, and the possibility of sample temperature manipulation and controlled addition of reaction partners allows for investigation of a wide range of reactions.

Instead of a lengthy listing of possible ways in which ARXPS on ILs can be employed, this Outlook chapter will focus on one specific research direction, where several pre-investigations have already been done in the course of this thesis. The project deals with the potential use of siloxane-based ligands as "float balls" for catalytically active complexes in ILs.

It has been noted several times throughout this thesis that silicone-based impurities in ILs that are likely polysiloxane (PSi) compounds show an extremely high surface activity, so that minute traces in ILs can complicate surface investigations of the IL, although the impurity is not even detected by other characterisation techniques such as NMR (see e.g. Chapter 4).

On the one hand, this is an annoying complication and leads to time-consuming surface cleaning procedures that impede reliability of results. On the other hand, this extreme surface enrichment carries a huge potential: if a defined siloxane compound was tethered to a catalyst dissolved within an IL, it may be possible to enhance the surface activity of the catalyst considerably. For homogeneously catalysed reactions in a SILP system[17], bringing the catalyst as close as possible towards the IL/gas interface can decisively diminish diffusion limitation of the reaction rate.

Prior to embarking on detailed research on such a surface enhanced SILP catalyst, questions that need to be answered include:

1) Is the impurity containing Si, C and O that is encountered in ILs indeed a PSi?

2) If so, is the extreme surface activity inherent for PSi? Or are PSis identifiable in minute traces only due to the fact that their Si atoms make them detectable in ILs that typically contain no Si, whereas e.g. the C 1s signals of hydrocarbon polymers that may have a similar potential of surface enrichment will nearly always be superimposed by IL signals?

3) Is the surface activity related to the fact that PSis are long chain polymers, or will PSi monomers or oligomers, when used as ligands, show the same behaviour?

4) Does the surface enrichment depend on factors such as temperature or surface composition of the IL?

5) How strong is the enrichment for different PSis, i.e. at which bulk concentration are they still detectable at the surface by XPS?

Some of these questions have already been addressed by obtaining several commercial PSis and dissolving trace amounts of them in ILs. It was found that these commercial compounds showed the same high surface enrichment as typical impurities.

In the following, results on the vinyl-terminated compound poly(dimethylsiloxane) (see structure in Figure 22) dissolved in the ILs $[C_2C_1Im][Tf_2N]$ and $[C_8C_1Im][Tf_2N]$ are presented. To obtain a sufficient dilution and to enhance mixing between IL and PSi, a solvent has to be used. Several solvents and solvent mixtures have been investigated for their potential to dissolve different PSis and ILs. For the presented data, a 1 : 1 : 1 (vol) mixture of isopropanol, acetonitrile and petroleum ether has been used. All three solvents were shown to contain no Si. In later test experiments not shown here, it has, however, been found that a 1 : 1 (vol) mixture of hexane and acetone is the solvent mixture of choice for further investigations. This avoids the presence of petroleum ether, which itself is a badly characterised alkane mixture with low purity.

In Figure 22, the 80° survey spectra of the ILs $[C_2C_1Im][Tf_2N]$ (left) and $[C_8C_1Im][Tf_2N]$ (right) after dissolving a tiny amount of the PSi in them are given. The bulk concentration of PSi in both ILs was calculated to be $1x10^{-4}$ mol%. Note that concentration values in this chapter are expressed as PSi monomer per IL ion pair to retain comparability to differently terminated poly(dimethylsiloxane) compounds. These will also be investigated in the future and differ in

monomer number n and hence molecular mass M. In the initial RT spectra (top), no Si 2s/2p peaks are visible for $[C_2C_1Im][Tf_2N]$, whereas small Si 2s/2p signals can be found in the $[C_8C_1Im][Tf_2N]$ spectrum at ~152 eV and ~100 eV. The PSi surface content can be estimated from the spectra by comparing e.g. the S 2p and Si 2p intensities. Their ratio is roughly estimated to be 10 : 1 (S 2p : Si 2p), and this translates into a 40 mol% surface concentration of PSi (ASF(S 2p) ≈ 2 x ASF(Si 2p); 2 S atoms per IL ion pair and 1 Si atom per PSi monomer). The PSi is thus enriched by 5 orders of magnitude in the uppermost 1.0-1.5 nm when compared to the bulk.

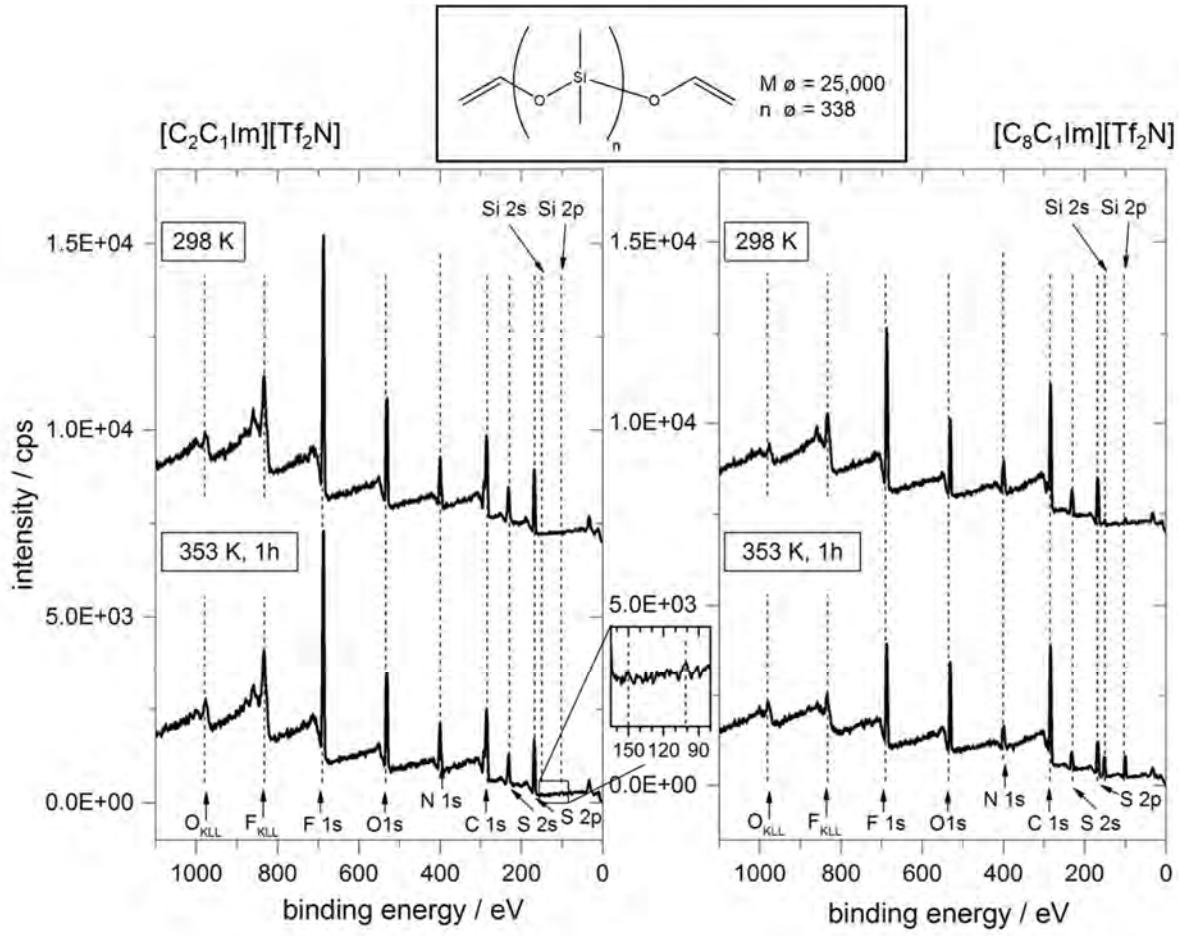

Figure 22: 80° emission survey spectra of $[C_2C_1Im][Tf_2N]$ (left) and $[C_8C_1Im][Tf_2N]$ (right) containing the vinyl terminated PSi compound shown at the top at a bulk concentration of $1x10^{-4}$ mol% (PSi monomer/IL pair). Spectra are given at RT (top) and after heating the IL to 353 K for 1 h (bottom).

The PSi surface content even increases when the IL is heated (see bottom spectra at Figure 22). For $[C_8C_1Im][Tf_2N]$, the Si 2s/2p signals increase upon heating to 353 K for 1 h to ~5 times their initial intensity. Even for $[C_2C_1Im][Tf_2N]$ where Si 2s/2p signals could not be

discerned in the initial spectrum, after heating, low intense Si 2s/2p signals can be detected (see inset in the Figure). This effect is in line with a long experience of our group on PSi impurity behaviour and likely results from enhanced diffusion at elevated temperatures. It is usually not reversible for impurities or for the PSis investigated on purpose, i.e. once PSis were able to diffuse to the IL surface, they remain there even when the temperature again decreases. To my knowledge, the only exception to this behaviour is exhibited by $[C_{18}C_1Im][TfO]$ described in Section 7.3.

The fact that for the IL with the short alkyl chain ($[C_2C_1Im][Tf_2N]$) PSi enrichment is less pronounced than for the IL with the longer alkyl chain ($[C_8C_1Im][Tf_2N]$) is also perfectly in line with our long experience on PSi contaminations. Notably, more than five very elaborate attempts to synthesise the IL $[C_{18}C_1Im][TfO]$ (see Section 7.3) with a very long alkyl chain without any impurity failed, even though every possible precaution to prevent contamination was taken by highly experienced chemists in the synthesis.[67] Shorter chain ILs could be synthesised without any observed impurities by the same chemists acting along the same precaution guidelines. Apart from that, investigating our stock of standard ILs that contains $[C_nC_1Im][Tf_2N]$ with n = 2, 4, 6, 8, 10, 12, 14 and 16 confirmed the assumption that PSi impurities enrich more strongly at the surface of ILs containing long terminal alkyl chains, as for ILs with n > 10 small Si 2s/2p peaks were observed in XPS at 80° (data not shown). The ferrocenyl ILs reported on in the Appendix Chapter A.1 are a further case in point: the amide-linked compounds containing long terminal alkyl chains with n ≥ 7 all contained Si impurities prior to sputter cleaning, whereas the ether linked compounds without terminal alkyl chains did not.

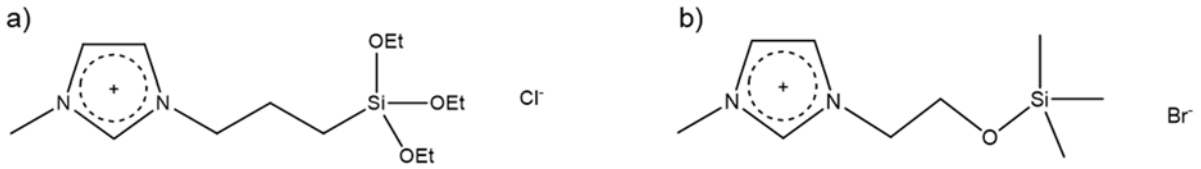

Figure 23: Two imidazolium ILs functionalised with a siloxane related moiety. In both cases, the functionalised side chain showed a high preference to orientate towards the vacuum.

Investigations on silicone-functionalised ILs can shed some light on question 3 above on whether or not the high surface activity will remain when PSis are no longer polymeric, but present as shorter oligomers or even monomers. The IL (tri(ethoxy)silylpropyl)methyl-imidazolium chloride (see Figure 23a) has already been introduced above as structure 4.3 and the clear orientation of the ethoxysilyl side chain towards the surface has been discussed in Section 4.1. The related IL (trimethylsilyloxyethyl)methylimidazolium bromide[68] that is given in Figure 23b also exhibits clear surface enrichment of the siloxane-functionalised side chain

(spectra not shown). These results suggest the possibility that the high surface activity of PSis is not only due to their polymeric structure, but also an inherent property of the siloxane motif.

Having so far ascertained the extremely high surface activity of PSis in general, further fundamental research must include the use of different PSis with varying terminal groups and different numbers of monomer repeat units in IL mixtures of low PSi concentrations. Differently functionalised ILs have to be investigated for their potential to enrich PSi at their surfaces, varying conditions such as temperature and concentration for a fundamental understanding of factors that promote PSi surface enrichment. In the next step, the project can progress to the synthesis of catalytically active complexes with PSi ligands, and the assessment of their performance under XPS conditions and more realistic large scale applications.

9. Conclusion

In the year 2006, surface science research on ionic liquid (ILs) was initiated in the work group of Florian Maier at the Department of Chemistry at the Universität Erlangen-Nürnberg (Physikalische Chemie II, Prof. Hans-Peter Steinrück).[4,29] Angle-resolved X-ray photoelectron spectroscopy (ARXPS) was subsequently carried out on a considerable number of different ILs. Numerous fundamental insights into surface composition and surface segregation effects in ILs and mixtures, solutions and dispersions based on ILs were achieved in the following years.[6,11-15,69,70] Based on these early findings, the work in this thesis presents the author's contribution to IL surface science from 2011 on. Incorporating five publications and complementary unpublished data, it expands the field from standard ILs to diversely functionalised ILs, and further examples of chemical reactions in ILs.

The surface composition of functionalised ILs is ruled by the interplay of different intermolecular forces that prevail between the different moieties of the IL, namely ionic interactions between the headgroups, dipole-ion or dispersive interactions between headgroups and non-ionic side chains and dipole-dipole or dispersive interactions between the side chains. Whether or not the IL shows some degree of surface order depends on the predominance of one of these interactions over the others. Observed surface compositions range from pronounced surface enrichment of e.g. halogenated alkyl chains, to isotropic arrangement of e.g. ether functionalised side groups.[P4]

Functionality introduces reactivity into ILs, and hence the possibility to study IL reactions by XPS. The reaction between the chloride anion of the IL $[C_8C_1Im]Cl$ acting as a weak base and the strong acid TfOH was thus investigated by XPS, monitoring the resulting anion metathesis that goes hand in hand with a molar density change. Changes in the XP spectra during acid dosage and temperature variations reveal that the reaction proceeds close to completion, but is restricted to the surface near region of the IL only.[P2] Investigation of a second reaction between an amine-functionalised IL and gaseous CO_2 led to fundamental insights for CO_2 uptake by amines, particularly for IL systems. It was shown that the uptake capacity of the near surface region for reaction products formed by CO_2 and amine is considerably higher than that of the bulk. Moreover, the dominant product species in the bulk differs from the dominant surface species that contains twice the amount of CO_2 for stoichiometric reasons. For the chemical absorption process taking place in high surface-to-volume media, both effects are highly advantageous for CO_2 capture.[P3]

Using chemical shifts of XPS signals as an indication of electron density of different IL moieties, two ILs functionalised with a thioether group at different positions of the imidazolium headgroup

were compared. For sulphur directly bonded to the C2 atom of imidazolium, there is a pronounced shift of the respective S 2p doublet to higher binding energy (BE) when compared to the S 2p signal of a thioether group part of the side chain at the 3-position of imidazolium. Hence, electron density of S at the 2-position is lower due to a higher degree of electron induction into the positively charged imidazolium ring when compared to S within the chain at the 3-position.[P1] However, variations in chemical shift in similar IL structures are frequently more subtle than those exhibited in the thioether results and require higher energy resolution to be detectable. The reported studies on such less pronounced variations include the investigation of ILs with different N-based cation headgroups, and of temperature effects in the IL $[C_{18}C_1Im][TfO]$.

The second main topic of this thesis is improvement of instrumentation for IL surface science research. The majority of the Erlangen results published so far has been achieved using a standard ARXPS setup that allows sample rotation to detect electrons under different polar emission angles. However, this method reaches its limits if low viscous liquids and/or films thicker than ~100 µm are to be investigated. A new XPS setup developed by our work group and obtained in 2014 is dedicated to angle-resolved studies of liquids. It allows samples to remain horizontal, while spectra at normal and grazing emission are recorded simultaneously by two electron analysers. This new setup with the name DASSA (Dual Analyser System for Surface Analysis) was characterised in this thesis, and first results highlighting its potential and necessity were presented.[P5]

10. Zusammenfassung

Im Jahr 2006 begann die Arbeitsgruppe von Florian Maier am Department Chemie der Universität Erlangen-Nürnberg (Physikalische Chemie II, Prof. Hans-Peter Steinrück)[4,29] mit Oberflächenforschung an Ionischen Flüssigkeiten (ILs). Im Zuge dessen wurde eine große Anzahl von verschiedenen ILs mit winkelaufgelöster Röntgenphotoelektronenspektroskopie (angle-resolved X-ray photoelectron spectroscopy, ARXPS) untersucht. In den folgenden Jahren wurden zahlreiche fundamentale Erkenntnisse über die Oberflächenzusammensetzung und über Oberflächenanreicherungseffekte in ILs und IL-basierten Mischungen, Lösungen und Dispersionen gewonnen.[6,11-15,69,70] Die Resultate in dieser Dissertation legen die Beiträge des Autors zum Gebiet der IL-Oberflächenuntersuchungen seit 2011 dar, die auf diesen frühen Ergebnissen basieren. Die Arbeit beinhaltet fünf Publikationen und komplementäre unveröffentlichte Daten, und erweitert das Gebiet der IL-Oberflächenforschung um verschiedene funktionalisierte ILs und um weitere Beispiele für chemische Reaktionen in ILs.

Die Oberflächenzusammensetzung funktionalisierter ILs wird durch das Zusammenspiel verschiedener intermolekularer Kräfte bestimmt, die zwischen den verschiedenen Teilen einer IL herrschen. Diese sind ionische Wechselwirkungen zwischen den Kopfgruppen, Dipol-Ion oder dispersive Wechselwirkungen zwischen den Kopfgruppen und den ungeladenen Seitenketten und Dipol-Dipol oder dispersive Wechselwirkungen zwischen den Seitenketten untereinander. Ob die IL einen gewissen Grad an Oberflächenordnung aufweist oder nicht, hängt davon ab, ob und wie stark eine dieser Wechselwirkungen über die anderen überwiegt. Die beobachtete Oberflächenzusammensetzung bewegt sich zwischen deutlicher Oberflächenanreicherung von z.B. halogenierten Alkylketten, und isotropischer Anordnung von z.B. etherfunktionalisierten Gruppen.[P4]

Funktionalisierung von ILs mit reaktiven Gruppen eröffnet die Möglichkeit, IL-Reaktionen mit XPS zu untersuchen. Die Reaktion zwischen dem leicht basischen Anion der IL $[C_8C_1Im]Cl$ und der starken Säure TfOH wurde mit XPS erforscht und die resultierende Anionen-Metathese, die mit einer Dichteänderung einhergeht, wurde verfolgt. Die Änderungen der XP-Spektren während der Säuredosierung und der Manipulation der Probentemperatur zeigen, dass die Reaktion nahezu komplett abläuft, aber auf die oberflächennahe Region der IL beschränkt ist.[P2] Die Untersuchung einer weiteren Reaktion zwischen einer Amin-funktionalisierten IL und gasförmigem CO_2 führte zu fundamentalen Erkenntnissen über die Chemisorption von CO_2 mittels Amin, speziell in IL-Systemen. Zum einen ist die Aufnahmekapazität der oberflächennahen Region für Reaktionsprodukte zwischen CO_2 und Amin wesentlich höher als die des Volumens. Zum anderen enthält die an der Oberfläche

dominante Produktspezies aus stöchiometrischen Gründen die doppelte Menge CO_2 der dominanten Spezies im Volumen. Beide Ergebnisse sind von großem Vorteil für die chemische Absorption von CO_2 in Medien mit einem hohen Verhältnis der Oberfläche zum Volumen.[P3]

Zwei ILs, die eine funktionelle Thioethergruppe an verschiedenen Positionen der Imidazolium-Kopfgruppe tragen, wurden mittels der chemischen Verschiebung der XPS-Signale verglichen, die ein Indikator für Elektronendichte an verschiedenen IL-Atomen ist. Ist der Schwefel direkt an das C2-Atom des Imidazoliums gebunden, zeigt das entsprechende S 2p-Dublett eine deutliche Verschiebung zu höherer Bindungsenergie (BE) im Vergleich zu dem S 2p-Signal einer Thioether-Gruppe, die Teil der Seitenkette an der Position 3 des Imidazoliums ist. Die Elektronendichte des S-Atoms an der Position 2 ist durch eine höhere Elektroneninduktion in den positiv geladenen Imidazoliumring geringer als die des S-Atoms in der Seitenkette an Position 3.[P1] Allerdings sind Veränderungen in der chemischen Verschiebung bei sich nahe verwandten IL-Strukturen häufig weniger stark ausgeprägt als die in den Thioether-Untersuchungen gezeigten, so dass höhere Energieauflösung nötig ist, um sie detektieren zu können. Als Beispiele solcher geringerer Effekte sind Untersuchungen an ILs mit verschiedenen N-basierten Kationen gezeigt, sowie Temperatureffekte in der IL $[C_{18}C_1Im][TfO]$.

Der zweite Schwerpunkt dieser Arbeit liegt auf der Verbesserung der Instrumentation für IL-Oberflächenuntersuchungen. Der Großteil der bisher veröffentlichten Ergebnisse aus Erlangen wurde mit einer herkömmlichen ARXPS-Anlage erzeugt, die Probenrotation zu hohen Elektronenemissionswinkeln zulässt. Allerdings stößt diese Methode an ihre Grenzen, wenn Flüssigkeiten mit geringer Viskosität und/oder mit Filmdicken größer als ~100 µm untersucht werden sollen. Eine neue XPS-Anlage, die speziell für winkelaufgelöste Untersuchungen von Flüssigkeiten ausgelegt ist, wurde durch unsere Arbeitsgruppe entwickelt und wurde 2014 geliefert. Mit dieser können Proben in horizontaler Orientierung verbleiben, während Spektren in normalem und streifendem Ausfall durch zwei Elektronenanalysatoren simultan aufgezeichnet werden. Diese neue Anlage mit dem Namen DASSA (Dual Analyser System for Surface Analysis, Dual-Analysator-System für Oberflächenanalyse) wurde in dieser Arbeit charakterisiert, und erste Ergebnisse wurden präsentiert, die ihr Potential und ihre Notwendigkeit aufzeigen.[P5]

11. Appendix

Published papers:

[P1] N. Taccardi, I. Niedermaier (shared 1st authorship), F. Maier, H.-P. Steinrück, and P. Wasserscheid, *Cyclic Thiouronium Ionic Liquids: Physicochemical Properties and their Electronic Structure Probed by X-Ray Induced Photoelectron Spectroscopy*, Chem-Eur J, 18, 27, 8288-8291, **2012**

http://onlinelibrary.wiley.com/doi/10.1002/chem.201200971/abstract

[P2] I. Niedermaier, N. Taccardi, P. Wasserscheid, F. Maier, and H.-P. Steinrück, *Probing a Gas/Liquid Acid-Base Reaction by X-ray Photoelectron Spectroscopy*, Angew Chem Int Edit, 52, 34, 8904-8907, **2013**

http://onlinelibrary.wiley.com/doi/10.1002/anie.201304115/abstract

[P3] I. Niedermaier, M. Bahlmann, C. Papp, C. Kolbeck, W. Wei, S. Krick Calderón, M. Grabau, P. S. Schulz, P. Wasserscheid, H.-P. Steinrück, and F. Maier, *Carbon Dioxide Capture by an Amine Functionalized Ionic Liquid: Fundamental Differences of Surface and Bulk Behavior*, J Am Chem Soc, 136, 1, 436-441, **2014**

http://pubs.acs.org/doi/abs/10.1021/ja410745a

[P4] C. Kolbeck, I. Niedermaier, A. Deyko, K. R. J. Lovelock, N. Taccardi, W. Wei, P. Wasserscheid, F. Maier, and H.-P. Steinrück, *Influence of Substituents and Functional Groups on the Surface Composition of Ionic Liquids*, Chem-Eur J, 20, 14, 3954-3965, **2014**

http://onlinelibrary.wiley.com/doi/10.1002/chem.201304549/abstract

[P5] I. Niedermaier, C. Kolbeck, H.-P. Steinrück and F. Maier, *Dual Analyzer System for Surface Analysis dedicated to angle-resolved photoelectron spectroscopy at liquid surfaces and interfaces*, Rev Sci Inst, 87, 4, 45105, **2016**

http://scitation.aip.org/content/aip/journal/rsi/87/4/10.1063/1.4942943

Appendix chapter:

A.1. Ferrocenyl-functionalised ILs

As has been introduced in Section 4.2, ferrocenyl ILs are potential candidates for a combined electrochemical/XPS investigation. Therefore, an elaborate assessment of such compounds was carried out. Nine different ferrocenyl-functionalised ILs of the general structure $[(Fc\text{-}L)C_nIm][Tf_2N]$ (Fc = ferrocene, L = linker) were investigated with ARXPS in the ESCA setup. The structures of these ILs are given in Figure A 1. The cations are of three types, differing in the linker unit that covalently binds the ferrocenyl moiety to the imidazolium ring. This is either an amide (compounds A1-A5), an ether (A6-A7) or an alkyl unit (A8-A9). The compounds of the amide- and alkyl-linked groups differ in length of the second alkyl chain at the imidazolium ring, and in the case of the ether-linked compounds, they differ in the chain length of the linker itself. The syntheses of these new ILs were carried out at Lehrstuhl für Organische Chemie II by B. Gharib in the years 2011-2013 who also supplied us with samples. Details are given in Reference 71. As has been noted in Section 4.2, the presence of surface-active contaminations in these compounds complicated data analysis with respect to surface composition. Nevertheless, clear common trends found in all data sets allowed for relatively reliable conclusions. In 2012, Taylor and Licence published an XPS study on methylene-bound ferrocenyl ILs (in particular, $[(FcC_1)C_1Im][Tf_2N]$ and $[(FcC_1)C_1Im][Tf_2N]_2$ with oxidations states Fe(II) and Fe(III), respectively)[72], which allows for comparison to some of our findings.

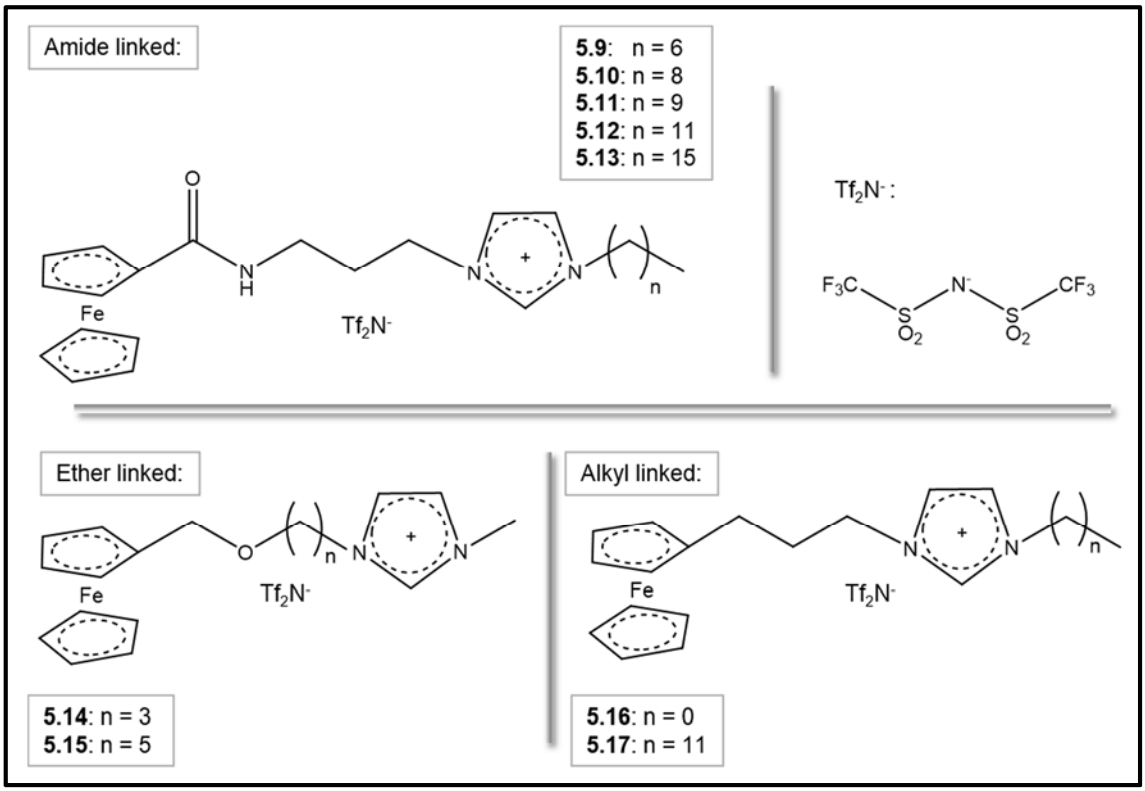

Figure A 1: Investigated ferrocenyl ILs with either an amide, ether or alkyl linker between the ferrocenyl unit and imidazolium.

A.1.1. Stability to sputter cleaning

Most of the samples contained a surface-active polysiloxane impurity noticeable by dominant Si 2s and Si 2p peaks in survey scans. Prior to ARXPS experiments (see Section A.1.2 below), Ar sputtering tests were carried out to determine a practicable procedure for surface cleaning without inducing severe surface damage.

For compounds A5 and A4, exemplary 80° survey scans with clear contamination signals are given in Figure A 2 (top left and middle, black spectra). The signals at around 100 eV and 152 eV are attributed to the Si 2p and Si 2s levels, respectively. Apart from that, the survey spectra are dominated by F 1s (~689 eV), O 1s (~532 eV) and C 1s (~285 eV) signals. The latter two are also characteristic for polysiloxanes. The alkyl-linked compound A8 exhibits a large signal at 285 eV in the 80° C 1s region scan typically associated with C atoms present within polysiloxane contaminations (see Figure A 2 top right, black).

Sputtering was first performed with 0.5 keV Ar ions for 30 min. For the three groups of ferrocenyl ILs with different linkers, the efficiency and impact of this sputtering step differed. For the amide-linked ILs, sputtering led to the desired reduction in Si 2s/2p, O 1s and C 1s signal intensities in the survey spectrum (compare black and grey spectra for A5 at top left in Figure A 2) and to an increase of all other IL signals. The latter was, however, not true for the Fe 2p region (bottom left). Prior to sputtering, a sharp Fe 2p doublet with the $2p_{3/2}$ component at ~709 eV and the $2p_{1/2}$ component at ~722 eV was visible, which fits well to a ferrocene (Fe(II)) signal.[72] After sputtering, the spectrum showed broad features mainly at higher binding energies, which likely contain Fe(II) and Fe(III) contributions and are a sign for severe damage of the XPS accessed IL molecules. Taylor et al. also observed very similar spectral changes during Ar sputtering for their methylene bridged ILs.[72]

For the alkyl-linked ILs (right spectra of A8), sputtering with 0.5 kV acceleration voltage successfully decreased the contamination, as deduced from the observation that the Fe $2p_{3/2}$ (bottom) and all other IL signals (not shown) increased in intensity without loss of quality. At the same time, the Si 2s/2p as well as the O 1s and C 1s signals decreased in intensity (Si and O not shown). In the C 1s region (top), only the contamination carbon peak at ~285 eV decreases, and at the same time, the components at ~293 eV and ~287 eV, solely associated with IL signals, gain intensity. The high stability of the alkyl linked compounds A8 and A9 against Ar sputtering is in contrast to the pronounced beam damage effects reported by Taylor et al. for their alkyl linked Fc-ILs.[72] This difference in stability might be related to the longer alkyl linker in our case.

For the ether-linked compounds A6 and A7, sputtering with 0.5 keV Ar ions was also tested (spectra not shown). After sputtering, XP spectra of good quality with reasonable peak shapes and no unexpected features were found as in the case of A8 and A9, indicating that the ether-linked compounds are also stable under these sputtering conditions.

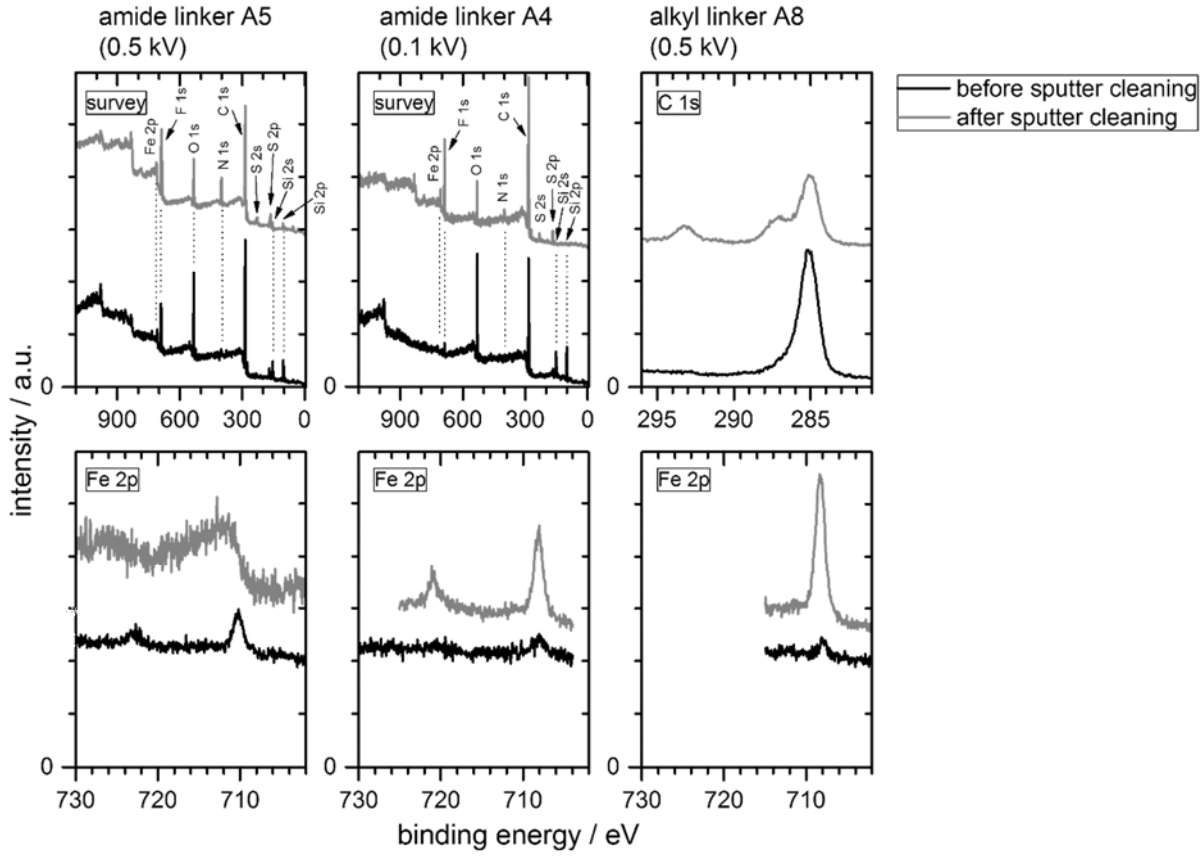

Figure A 2: 80° emission spectra of selected ferrocenyl ILs before (black) and after (grey) surface cleaning by Ar sputtering. In all cases sputtering reduces Si, O and C content (surveys and C 1s, top row). Alkyl linked ferrocenyl ILs show improved purity with a much improved Fe $2p_{3/2}$ signal after sputtering with 0.5 kV acceleration voltage (right), while amide linked ILs after sputtering with the same voltage show signs of degradation in the Fe 2p region (left). Sputtering the amide linked compounds repeatedly with 0.1 kV acceleration voltage also leads to improved Fe 2p signals (middle). Amide (left and middle) spectra were recorded at RT, alkyl (right) spectra at 343 K.

As the amide-linked compounds were prone to degradation when sputtered with 0.5 kV acceleration voltage, a series of milder sputtering steps was carried out for those ILs. 0.1 keV Ar ions were repeatedly applied for only 10 min, followed by XPS to monitor the cleaning progress. As shown in Figure A 2 (middle) for compound A4, surface contamination was successfully minimised even for these more sensitive samples. In the survey scan (top), the Si 2s/2p, O 1s and C 1s signals decrease, while simultaneously all IL signals increase in intensity. The Fe 2p region (bottom) also shows a much increased signal after repeated mild sputtering with a clear doublet structure.

A.1.2. Surface composition of ferrocenyl ILs

Since some ILs (e.g. A5) showed pronounced spectral changes in the Fe 2p signals after sputtering, indicating massive beam damage at the ferrocenyl unit, only ILs will be discussed in a state where a sharp Fe(II) signal at around 709 eV was detected. For the following samples, details about pre-treatment and, if applicable, features in the spectra after pre-treatment indicating remaining contaminations or minor beam damage are given in Table A 1. The amide-linked ILs A1-A4 were sputtered repeatedly with 0.1 kV acceleration voltage and all alkyl-linked ILs were sputtered with 0.5 kV for an extended period (30 min). The amide-linked compound A5 was investigated as received without sputter treatment to retain an untreated dataset, although it also showed clear Si signals in 80° emission. As no Si signals were visible in the survey scans of the ether-linked compounds, these were investigated without sputtering.

Table A 1: Pre-treatment of the samples evaluated in Figure A 4, A 5 and A 7.

Sample	**Sputtered (energy in keV) / heated**	**Spectral features**
Amide linker		
A1: [(Fc(CO)(NH)C_3)C_7Im][Tf_2N]	x (0.1) / -	Slight Si and Au traces in 80° survey scan
A2: [(Fc(CO)(NH)C_3)C_9Im][Tf_2N]	x (0.1) / -	Slight Si trace in 80° survey scan
A3: [(Fc(CO)(NH)C_3)C_{10}Im][Tf_2N]	x (0.1) / x	Beam/sputter damage visible in Fe 2p
A4: [(Fc(CO)(NH)C_3)C_{12}Im][Tf_2N]	x (0.1) / -	
A5: [(Fc(CO)(NH)C_3)C_{16}Im][Tf_2N]	- / -	Clear Si 2s/2p signals in 80° survey/ 0° and 80° region scans; shoulder in F 1s
Ether linker		
A6: [(FcCOC_3)C_1Im][Tf_2N]	- / -	
A7: [(FcCOC_5)C_1Im][Tf_2N]	- / -	
Alkyl linker		
A8: [(FcC_3)C_1Im][Tf_2N]	x (0.5) / x	
A9: [(FcC_3)C_{12}Im][Tf_2N]	x (0.5) / x	

In addition to sputter cleaning, compounds A3, A8 and A9 were heated to 340 K for 20-30 min after sputtering. It is the general experience of our group that for sputter-cleaned ILs, post-sputter heating can improve XPS signal quality, likely by enhancing diffusion that leads to a freshly exposed surface containing undamaged IL molecules from deeper layers. In the present case, the efficiency of the additional heating step was not assessed.

For compounds A1 and A2, traces of Si signals were still visible after sputtering in the 80° spectra, showing that the contamination was not removed completely. For A1, also a Au 4f

trace was visible in the 80° wide scan, which is a consequence of the analyser window positioned close to the IL rim on the Au sample support. Compound A3 contained a distorted feature in the Fe 2p spectra in addition to the main peak. As this IL underwent a sputter procedure identical to that of the other amide-linked ILs, but was the only one that was heated in addition, it is possible that this heating step led to structural damage instead of the desired improved surface purity. No such features were, however, observed in the Fe 2p spectra of the other heated ILs (A8 and A9). The unsputtered and unheated compound A5 contained a tiny shoulder within the F 1s signal of unclear origin apart from the already mentioned Si signals.

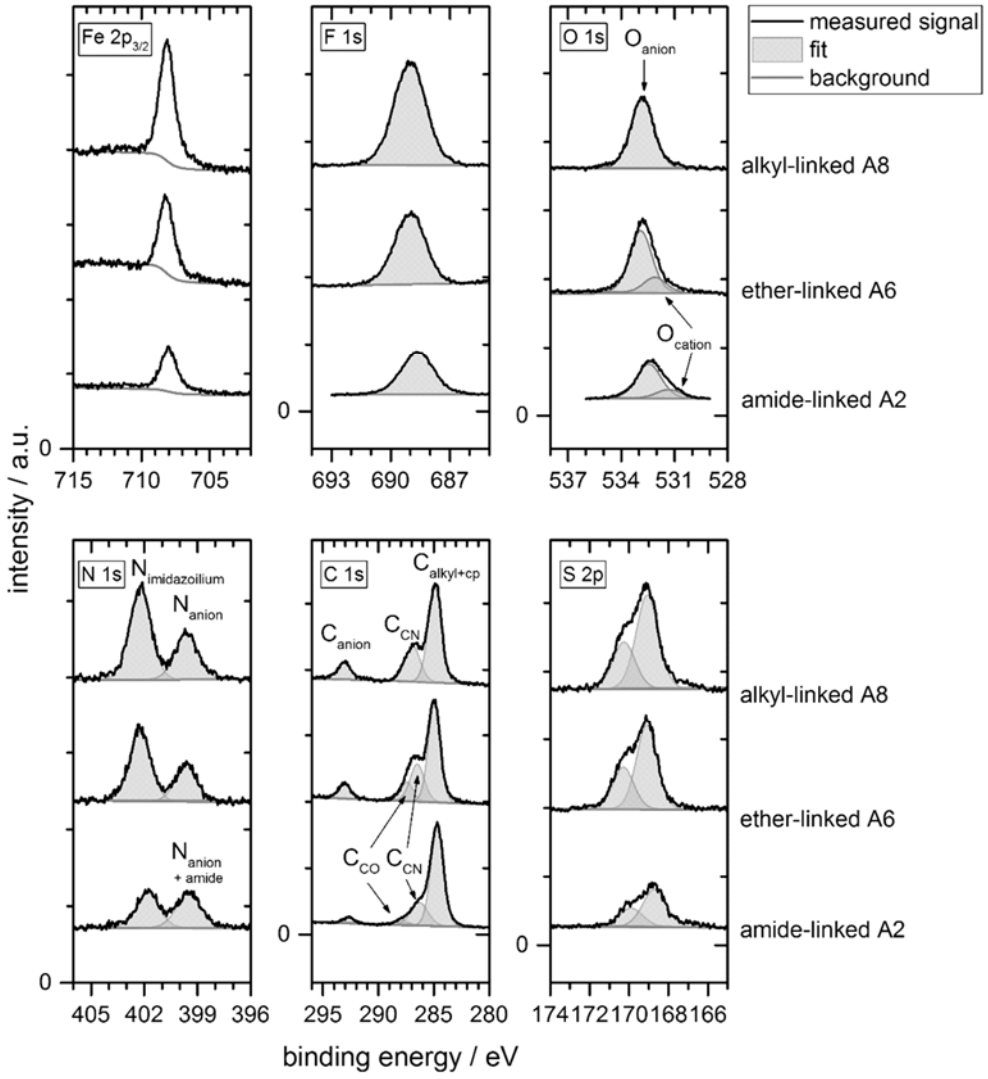

Figure A 3: Exemplary region scans for each group with different linker unit. Fit peaks are explained in the text. Spectra are not normalised, but offset for better visibility.

Figure A 3 shows all 0° region spectra for one representative of each IL group, namely compound A2 (amide-linked, bottom), compound A6 (ether-linked, middle) and compound A8 (alkyl-linked, top). The fit peaks used to determine peak areas for the different components are

also shown. The Fe $2p_{3/2}$ region was not fitted, but numerically integrated. Trying to fit the Fe $2p_{3/2}$ spectra showed that due to asymmetry of the peaks and the presence of a satellite structure towards higher BE, fitted areas are by 10-30 % lower than integration of the complete region, leading to too low experimental Fe atom numbers in the evaluation. The F 1s, N 1s and S 2p regions were fitted as detailed in Section 3.4. Note that only for the amide-linked ILs, the N 1s peak at lower BE, associated with the $[Tf_2N]^-$ anion, contains a contribution of the amide N atom of the cation, leading to a 1 : 1 ratio with the imidazolium N 1s peak as opposed to the 2 : 1 ratio for the ether- and alkyl-linked ILs. The main feature of the O 1s region is associated with the four O atoms of the anion. For the ether- and amide-linked ILs, there is an additional O 1s signal attributed to the O atom of the cation that is visible as a shoulder towards lower BE. Thus, two peaks were used for these spectra fits with an area constraint of the nominal 4 : 1 ratio. Also, peak fwhms were constrained to be identical to obtain reasonable fits. For the C 1s region, the C_{anion} peak is offset sufficiently from the main peak to be fitted without constraints. The main peak at ~284.5 eV can be attributed to all C atoms bound to C and H only, namely the alkyl and cyclopentadienyl (cp) C atoms of the cation. For the shoulder towards higher BE, a single component can be resolved for the alkyl-linked IL, associated with all C atoms bound to N within the cation at the imidazolium moiety. For the ether- and alkyl-linked ILs, a further shoulder towards higher BE is present. This can be attributed to all C atoms bound to O, either in the ether or amide group. Area constraints were used for the 0° fits according to the nominal stoichiometry (e.g. a ratio of 19 : 6 : 1 for $C_{alkyl+cp}$: C_{CN} : C_{CO} for compound A2). No other constraints were made.

The 80° spectra were again not fitted for Fe $2p_{3/2}$ and fitted without constraints for the F 1s and N 1s regions, and the O 1s region of the alkyl linked ILs with only one component. For the S 2p doublet, identical constraints to the 0° spectra were used. For the O 1s region of the amide- and ether-linked compounds that contain two components, spectra were fitted with a peak distance constraint using the value obtained from the respective 0° fit. Identical fwhm values were again pre-set, but areas were not constrained. Similarly, for the C 1s region, relative peak positions within the main feature were constrained to the values obtained from the 0° fits, and the same was done for relative fwhm ratios. No area constraints were used.

As the ID for 0° emission typically extends over several molecular layers with on average no pronounced orientation effects, these spectra are suitable to quantitatively determine the composition of all compounds. Data evaluation for all 0° spectra of compounds A1-A9 is given in Figure A 4. Here, the experimentally determined atom numbers n_i for all species i are given as a percentage of the nominal values ($n_{i,\ exp(0°)}$ / $n_{i,\ nominal}$ x 100 %). Due to an experimental uncertainty of ± 10 % (grey bar in Figure A 4), only larger deviations will be discussed in the following. The top graph represents O 1s and C 1s atom numbers (apart from the anion data

points) that could potentially contain a contribution from contaminants still present at the surface. Note that due to the area constraint used in fitting, the value is identical for all three C species so that it is impossible to determine excess of one specific C species. The middle row details results for all anion signals. Note that for the N 1s values of the amide-linked ILs A1-A5, the N atoms of the $[Tf_2N]^-$ anion as well as those of the amide linkers in the cation are included, as both give rise to superimposed peaks at ~399 eV. The remaining cation signals (Fe $2p_{3/2}$ and $N_{imidazolium}$) are shown at the bottom.

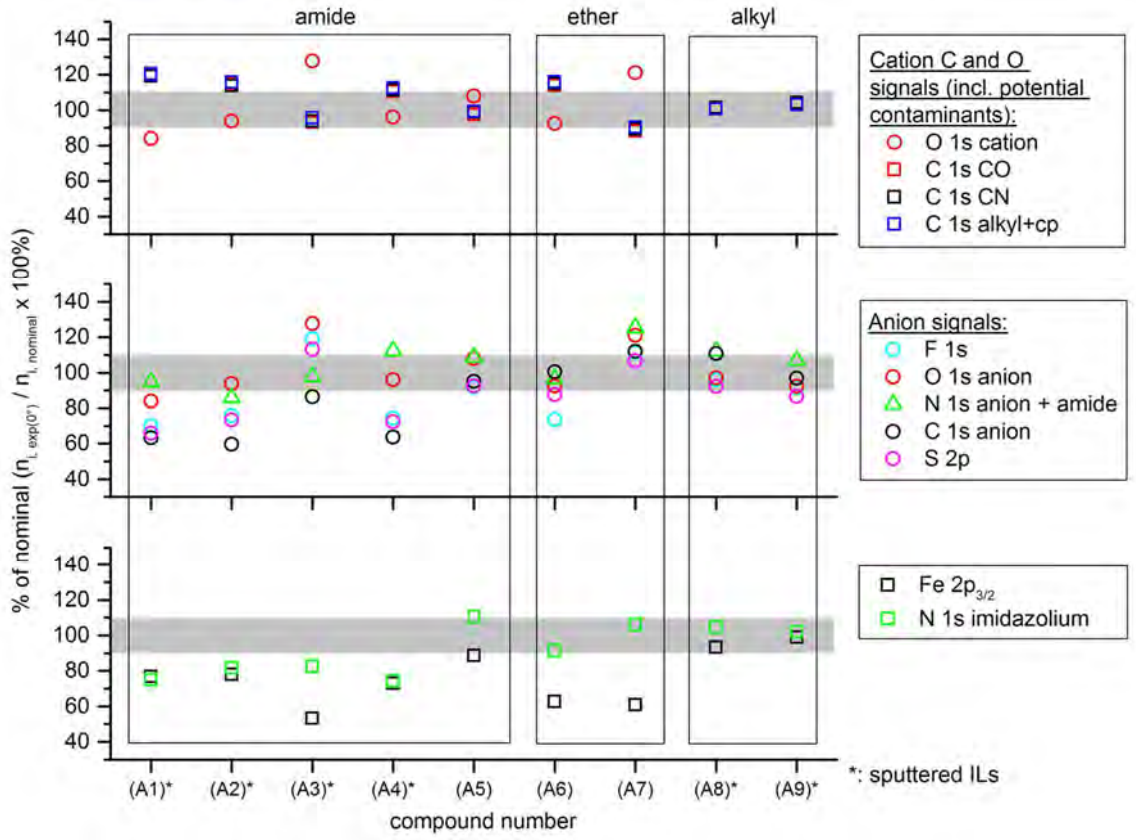

Figure A 4: Experimental atom numbers in 0° emission as percentage of nominal values.

Only for the two alkyl-linked compounds A8 and A9 after sputtering, the composition measured in 0° matched the nominal values. Interestingly, the experimental values of the unsputtered amide-linked compound A5 that showed pronounced Si signals also were within the experimental uncertainty. It is the experience of our group that conventional polysiloxane contaminations in ILs (e.g. from glassware grease) typically provide additional intensity to the O 1s and C 1s signals of the IL. Thus, the Si contamination observed for A5 is likely not of the polysiloxane type, but a different Si-based compound.

For both A3 and A7, anion signals are on average higher than expected. This likely results from residual $Li[Tf_2N]$ still present as an impurity within the IL. $Li[Tf_2N]$ is used in the synthesis for anion metathesis. Li is hardly detectable in XPS due to the very low cross section of the

Li 1s core level signal, so that only additional intensity in all $[Tf_2N]^-$ signals is detected. Consequently, all other signals tend to be quite low in the evaluation of these compounds with $[Tf_2N]^-$ excess. In addition, the O_{cation} shows an artificially enhanced intensity due to the fact that in the fit model used the peak area is constrained to ¼ of the O_{anion} signal. In all cases, O_{cation} thus shows exactly the same deviation from 100 % than O_{anion} does.

For compounds A1, A2, A4 and A6, there is clearly an organic contamination present, as all cationic C 1s signals are too high and consequently, all other signals with a few exceptions are too low. For the first two compounds, there is likely a persistent polysiloxane contamination present, as Si 2s/2p signals were still visible even after sputtering. For a clearer analysis, atom numbers were re-calculated omitting the C 1s signals of the cation and all O 1s signals that are also expected to contain an impurity contribution. The results are shown in Figure A 5.

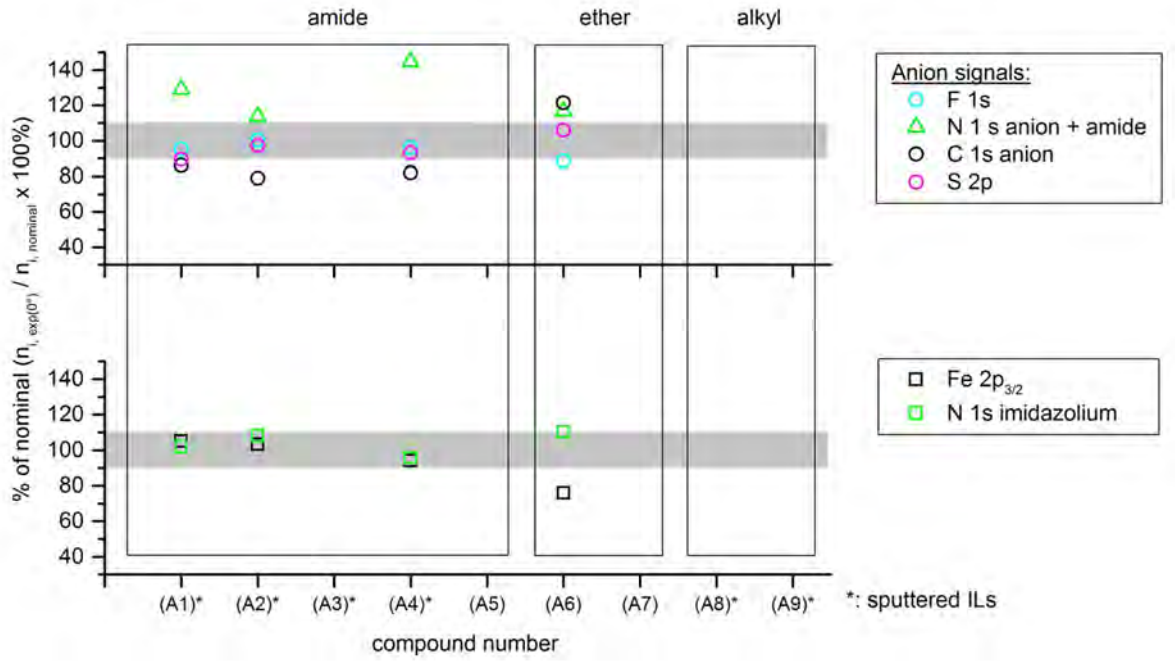

Figure A 5: Experimental atom numbers in 0° emission as percentage of nominal values, as in Figure A 4, but basing the calculation of experimental atom numbers only on those signals not associated with contaminant contributions.

All data points now move closer to expected stoichiometry. For $N_{imidazolium}$, the values for all compounds are now within or very close to the expected grey region. The Fe $2p_{3/2}$ intensity is also within the nominal range for A1, A2 and A4, but clearly too low for A6. Synthesis of the latter is done via functionalisation of imidazole with the bromo-terminated ferrocenylalkyl ethoxy compound in a first step as shown in Figure A 6 (top). The resulting ferrocenylimidazole is then methylated with methyl iodide to form the disubstituted imidazolium. One possible explanation for the low Fe content could be insufficient product separation after the first functionalisation step. If this hypothesis was true, residual unreacted imidazole would then

react with the alkylation agent methyl iodide in a side reaction forming additional dimethylimidazolium iodide ($[C_1C_1Im]I$) as shown in the last row of Figure A 6. After the final anion metathesis step that exchanges I^- by $[Tf_2N]^-$ (not shown), $[C_1C_1Im][Tf_2N]$ would be present as an impurity within the IL, leading to an overall too low Fe content. The comparatively low experimental O_{cation} numbers (see Figure A 4) corroborate this assumption. However, a too low C_{alkyl} content would also be expected, but is not experimentally observed.

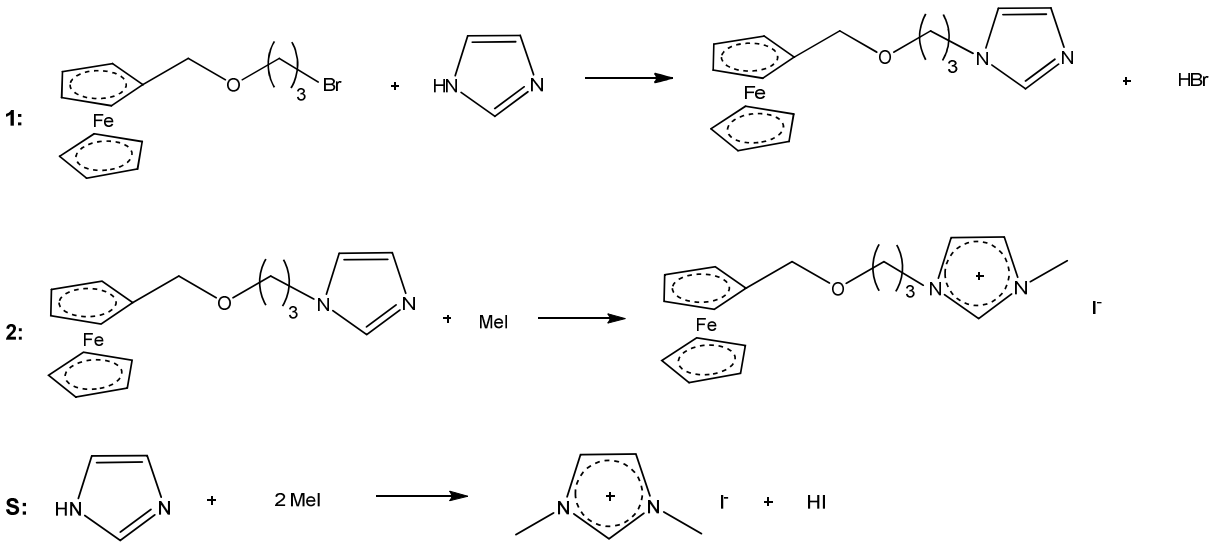

Figure A 6: 1 and 2: part of the synthesis of compound A6, from Reference 71. S: Possible side-reaction of unreacted imidazolium of step 1 with MeI in step 2 to form $[C_1C_1Im]I$.

The anion signals in general still do not show a perfect match with nominal values. Most striking is the too high content of N_{anion} for all compounds. Many species containing neutral nitrogen (e.g. amines, amides) will give rise to a signal superimposed by the N_{anion} signal. Hence, assuming organic contaminations are only based on C and O is likely an oversimplification, and in this case, N may also be present as part of an impurity. This impurity is possibly a by-product of the amide synthesis for compounds A1, A2 and A4.

80° emission spectra were recorded for all compounds in order to determine ion orientation at the IL-vacuum interface by comparison with the 0° spectra described above. Note that for samples with surface-active contaminations, the results have to be considered with care. Figure A 7 shows the surface composition derived from 80° spectra relative to the 0° spectra ($(100\ \% \times n_{i,\ exp(80°)} / n_{i,\ exp(0°)}) - 100\ \%$). A data point above the line at zero indicates that for the corresponding species, relative intensity in 80° is higher than in 0° and it is surface-enriched, whereas a data point below the line indicates surface depletion. Unsurprisingly, for compounds A1, A2, A4 and A6, the organic contamination dominates the surface and hence gives rise to increased C_{alkyl} intensity at the surface, while in general the intensity of all other signals decreases in 80°. The presence of a surface-active organic contamination also shows

up in the large deviation from the O_{anion} data points from all other anion data for A1. Similarly, for A5 that was known to contain a surface-active contamination conspicuous in Si 2s/2p signals in the 80° survey scan, the fact that O_{anion} strongly increases in 80° while all other signals apart from $C_{alkyl+cp}$ decrease is a consequence of this contamination.

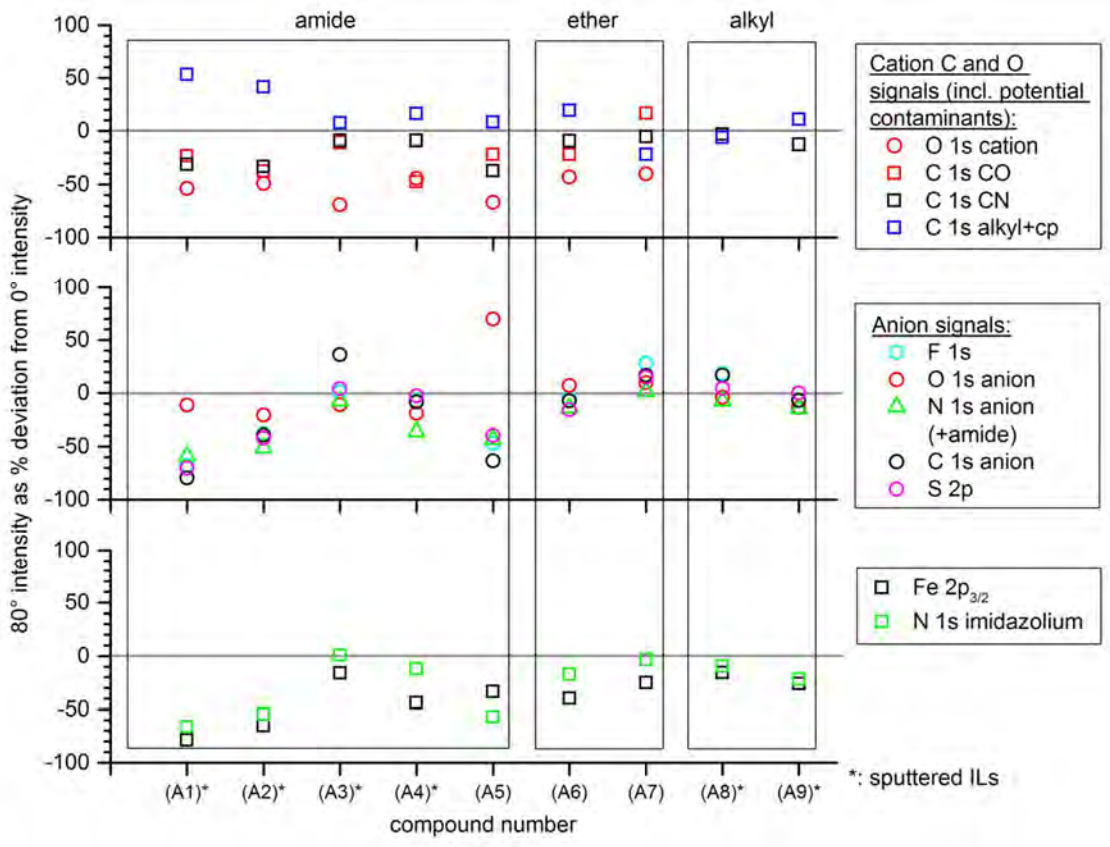

Figure A 7: Percentage deviation of experimental atom numbers at 80° emission from experimental atom numbers at 0° emission.

Where it is possible to analyse the C signals that originate from the cation (compounds A3, A5, A7, A8 and A9 in Figure A 7), one can state that with the exception of A7 and A8, the $C_{alkyl+cp}$ signal is enhanced in 80°. Furthermore, in all cases, C_{CN} and for the amide-linked ILs also C_{CO} and O_{cation} is decreased. This indicates an orientation of the charged imidazolium moiety away from the surface and towards the IL bulk, which at least for compounds A5, A8 and A9 is in line with the decrease in $N_{imidazolium}$ intensity in 80°. For the amide compounds, this also shows the orientation of the amide moiety towards the bulk. As the $C_{alkyl+cp}$ signal contains contributions of both the ferrocenyl and the alkyl moiety of the cation, the signal enhancement for A3, A5 and A9 could be attributable to a surface enrichment of both or any of these moieties. However, in all cases Fe is shown to be surface-depleted and notably, the $C_{alkyl+cp}$ intensity only increases in compounds where a long terminal alkyl chain is present ($-(CH_2)_nCH_3$ with n = 9 for A3, n = 15 for A5 and n = 11 for A9). Such terminal alkyl chains generally exhibit a clear orientation towards the surface in simple ILs when of sufficient lengths ($n \geq 3$)[11], indicating

that this is also the case here. In compound A8, n equals zero (methyl group) and for compound A7 where the chain contains 5 C atoms, its position is not terminal, so that in these two compounds, no predominant alkyl surface enrichment is observed.

The decrease in Fe $2p_{3/2}$ for all compounds shows that the ferrocenyl moiety is preferentially orientated towards the bulk. Comparing the magnitude of the Fe $2p_{3/2}$ and $N_{imidazolium}$ signal decrease in 80° at the bottom of Figure A 7 shows that for all compounds with the exception of A5, the Fe $2p_{3/2}$ signal is on average more attenuated than the $N_{imidazolium}$ signal. This might be an indication that the ferrocenyl moiety is on average further away from the surface compared to the imidazolium headgroup. However, this interpretation must be taken with care. Since the kinetic energy of the Fe 2p signal of about 780 eV is lower than of the N 1s core level with around 1080 eV kinetic energy, the differences in inelastic mean free path for both core levels could also contribute to the differences in intensity changes. Nevertheless, an indication of the sub-surface localisation of the ferrocene unit could also be derived from the fact that in most cases (8 out of 9 samples), the Fe $2p_{3/2}$ signal attenuation is more pronounced than that of all anion signals, showing that the ferrocenyl moiety also lies below the complete anion. Again, the exception is compound A5. The reason for the deviation in A5 is likely related to the Si-based impurity that may either introduce artefacts into the spectra or effectively change surface composition.

The fact that for almost all ferrocenyl-IL samples, the ferrocenyl moiety preferentially lies below the anion and possibly below the imidazolium group is to some extent unexpected. Recalling the results of [P4], it was shown that for different classes of ILs investigated with ARXPS, the polar headgroups of cations and anions form a layer at a similar distance from the surface. Moreover, neutral groups such as alkyl chains or functional groups such as neutral amines have a tendency for orientation towards the vacuum in case of low attractive interaction of these groups with the headgroups. With increasing interaction, the surface enrichment of the side chains is lowered, and is completely lost for very strong interaction, e.g. in the case of ether functionalisation within the side chains. Also, in the case of side chains shorter than 4 atoms, no enrichment was found. In these last two cases, polar headgroups and functional side chains show isotropic arrangement and are on average at the same distance from the outer surface.

The complete ferrocenyl group linked to the imidazolium headgroup for the ILs A1-A9 is a neutral unit as long as Fe in the centre is formally in oxidation state +2. Thus, one could expect a tendency of this unit to exhibit surface enrichment. Attractive interactions with the ionic headgroups might nevertheless be present. These could include Coulombic and/or π-π interactions of the cp ligands with the imidazolium ring, favouring a preferential ferrocenyl orientation towards the bulk in the surface layer. One could also assume that for the amide-

linked compounds A1-A5 and for the ether-linked compounds A6-A7, interaction of functionalised amide/ether units within the linker chain and the ionic headgroups also suppresses any pronounced surface orientation of the nonpolar ferrocenyl part. For the alkyl-linked compounds A8-A9, the propyl chain might be too short to allow pronounced ferrocenyl surface enrichment. These factors could lead to a more isotropic surface arrangement. However, they cannot explain the likely positioning of the Fc unit below the anion. This arrangement could be related to the bulky size of the Fc moiety. For a more detailed analysis, samples with high purity are required before clear conclusions are possible.

12. Literature

[P1] N. Taccardi, I. Niedermaier (shared 1st authorship), F. Maier, H.-P. Steinrück, and P. Wasserscheid, *Cyclic Thiouronium Ionic Liquids: Physicochemical Properties and their Electronic Structure Probed by X-Ray Induced Photoelectron Spectroscopy*, Chem-Eur J, 18, 27, 8288-8291, **2012**.

[P2] I. Niedermaier, N. Taccardi, P. Wasserscheid, F. Maier, and H.-P. Steinrück, *Probing a Gas/Liquid Acid-Base Reaction by X-ray Photoelectron Spectroscopy*, Angew Chem Int Edit, 52, 34, 8904-8907, **2013**.

[P3] I. Niedermaier, M. Bahlmann, C. Papp, C. Kolbeck, W. Wei, S. Krick Calderón, M. Grabau, P. S. Schulz, P. Wasserscheid, H.-P. Steinrück, and F. Maier, *Carbon Dioxide Capture by an Amine Functionalized Ionic Liquid: Fundamental Differences of Surface and Bulk Behavior*, J Am Chem Soc, 136, 1, 436-441, **2014**.

[P4] C. Kolbeck, I. Niedermaier, A. Deyko, K. R. J. Lovelock, N. Taccardi, W. Wei, P. Wasserscheid, F. Maier, and H.-P. Steinrück, *Influence of Substituents and Functional Groups on the Surface Composition of Ionic Liquids*, Chem-Eur J, 20, 14, 3954-3965, **2014**.

[P5] I. Niedermaier, C. Kolbeck, H.-P. Steinrück and F. Maier, "*Dual Analyzer System for Surface Analysis (DASSA)", a UHV system dedicated for angle-resolved photoelectron spectroscopy at liquid surfaces and interfaces*, Rev Sci Inst, 87, 4, 45105, **2016**.

1. H. Siegbahn and K. Siegbahn, *ESCA applied to liquids*, J Electron Spectrosc, 2, 319-325, **1973**.

2. H. Fellner-Feldegg, H. Siegbahn, L. Asplund, P. Kelfve, and K. Siegbahn, *ESCA applied to liquids IV. A wire system for ESCA measurements on liquids* J Electron Spectrosc Rel Phen 7, 421-428, **1975**.

3. B. Winter, *Liquid microjet for photoelectron spectroscopy*, Nucl Instrum Meth A, 601, 1-2, 139-150, **2009**.

4. F. Maier, J. M. Gottfried, J. Rossa, D. Gerhard, P. S. Schulz, W. Schwieger, P. Wasserscheid, and H.-P. Steinrück, *Surface enrichment and depletion effects of ions dissolved in an ionic liquid: an X-ray photoelectron spectroscopy study*, Angew Chem Int Edit, 45, 46, 7778-7780, **2006**.

5. E. F. Smith, I. J. Villar Garcia, D. Briggs, and P. Licence, *Ionic liquids in vacuo; solution-phase X-ray photoelectron spectroscopy*, Chem Commun, 45, 5633-5635, **2005**.

6. C. Kolbeck, J. Lehmann, K. R. J. Lovelock, T. Cremer, N. Paape, P. Wasserscheid, A. P. Fröba, F. Maier, and H.-P. Steinrück, *Density and Surface Tension of Ionic Liquids*, J Phys Chem B, 114, 51, 17025-17036, **2010**.

7. S. G. Lee, *Functionalized imidazolium salts for task-specific ionic liquids and their applications*, Chem Commun, 10, 1049-1063, **2006**.

8. F. Karadas, M. Atilhan, and S. Aparicio, *Review on the Use of Ionic Liquids (ILs) as Alternative Fluids for CO_2 Capture and Natural Gas Sweetening*, Energ Fuel, 24, 5817-5828, **2010**.

9. S. Caporali, U. Bardi, and A. Lavacchi, *X-ray photoelectron spectroscopy and low energy ion scattering studies on 1-buthyl-3-methyl-imidazolium bis(trifluoromethane) sulfonimide*, J Electron Spectrosc, 151, 1, 4-8, **2006**.

10. O. Höfft, S. Bahr, M. Himmerlich, S. Krischok, J. A. Schaefer, and V. Kempter, *Electronic structure of the surface of the ionic liquid [EMIM][Tf_2N] studied by metastable impact electron spectroscopy (MIES), UPS, and XPS*, Langmuir, 22, 17, 7120-7123, **2006**.

11. K. R. J. Lovelock, C. Kolbeck, T. Cremer, N. Paape, P. S. Schulz, P. Wasserscheid, F. Maier, and H.-P. Steinrück, *Influence of Different Substituents on the Surface Composition of Ionic Liquids Studied Using ARXPS*, J Phys Chem B, 113, 9, 2854-2864, **2009**.

12. C. Kolbeck, T. Cremer, K. R. J. Lovelock, N. Paape, P. S. Schulz, P. Wasserscheid, F. Maier, and H.-P. Steinrück, *Influence of Different Anions on the Surface Composition of Ionic Liquids Studied Using ARXPS*, J Phys Chem B, 113, 25, 8682-8688, **2009**.

13. C. Kolbeck, M. Killian, F. Maier, N. Paape, P. Wasserscheid, and H.-P. Steinrück, *Surface characterization of functionalized imidazolium-based ionic liquids*, Langmuir, 24, 17, 9500-9507, **2008**.

14. I. Niedermaier, C. Kolbeck, N. Taccardi, P. S. Schulz, J. Li, T. Drewello, P. Wasserscheid, H.-P. Steinrück, and F. Maier, *Organic Reactions in Ionic Liquids Studied by in situ XPS*, Chemphyschem, 13, 7, 1725-1735, **2012**.

15. C. Kolbeck, I. Niedermaier, N. Taccardi, P. S. Schulz, F. Maier, P. Wasserscheid, and H.-P. Steinrück, *Monitoring of Liquid-Phase Organic Reactions by Photoelectron Spectroscopy*, Angew Chem Int Edit, 51, 11, 2610-2613, **2012**.

16. J. H. Davis, *Task-specific ionic liquids*, Chem Lett, 33, 9, 1072-1077, **2004**.

17. H.-P. Steinrück, J. Libuda, P. Wasserscheid, T. Cremer, C. Kolbeck, M. Laurin, F. Maier, M. Sobota, P. S. Schulz, and M. Stark, *Surface Science and Model Catalysis with Ionic Liquid-Modified Materials*, Adv Mater, 23, 22-23, 2571-2587, **2011**.

18. H. Hertz, *Ueber einen Einfluss des ultravioletten Lichtes auf die electrische Entladung*, Annalen der Physik, 267, 8, 983–1000, **1887**.

19. W. Hallwachs, *Ueber den Einfluss des Lichtes auf electrostatisch geladene Körper*, Annalen der Physik, 269, 2, 301–312, **1888**.

20. K. Siegbahn, C. Nordling, A. Fahlman, R. Nordberg, K. Hamrin, J. Hedman, G. Johansson, T. Bergmark, S.-E. Karlsson, and I. Lindgren, *ESCA: Atomic, molecular and solid state structure studied by means of electron spectroscopy*, Almquist and Wiksells, Uppsala, **1967**.

21. Stefan Hüfner, *Photoelectron Spectroscopy*, Springer, **1996**.

22. D. Briggs and M. P. Seah, *Practical surface analysis by Auger and X-ray photoelectron spectroscopy*, John Wiley and Sons Ltd, Chichester, **1983**.

23. Paul van der Heide, *X-ray Photoelectron Spectroscopy: An introduction to Principles and Practices*, John Wiley and Sons Ltd, Chichester, **2012**.

24. M. P. Seah and W. A. Dench, *Quantitative electron spectroscopy of surfaces: A standard data base for electron inelastic mean free paths in solids*, Surf Interface Anal, 1, 1, 2-11, **1979**.

25. NIST Electron Inelastic-Mean-Free-Path Database Version 1.2, C. J. Powell and A. Jablonski, U.S. Department of Commerce, **2010**.

26. A. Jablonski and C. J. Powell, *Information depth and the mean escape depth in Auger electron spectroscopy and X-ray photoelectron spectroscopy*, J Vacuum Science & Technology A, 21, 1, 274-283, **2003**.

27. P. Wasserscheid, *Chemistry - Volatile times for ionic liquids*, Nature, 439, 7078, 797-797, **2006**.

28. S. Krischok, R. Ottking, W. J. D. Beenken, M. Himmerlich, P. Lorenz, O. Höfft, S. Bahr, V. Kempter, and J. A. Schaefer, *A comparative study on the electronic structure of the 1-ethyl-3-methylimidazolium bis(trifluoromethylsulfonyl)amide RT-ionic liquid by electron spectroscopy and first principles calculations*, Z Phys Chem, 220, 10-11, 1407-1416, **2006**.

29. J. M. Gottfried, F. Maier, J. Rossa, D. Gerhard, P. S. Schulz, P. Wasserscheid, and H.-P. Steinrück, *Surface studies on the ionic liquid 1-ethyl-3-methylimidazolium ethylsulfate using X-ray photoelectron spectroscopy (XPS)*, Z Phys Chem, 220, 10-11, 1439-1453, **2006**.

30. Till Cremer, *Ionic Liquid Bulk and Interface Properties: Electronic Interaction, Molecular Orientation and Growth Characteristics*, PhD thesis, Universität Erlangen-Nürnberg, **2012**.

31. J. Pantförder, S. Pöllmann, J. F. Zhu, D. Borgmann, R. Denecke, and H.-P. Steinrück, *New setup for in situ x-ray photoelectron spectroscopy from ultrahigh vacuum to 1 mbar*, Rev Sci Instrum, 76, 1, **2005**.

32. NIST Standard Reference Database 20, Version 4.1, *http://srdata.nist.gov/xps/*, A. V. Naumkin, A. Kraut-Vass, S. W. Gaarenstroom, and C. J. Powell

33. C. D. Wagner, L. E. Davis, M. V. Zeller, J. A. Taylor, R. H. Raymond, and L. H. Gale, *Empirical Atomic Sensitivity Factors for Quantitative Analysis by Electron-Spectroscopy for Chemical Analysis*, Surf Interface Anal, 3, 5, 211-225, **1981**.

34. M. P. Seah, *Quantification and Measurement by Auger-Electron Spectroscopy and X-Ray Photoelectron Spectroscopy*, Vacuum, 36, 7-9, 399-407, **1986**.

35. C. Kolbeck, *Surface Characterisation of Ionic Liquid Systems and in situ Monitoring of Liquid-Phase Reactions by X-ray Photoelectron Spectroscopy*, PhD thesis, Universität Erlangen-Nürnberg, **2012**.

36. The majority of the ILs used in this work were synthesised by Dr. N. Taccardi, Chemische Reaktionstechnik (Prof. P. Wasserscheid), Universität Erlangen-Nürnberg. Further IL syntheses were done by Dr. F. Kohler and M. Müller, same Chair, and B. Gharib, Organic Chemistry II (Prof. A. Hirsch), Universität Erlangen-Nürnberg

37. R. R. Gagne, C. A. Koval, and G. C. Lisensky, *Ferrocene as an Internal Standard for Electrochemical Measurements*, Inorg Chem, 19, 9, 2854-2855, **1980**.

38. K. R. J. Lovelock, I. J. Villar-Garcia, F. Maier, H.-P. Steinrück, and P. Licence, *Photoelectron Spectroscopy of Ionic Liquid-Based Interfaces*, Chem Rev, 110, 9, 5158-5190, **2010**.

39. J. E. McMurry, *Organic Chemistry*, Brooks Cole, **2004**, 6th ed.

40. D. A. Palmer, R. W. Ramette, and R. E. Mesmer, *Triiodide Ion Formation Equilibrium and Activity Coefficients in Aqueous Solution*, J Solution Chem, 13, 9, 673-683, **1984**.

41. M. Kilian, *Surface studies of simple and complex ionic liquid systems with X-ray induced photoelectron spectroscopy*, Master thesis, Universität Erlangen-Nürnberg, **2007**.

42. M. Freemantle, *An Introduction to Ionic Liquids*, RSC Publishing, Cambridge, **2010**.

43. T. Cremer, C. Kolbeck, K. R. J. Lovelock, N. Paape, R. Wölfel, P. S. Schulz, P. Wasserscheid, H. Weber, J. Thar, B. Kirchner, F. Maier, and H.-P. Steinrück, *Towards a Molecular Understanding of Cation-Anion Interactions - Probing the Electronic Structure of Imidazolium Ionic Liquids by NMR Spectroscopy, X-ray Photoelectron Spectroscopy and Theoretical Calculations*, Chem-Eur J, 16, 30, 9018-9033, **2010**.

44. CNN News Online, *http://edition.cnn.com/2015/11/29/europe/france-paris-cop21-climate-change-conference/index.html*, accessed: 30/11/15 12:30 pm

45. Tagesschau News Online, *http://www.tagesschau.de/ausland/klimakonferenz-119.html*, accessed: 30/11/15 12:30 pm

46. D. Y. C. Leung, G. Caramanna, and M. M. Maroto-Valer, *An overview of current status of carbon dioxide capture and storage technologies*, Renew Sust Energ Rev, 39, 426-443, **2014**.

47. B. Dutcher, M. H. Fan, and A. G. Russell, *Amine-Based CO_2 Capture Technology Development from the Beginning of 2013 - A Review*, Acs Appl Mater Inter, 7, 4, 2137-2148, **2015**.

48. X. Q. Lu, D. L. Jin, S. X. Wei, Z. J. Wang, C. H. An, and W. Y. Guo, *Strategies to enhance CO_2 capture and separation based on engineering absorbent materials*, J Mater Chem A, 3, 23, 12118-12132, **2015**.

49. C. Wu, T. P. Senftle, and W. F. Schneider, *First-principles-guided design of ionic liquids for CO_2 capture*, Phys Chem Chem Phys, 14, 38, 13163-13170, **2012**.

50. J. H. Huang and T. Ruther, *Why are Ionic Liquids Attractive for CO_2 Absorption? An Overview*, Aust J Chem, 62, 4, 298-308, **2009**.

51. M. Ramdin, T. W. de Loos, and T. J. H. Vlugt, *State-of-the-Art of CO_2 Capture with Ionic Liquids*, Ind Eng Chem Res, 51, 24, 8149-8177, **2012**.

52. M. Hasib-ur-Rahman, M. Siaj, and F. Larachi, *Ionic liquids for CO_2 capture - development and progress*, Chem Eng Process, 49, 4, 313-322, **2010**.

53. A. G. Ying, L. Liu, G. F. Wu, G. Chen, X. Z. Chen, and W. D. Ye, *Aza-Michael addition of aliphatic or aromatic amines to alpha,beta-unsaturated compounds catalyzed by a DBU-derived ionic liquid under solvent-free conditions*, Tetrahedron Lett, 50, 14, 1653-1657, **2009**.

54. B. Yu, H. Y. Zhang, Y. F. Zhao, S. Chen, J. L. Xu, L. D. Hao, and Z. M. Liu, *DBU-Based Ionic-Liquid-Catalyzed Carbonylation of o-Phenylenediamines with CO_2 to 2-Benzimidazolones under Solvent-Free Conditions*, Acs Catal, 3, 9, 2076-2082, **2013**.

55. M. K. Munshi, P. S. Biradar, S. M. Gade, V. H. Rane, and A. A. Kelkar, *Efficient synthesis of glycerol carbonate/glycidol using 1,8-diazabicyclo [5.4.0] undec-7-ene (DBU) based ionic liquids as catalyst*, RSC Adv, 4, 33, 17124-17128, **2014**.

56. H. Y. Yuan and J. P. Zhang, *$[DBU-H]^+$ and H_2O as effective catalyst form for 2,3-dihydropyrido[2,3-d]pyrimidin-4(1H)-ones: A DFT Study*, J Comput Chem, 36, 17, 1295-1303, **2015**.

57. H. R. Shaterian, M. Sedghipour, and E. Mollashahi, *[DBU][Ac]-catalyzed mild preparation of 6-amino-4-aryl-5-cyano-3-methyl-1,4-dihydropyrano[2,3-c]pyrazole derivatives*, Res Chem Intermediat, 40, 8, 2721-2728, **2014**.

58. L. Q. Wu, J. L. Song, B. B. Zhang, B. W. Zhou, H. C. Zhou, H. L. Fan, Y. Y. Yang, and B. X. Han, *Very efficient conversion of glucose to 5-hydroxymethylfurfural in DBU-based Ionic Liquids with benzenesulfonate anion*, Green Chem, 16, 8, 3935-3941, **2014**.

59. M. Shigeyasu, H. Murayama, and H. Tanaka, *Production of nanoparticles composed of ionic liquid $[C_4mpyrr][NTf_2]$ and their chemical identification by diameter analysis and X-ray photoelectron spectroscopy*, Chem Phys Lett, 463, 4-6, 373-377, **2008**.

60. S. Men, K. R. J. Lovelock, and P. Licence, *X-ray photoelectron spectroscopy of pyrrolidinium-based ionic liquids: cation-anion interactions and a comparison to imidazolium-based analogues*, Phys Chem Chem Phys, 13, 33, 15244-15255, **2011**.

61. R. K. Blundell and P. Licence, *Quaternary ammonium and phosphonium based ionic liquids: a comparison of common anions*, Phys Chem Chem Phys, 16, 29, 15278-15288, **2014**.

62. S. Men, D. S. Mitchell, K. R. J. Lovelock, and P. Licence, *X-ray Photoelectron Spectroscopy of Pyridinium-Based Ionic Liquids: Comparison to Imidazolium- and Pyrrolidinium-Based Analogues*, Chemphyschem, 16, 10, 2211-2218, **2015**.

63. M. Galinski, A. Lewandowski, and I. Stepniak, *Ionic liquids as electrolytes*, Electrochim Acta, 51, 26, 5567-5580, **2006**.

64. S. U. Lee, J. Jung, and Y. K. Han, *Molecular dynamics study of the ionic conductivity of 1-n-butyl-3-methylimidazolium salts as ionic liquids*, Chem Phys Lett, 406, 4-6, 332-340, **2005**.

65. A. Noda, K. Hayamizu, and M. Watanabe, *Pulsed-gradient spin-echo H-1 and F-19 NMR ionic diffusion coefficient, viscosity, and ionic conductivity of non-chloroaluminate room-temperature ionic liquids*, J Phys Chem B, 105, 20, 4603-4610, **2001**.

66. I. J. Villar-Garcia, E. F. Smith, A. W. Taylor, F. L. Qiu, K. R. J. Lovelock, R. G. Jones, and P. Licence, *Charging of ionic liquid surfaces under X-ray irradiation: the measurement of absolute binding energies by XPS*, Phys Chem Chem Phys, 13, 7, 2797-2808, **2011**.

67. The syntheses were carried out by Dr. F. Kohler, then researcher at Chemische Reaktionstechnik (Prof. P. Wasserscheid), Universität Erlangen-Nürnberg, M. Müller, Chemische Reaktionstechnik (Prof. P. Wasserscheid), Universität Erlangen-Nürnberg,

and Dr. T. Matsuda, then researcher at Physikalische Chemie II (Prof. H.-P. Steinrück), Universität Erlangen-Nürnberg.

68. The synthesis was carried out by S. Dommer, group of Prof. J. Schatz, Organische Chemie I (Prof. R. Tykwinski), Universität Erlangen-Nürnberg

69. C. Kolbeck, N. Paape, T. Cremer, P. S. Schulz, F. Maier, H.-P. Steinrück, and P. Wasserscheid, *Ligand Effects on the Surface Composition of Rh-Containing Ionic Liquid Solutions Used in Hydroformylation Catalysis*, Chem-Eur J, 16, 40, 12083-12087, **2010**.

70. C. Kolbeck, A. Deyko, T. Matsuda, F. T. U. Kohler, P. Wasserscheid, F. Maier, and H.-P. Steinrück, *Temperature-Dependent Surface-Enrichment Effects of Imidazolium-Based Ionic Liquids*, Chemphyschem, 14, 16, 3726-3730, **2013**.

71. B. Gharib and A. Hirsch, *Synthesis and Characterization of New Ferrocene-Containing Ionic Liquids*, Eur J Org Chem, 19, 4123-4136, **2014**.

72. A. W. Taylor and P. Licence, *X-Ray Photoelectron Spectroscopy of Ferrocenyl- and Ferrocenium-Based Ionic Liquids*, Chemphyschem, 13, 7, 1917-1926, **2012**.

73. J. A. R. Samson, *Angular Distributions of Photoelectrons and Partial Photoionization Cross-Sections*, Philos Tr R Soc S-A, 268, 1184, 141-146, **1970**.

74. S. M. Goldberg, C. S. Fadley, and S. Kono, *Photo-Ionization Cross-Sections for Atomic Orbitals with Random and Fixed Spatial Orientation*, J Electron Spectrosc Relat Phenom, 21, 4, 285-363, **1981**.

13. Acknowledgement

Es gibt viele Personen, bei denen ich mich herzlich bedanken möchte.

Bei Herrn Professor Steinrück für die Chance, die Doktorarbeit am Lehrstuhl PC II anfertigen zu können, für beständige Unterstützung, die reichliche Weitergabe von Wissen und extrem schnelles Korrekturlesen.

Bei Florian Maier für die gute Betreuung, für Sich-Zeit-nehmen, auch wenn er eigentlich keine Zeit hatte, für sehr viele Erklärungen à la „Also, jetzt pass mal auf ....." (30 Schmierblätter und 2 Stunden später) „..... ist doch ganz klar und einfach, oder?“, für viel Entscheidungsfreiheit und wenig Druck, und für sehr viel entgegengebrachtes Vertrauen.

Bei allen IL-Kollegen, speziell aber bei Claudia Kolbeck für die gute Betreuung in der Anfangszeit und eine super Zusammenarbeit; bei Flo Rietzler für viel gute Laune und entspanntes Zusammenarbeiten; und bei Bettina Heller, bei der ich mein „Erbe“ in guten Händen weiß.

Bei Herrn Professor Wasserscheid und seinen Mitarbeitern für die erfolgreiche Kooperation und viele gute Ideen und Diskussionen.

Bei Nicola Taccardi für die Synthese eines Großteils der verwendeten ILs, und grundsätzlich für große Hilfsbereitschaft und Unterstützung bei der Aufklärung unerwarteter Prozesse in ILs unter XPS.

Bei HP Bäumler und Bernd Kreß für tausendfache Hilfe bei allen möglichen technischen, mechanischen, elektrischen, elektronischen, wasser- und gasbezogenen Problemen. Ohne euch würde hier nichts laufen!

Bei den Mitarbeitern der Werkstatt für die Anfertigung zahlloser Spezialteile aus skurrilen Materialien und das schnelle Reparieren bei akuten Problemfällen.

Bei weiteren Personen, die ILs oder andere Proben für mich synthetisiert haben (Florian Kohler, Michael Müller, Rainer Lippert, Bhasem Gharib, Wei Wei, Matthias Bahlmann, Swetlana Sachnov, Sabine Dommer).

Bei Herrn Professor Drewello und Jing Li für ESI-MS-Messungen, auch wenn dabei leider kein gemeinsames Paper rauskam; und bei Rolf Kirschbaum für allgemeine Beratung zu MS.

Bei meiner Familie, ohne die ich nicht wäre, wer ich bin, und ohne die ich die Promotion und auch das Studium niemals hätte durchziehen können. Speziell bei meiner Mutter für zehntausend Stunden Kinderbetreuung und bei meinem Vater und Fredi (Familienmitglied im weitesten Sinne) für viele „fachfremde“ Diskussionen, die oft Ansätze zu neuen Lösungsideen waren.

Bei allen früheren und momentanen Mitarbeitern der PC II, die zu einem super Arbeitsklima beigetragen haben. Insbesondere sind zu nennen: Bernd, HP, Sandra, Claudia, Flo V., Michi L., Oli, Alexey, Christoph, Flo R., Andreas Späth, der die Antwort auf alle Fragen kennt, Andre, Susanne, Bettina, Sascha, Flo S., Matze G., Dr. Till,
and yes, Christian Papp, you too.